UNIVERSITY OF SOUTHAMPTON

FACULTY OF ENGINEERING, SCIENCE & MATHEMATICS

SCHOOL OF PHYSICS AND ASTRONOMY

SPECTRAL MODELLING OF MOLECULAR NITROGEN IN AURORA

Olli-Pekka Jokiaho

A Thesis submitted for the degree of Doctor of Philosophy

September 2009

UNIVERSITY OF SOUTHAMPTON

ABSTRACT

FACULTY OF ENGINEERING, SCIENCE & MATHEMATICS

SCHOOL OF PHYSICS AND ASTRONOMY

Doctor of Philosophy

SPECTRAL MODELLING OF MOLECULAR NITROGEN IN AURORA

by Olli-Pekka Jokiaho

A custom made five panel filter mosaic window was designed, installed and operated with the HiTIES (High Throughput Imaging Echelle Spectrograph) at the Nordlysstasjonen in Svalbard, Norway (78.2025N and 15.829E). The filter provides images of the resonant scattered spectra of N_2^+ 1N (0,1), (1,2), (2,3) bands and a neutral N_2 2P (0,3) band. *Ab initio* models were created for describing the populations of vibrational and rotational energy levels in both excited and ionised N_2 molecules in the ionosphere. In the rotational profiles the species are treated to be in thermal equilibrium, whereas the vibrational levels assume a non-thermal steady state time independent model.

Rotational temperatures were evaluated for different auroral forms for the N_2^+ (0,2) band from the magnetic zenith and along the meridian slit in HiTIES data from winter. A clear trend in neutral temperature is found, with higher values for times of lower energy precipitation. The relationship between resonant scattering of solar photons via N_2^+ and direct emission from electron impact on N_2 was evaluated qualitatively and quantitatively with HiTIES data from January-March 2007. A relationship was found that clearly indicates the emission profiles are a function of primary electron energy and solar shadow height when auroral arcs are partially sunlit during events of electron precipitation.

Contents

List of Figures

List of Tables

Declaration of Authorship

I, Olli-Pekka Jokiaho, declare that the thesis entitled

Spectral Modelling of Molecular Nitrogen in Aurora

and the work presented in the thesis are both my own, and have been generated by me as the result of my own original research. I confirm that:

- this work was done wholly or mainly while in candidature for a research degree at this University;
- where any part of this thesis has previously been submitted for a degree or any other qualification at this University or any other institution, this has been clearly stated;
- where I have consulted the published work of others, this is always clearly attributed;
- where I have quoted from the work of others, the source is always given. With the exception of such quotations, this thesis is entirely my own work;
- I have acknowledged all main sources of help;
- where the thesis is based on work done by myself jointly with others, I have made clear exactly what was done by others and what I have contributed myself;
- parts of this work have been published as: *Ann. Geo., 26, 4, 853-866, 2008*, *Ann. Geo., 27, 6, 2545-2553, 2009* and *Ann. Geo., 27, 9, 3465-3478, 2009*.

O. Jokiaho

29 September 2009

Acknowledgments

I would like to thank everyone who have helped and inspired me during my doctoral study. Most importantly my supervisor Prof Betty Lanchester and also Dr Nickolay Ivchenko for all the encouragement during the many years of work.

I would like to thank Prof Henry Risbeth for good company at swimming trips and many pub lunches, Prof Dirk Lummerzheim for scientific discussions and help with software analysis, Dr Geoff Daniels for helping me with the statistical part of this thesis and Matt Danby for providing insight into strategic approach and putting game theory into practice.

I would like to thank my peers Dan Whiter, Hanna Dahlgren, Mea Wedlund and Doctors Jo Sullivan, Björn Gustavsson and Anastasia Stockton-Chalk for company in long observing campaigns, advice and building of data management tools, Jeffrey Holmes and Margit Dyrland for all their logistical help in the arctic Svalbard.

I would like to use the opportunity to thank my parents and family for long distance support and patience with my absence from home.

Finally, but not least, this thesis would not have been possible without the diligence and love of Rita Priest and the culinary skills she mastered in filling all the delicious lunch boxes needed to see this work through and preventing the completion of this work spiraling into infinity.

I would like thank everybody else that has been a part of this PhD experience I have not mentioned here too, thank you very much.

Chapter 1

Introduction

1.1 Background

The primary topic of the thesis is the Aurora Borealis measured from the Nordlysstasjonen located at Adventdalen, Svalbard in Norway. More specifically, the emission spectra of diatomic molecules, which are important in the upper atmospheric auroral processes, are modelled, observed with instruments and analysed both qualitatively and quantitatively.

The region of Svalbard (78.2N 15.8E) offers a unique location for observation of the aurora as it is sufficiently dark at noon in winter and it is also at the correct geomagnetic latitude to observe dayside aurora with reduced interference from sunlight. The station is typically north of the auroral oval in the magnetic cusp during this time. It is ideally located to measure aurora with various shadow heights moving from night time over to twilight and noon over extended periods of time in the winter months.

A few paragraphs are now devoted to describing the large natural laboratory in which the observations occur. The Sun's gaseous interior and the molten core of the Earth form magnetic fields that extend out from their surfaces and into space. The Earth's magnetic field (EMF) resembles a dipole field that is offset from the geographic rotation axis fluctuating at around ten degrees. The Sun's magnetic field within the heliosphere forms the interplanetary magnetic field (IMF) carried out into the solar system by the solar wind. The outline of these large scale systems are seen in Fig. 1.1. The IMF lines are still attached to the solar surface and the rotation of the Sun winds up the magnetic fields into Parker spirals as seen in the left. The Earth's magnetosphere forms

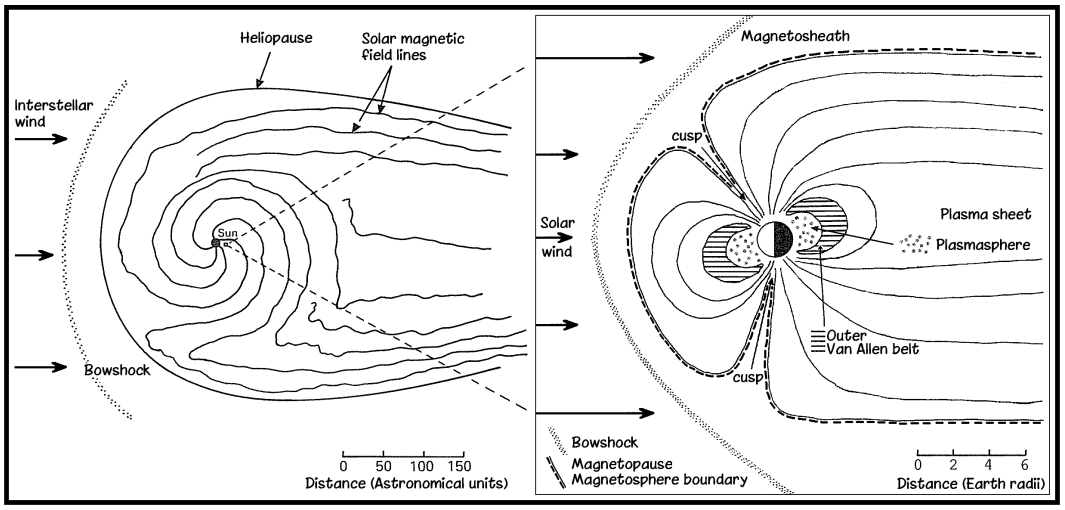

Figure 1.1: *The solar wind is carried radially out from the Sun, but the IMF is still attached to the rotating surface (left). The Earth is surrounded by its own magnetosphere that deflects most of the solar wind apart from a small fraction that under favourable conditions enter its plasma regions and current systems. [Figure by O. Jokiaho]*

a cavity within the solar wind seen in the right.

The solar wind is made of protons and electrons whose density and velocity are often increased by violent ejections of plasma that follow solar flares. The magnetopause is formed where the pressure balance reaches zero between the IMF and EMF. The terrestrial magnetosphere acts as a barrier to more than 99% of the solar wind deflecting it past the Earth. The dipole field is forced earthward at the dayside, typically 8-10 Earth radii, and dragged down wind several hundred Earth radii on the night side. A bow shock is created ahead of the dayside magnetopause where the solar wind encounters the leading edge of the EMF. The distance from the Earth of this boundary region responds to changes in the solar wind pressure, moving closer at high solar wind velocities. Between the bow shock and magnetopause there is a plasma rich region through which all solar wind incident on the Earth flows. This is known as the magnetosheath where the plasma is either deflected or is able to enter the Earth's magnetosphere.

The solar wind plasma has "frozen in" magnetic field. Both the strength and orientation play a crucial role in plasma gaining entry into the terrestrial magnetosphere and resulting in the production of aurora. When the IMF has a strong southern component relative to the ecliptic plane (i.e. anti-parallel to the EMF), the dayside magnetopause can magnetically reconnect with the solar wind. This method of plasma entry is dominant in these conditions. Similarly, northward IMF results in lobe and cusp reconnection.

These large scale phenomena form the background to the observations described in this thesis and are not directly part of the research project, which is entirely based on magnetic zenith measurements at one location. Charged particles entering the Earth's magnetosphere involve acceleration processes many of which are still unclear, guiding them by the Earth's magnetic field into the atmosphere where they create the aurora. During this process they suffer from elastic and inelastic collisions with the atmospheric constituents. The latter involve transfer of energy by dissociation, ionisation, excitation, heating the atmosphere and producing Brehmsstrahlung. The first four involve both primary incident electrons and locally produced secondary electrons, whereas the latter is produced by the primary species only. Ionisation breaks molecules apart into ions and electrons and excitation involves raising the energy levels of bound electrons. These processes involve transitions between electronic states, vibrational and rotational levels. These energy levels are quantised and when relaxed, release photons with very specific energies. These reactions take place in the thermosphere, where the neutral gas constituents are treated as thermal and are characterized by a temperature which follows the neutral temperature and influences the emission characteristics from the excited species. The neutral temperature profile of the atmosphere is seen in the middle of Fig. 1.2.

Molecular species of nitrogen and oxygen are the most abundant species of the atmosphere at low altitudes and lighter atomic and ionised species are relatively more abundant at higher altitudes. The main constituents of the aurora are emissions from

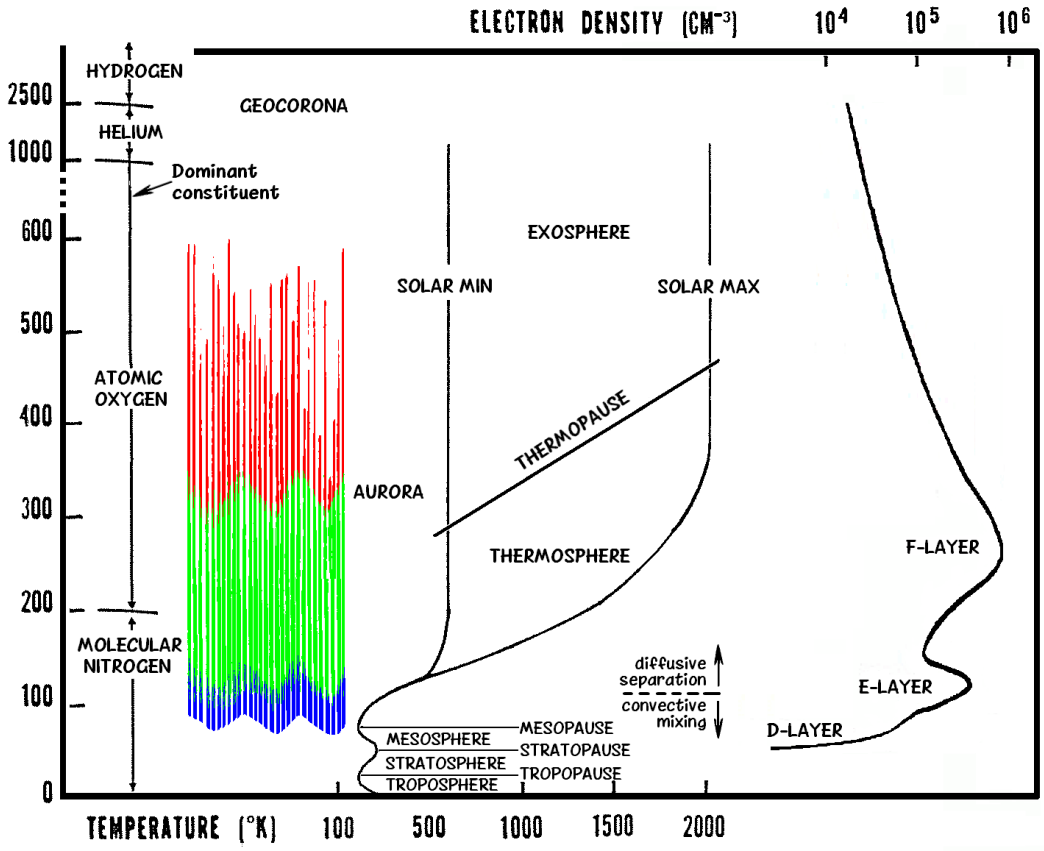

Figure 1.2: *Heights of the principal atmospheric elements at auroral heights, the neutral temperature profile for both quiet and active Sun and a schematic layout of ionospheric layers of electron density due to photoionisation. The electron concentration in the ionosphere changes depending on solar conditions and Sun-Earth geometry while retaining the altitude characteristics. [Figure by O. Jokiaho]*

these species. Emissions from molecular nitrogen are mainly seen in the UV-blue, but also in the red-IR range involving several band systems extending to the mid-wavelengths between the two domains. Fig. 1.3 shows the distribution of molecular emissions in the ionosphere. Atomic oxygen de-excites with wavelengths in the green and the red-IR range. These emissions are geographically confined to the magnetic polar regions and occur sporadically only at times of electron precipitation. Emission

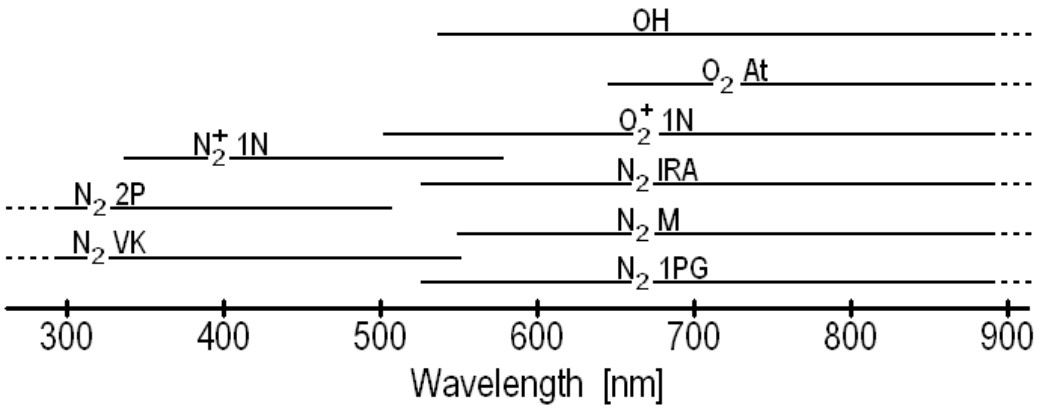

Figure 1.3: *Dominating molecular auroral emissions as a function of wavelength. [Figure by O. Jokiaho]*

characteristics depend on particle energy and hence depth of penetration into the atmosphere as well as the local atmospheric composition. It is separate from the only other type of optical phenomena occurring in the upper atmosphere, airglow, which is an omnipresent faint chemiluminescent glow of continuous emissions arising from discrete atomic and molecular chemical reactions and transitions (OH, O_2, O, Na) in the ionosphere due to photoionisation. It is low in intensity in visual wavelengths, but results in a night sky that is never perfectly dark.

The ionosphere is almost entirely created by ionisation from short wavelength solar radiation. Specific regions in the ionosphere develop known as ionospheric F, E and D layers. They do not follow a simple height differentiation, but instead are associated with different physical processes such as absorption characteristics of the atmosphere, recombination depending on atmospheric density and the changes in the relative species composition. A schematic diagram of the ionosphere is seen on the right of Fig. 1.2.

The high latitude ionosphere is of particular interest here because of the effect sunlight has when there is also auroral electron precipitation. The molecules most affected are N_2 and their ions. The research described in this thesis investigates and establishes

the relationship between resonant scattering of solar photons via N_2^+ and direct emission from electron impact on N_2.

1.2 Ionospheric reaction processes

The N_2^+ excited states are produced simultaneously with ionisation from the neutral N_2 ground state rather than excitation from the ion ground state, because the parent ion ground state populations would otherwise have to be unrealistically large [Whitten et al., 1971]. Especially the First Negative system has been used as a indirect measurement of ionisation rate and incident electron flux due to prompt emissions from the short lived state, which is also free of any cascading transitions [Omholt, 1971]. In turn, the neutral N_2 molecule is efficient in depleting the population of secondary electrons below 15 eV, producing N_2 in the excited electron states.

1.2.1 Creation of N_2^+

Photoionisation from solar UV radiation is the principal mechanism for producing the ionosphere and dominates the processes in the atmospheric creation of N_2^+ via

$$\mathrm{N_2} + \mathrm{h}\nu(< 79.6\mathrm{nm}) \rightarrow \mathrm{N_2^+} + \mathrm{e^-} \tag{1.1}$$

producing photoelectrons [Rees, 1989]. N_2^+ is also produced sporadically by precipitating electrons of magnetospheric origin [Degen, 1977]

$$\mathrm{N_2} + \mathrm{e^{-*}} \rightarrow \mathrm{N_2^+} + \mathrm{e^{-*}} + \mathrm{e^-} \tag{1.2}$$

trapped and accelerated by the Earth's magnetosphere, where e^{-*} is the primary electron and e^- the secondary electron. The N_2^+ emissions are excited by both processes in daylight and by the latter during the night. These processes depend on the incident solar wind and the ultraviolet spectrum of the Sun that follow the solar cycle.

There are also other processes that contribute to N_2^+ production [Fox et al., 1985]. These are charge transfer collisions resulting from collisions of neutral N_2 with atomic

oxygen and helium ions.

$$O^+ + N_2 \rightarrow N_2^+ + O \tag{1.3}$$

$$He^+ + N_2 \rightarrow N_2^+ + He \tag{1.4}$$

The possible energy levels of N_2^+ are $X^2\Sigma_g^+$ (15.5 eV), $A^2\Pi_u$ (16.7 eV), $B_2\Sigma_u^+$ (18.8 eV), $C^2\Sigma_u^+$ (23.5 eV) and $D^2\Pi_g$ (22.0 eV) [Rees, 1989]. These are electronic states whose nomenclature is described more in detail in Chapter 2. Excitation of the C and D states account for less than 1% of the total excitation. They suffer from strong predissociation and are therefore considered insignificant. Emissions occur in transitions from the A and B states to the ground X state. The Meinel (M) band is known as the $A^2\Pi_u \rightarrow X^2\Sigma_g^+$ transition in the near infrared with a typical lifetime of a few microseconds and the First Negative (1N) as the $B^2\Sigma_u^+ \rightarrow X^2\Sigma_g^+$ transition at the blue end of the visible spectrum with a typical lifetime measured in nanoseconds. For the 1N emissions Eqs. 1.1-1.2 represent the main contribution as the charge transfer processes such as reaction 1.3 can only produce N_2^+ in X and A states and reaction 1.4 only produces N_2^+ B very weakly.

1.2.2 Losses of N_2^+

The dominant effects in the losses of N_2^+ are via charge transfer by collisions with neutral species of O, O_2 and NO following Eqs. 1.5-1.8 [Fox et al., 1985].

$$N_2^+ + O \rightarrow NO^+ + N \tag{1.5}$$

$$N_2^+ + O \rightarrow O^+ + N_2 \tag{1.6}$$

$$N_2^+ + O_2 \rightarrow O_2^+ + N_2 \tag{1.7}$$

$$N_2^+ + NO \rightarrow NO^+ + N_2 \tag{1.8}$$

Molecular nitrogen ions react with atomic oxygen converting into atomic oxygen ions and nitric oxide ions. If the reaction is with molecular oxygen, then the end product is a molecular oxygen ion. A rearrangement resulting from a collision with nitric

oxide produces nitric oxide ions. The process resulting in nitric oxide ions is favoured due to nitric oxide having a lower ionisation potential (9.3 eV) than atomic or molecular species of oxygen (12.1 eV) [Rees, 1989]. The relative importance of the processes, however, depends on the concentrations and reaction rates of the species.
Another loss is dissociative recombination via

$$\mathrm{N_2^+ + e \rightarrow N + N}, \tag{1.9}$$

where auroral activity occurs, typically at higher ionospheric altitudes.

1.2.3 Other Processes

Additional alteration of vibrational levels without changing the total $\mathrm{N_2^+}$ population occurs [Fox et al., 1985] as a result of:
electron induced fluorescence

$$\mathrm{N_2^+(X^2\Sigma_g^+) + e \rightarrow N_2^+(A^2\Pi_u, B^2\Sigma_u^+)}, \tag{1.10}$$

resonant absorption of solar photons

$$\mathrm{N_2^+(X^2\Sigma_g^+) + h\nu \rightarrow N_2^+(A^2\Pi_u, B^2\Sigma_u^+)}, \tag{1.11}$$

which lead to prompt emissions

$$\mathrm{N_2^+(A^2\Pi_u, B^2\Sigma_u^+) \rightarrow N_2^+(X^2\Sigma_g^+) + h\nu}, \tag{1.12}$$

and quenching effects leading to the loss or addition of vibrational energy in collisions with its neutral counterpart

$$\mathrm{N_2^+(X, v'' > 0) + N_2 \leftrightarrow N_2^+(X, v = 0) + N_2} \tag{1.13}$$

$$\mathrm{N_2^+(X, v'' > 0) + O \leftrightarrow N_2^+(X, v = v'' - 1) + O} \tag{1.14}$$

$$\mathrm{N_2^+(X, v'' > 0) + O_2 \leftrightarrow N_2^+(X, v = v'' - 1) + O_2}. \tag{1.15}$$

The kinetic energy associated with the ions before the collision appears as the kinetic energy of the neutral after the collision and vice versa. These processes efficiently transfer the kinetic energy from ions to the neutrals [Rees, 1989].

1.3 Thesis structure

The vibrational populations and rotational spectra of various molecular nitrogen bands used by the optical instruments in the Space Environment Group at the University of Southampton, UK, have been modelled *ab initio*. In particular in this work, the N_2^+ 1N emission bands are studied during events of electron precipitation into the ionosphere in non-sunlit, twilight and sunlit conditions with the HiTIES (High Throughput Imaging Echelle Spectrograph) instrument.

An introduction to spectroscopic nomenclature, part of which is used in this thesis, is given in chapter 2. This highlights that certain styles of notation have historical rather than logical representation. The theoretical basis of modelling quantum rotation-vibration spectra in electronic transitions is then set out in chapter 3.

The instruments used for the above measurements are described in chapter 4 and also the work particular to the operation of the instruments and analysis of their measurements. To achieve the science objectives for studying the N_2^+ molecules with HiTIES, a mosaic filter was designed for the spectrograph. The design process was an independent project and is described in the section 4.1.1. Section 4.2.1 describes modelling of spectral bands extended to all the bands of interest that had optical filters built for and in use by HiTIES and the multi spectral imager ASK (Auroral Structure and Kinetics). The total band transmittances were calculated as a function of rotational temperature on the basis of knowing the spectral characteristics of the band systems in question.

Chapter 5 describes the building of the spectral model for the N_2^+ 1N (0,2) band, which was used as a diagnostic tool for neutral temperature and emission height variations with supporting measurements from the Svalbard Eiscat Radar (ESR). The radar and modelling results confirm that the measured average energies are a lower limit for an estimate of the characteristic energy. In each event the energy distribution is clearly made up of more than one spectral shape. This work emphasises the need for high time resolution as well as high spectral resolution.

A time independent steady state model of production and loss terms of N_2^+ is developed to be used in combination with the Space Environment Group's ion chemistry model and HiTIES data to quantify the effect of solar resonant absorption. Similarly, in another steady state model the population distributions of N_2 excited electron states were modelled in order to measure the cascade contribution into two specific 1P bands. This was important in constructing an emission cross section to be used with the ion chemistry code for the modelled 1P emissions that are imaged by the ASK instrument. It was used as a part of work conducted in Ashrafi et al. [2009] and Lanchester et al. [2009]. The modelling of these electronic and vibrational populations is described in detail in Chapter 6.

Chapter 7 shows how resonance scattering dominates auroral N_2^+ emissions above, and direct emission dominates below a certain altitude. This altitude is governed by the ion lifetime, which in turn depends on the atmospheric conditions e.g. solar minimum/maximum. Therefore, when sunlight is present the height integrated profiles are dependent not only on the shadow height but also on the peak energy of the precipitating electrons.

Chapter 2

Spectroscopic notation

Notation of energy levels of atomic and molecular states can be rather confusing between physicists and spectroscopists. Terminology has developed historically and not always logically, therefore a brief description is given here. A more comprehensive reading of this section can be found in Jevons [1932] and Herzberg [1950].

Partially filled outer electron shells of valence electrons and electron orbitals of atoms result in chemical bonding and reactivity. The filled and localised inner shells of atoms contribute very weakly to the overall molecular properties and their electronic structure. It is the atomic valence electrons which are responsible for molecular electronic spectra.

Each electron is described by quantum numbers, which describe values of conserved quantities of quantised systems such as energy levels of electrons in atoms and molecules. Mainly, n is the principle quantum number and l is the orbital quantum number.

A *Configuration* is given as

$$n(l)^x \tag{2.1}$$

where x is the number of electrons eg.

$$1s^2 2s^2 2p^6 3s^2 3p^6 \tag{2.2}$$

A *State* is defined as

$${}^{M_S}(L)_J = {}^{2S+1}(L)_{L+S} \tag{2.3}$$

where J is the total angular momentum, a combination of spin and orbital terms, M_S is

the electron spin multiplicity and

$$S = \sum_i s_i \tag{2.4}$$

is the net electron spin. These are for example singlet, doublet and triplet states governed by

$$M_S = 2S + 1 \tag{2.5}$$

where S is the net electron spin angular momentum in the system, each electron contributing either $-\frac{1}{2}$ or $+\frac{1}{2}$. Accordingly, for a singlet state the total electron spin quantum number 0, $M_0 = 1$ and triplet $M_1 = 3$. The way spins govern spectral lines is that electron spin affects the splitting in wavelength and nuclear spin affects the statistical weight in the intensity of fine spectral lines.

By textbook definition and to avoid confusion, a lower case s and l usually refer to a one electron system and a capital S and L to a poly-electronic system. The labels stand for **S**harp, **P**rincipal, **D**iffuse, **F**undamental according to their spectral properties and follow alphabetically from the latter onwards. Small letters are used to describe individual electrons and capitals refer to a resultant state of electronic configuration in both atomic and molecular systems.

For single electrons in molecules the notation for the electron orbital angular momentum becomes

$$\lambda = \sigma, \pi, \delta, \phi ... \text{ for } \lambda = 0, 1, 2, 3, ... \tag{2.6}$$

The atomic equivalent of λ is

$$l = s, p, d, f, ... \text{ for } \mathrm{l} = 0, 1, 2, 3... \tag{2.7}$$

For molecules Λ is the multiplicity of $\hbar$ and represents the z-component of the electronic orbital angular momentum which lies along the internuclear axis, where

$$\Lambda = \Sigma, \Pi, \Delta, \Phi, \Gamma ... \text{ for } \Lambda = 0, 1, 2, 3, 4... \tag{2.8}$$

The atomic equivalent of Λ is

$$L = S, P, D ... \text{ for } \mathrm{L} = 0, 1, 2... \tag{2.9}$$

for electronic states. This is caused by precession of L with the internuclear electric field along the internuclear axis. Hence the relationship between λ and L is that λ represents the parallel internuclear axis component of the angular momentum of an individual electron related to l by $\sqrt{l(l+1)}$. The relationship between Λ and L similarly is the parallel internuclear axis component of the orbital angular momentum of $\sqrt{L(L+1)}$. This motion forms the various electronic states a molecule can occupy as seen in the potential energy diagrams. The molecular electronic state is finally specified as

$$^{M_S}(\Lambda)_\Omega = ^{2S+1}(\Lambda)_{\Lambda+\Sigma} \quad e.g. \quad ^3\Delta_2 \tag{2.10}$$

For di and polyatomic molecules symbols σ and π indicate cylindrical symmetry of the molecular orbital wavefunction with respect to the internuclear axis (σ indicates symmetry, π non-symmetry). These can also be written as post-superscript $^+$ for symmetric and $^-$ for antisymmetric. For homonuclear diatomic molecules, subscripts g and u (gerade and ungerade) indicate parity and further symmetry of molecular orbitals through an inversion from any part of the molecule through the center point of the molecule to the opposite side. If the wavefunction of the orbital changes sign the parity subscript is u, if not then the subscript is a g. The gerade symbols are ignored if the molecule is not symmetric.

A *state* can now be written as e.g.

$$^3\Sigma_g^+$$

In atoms, a *term* includes both a *configuration* and a *state*. A *transition array* is a transition between two configurations eg.

$$3s - 4p \tag{2.11}$$

A *multiplet* includes all transitions between two terms eg.

$$3s^2p - 4p^2s \tag{2.12}$$

A *line* is a transition between two levels eg.

$$3s^2p_{3/2} - 4p^2s_{1/2} \tag{2.13}$$

In molecules, several states form *members of family*. These are designated in the order of increasing energy, but due to historical reasons the order does not always follow alphabetically. The ground state is labelled as capital X and the excited states of the same multiplicity are labelled as capital A, B, C... etc usually with increasing energy, but not always. If the multiplicity is different, those state are labelled as small case a, b, c... etc. An exception to this format is the N_2 molecule, in which excited singlet states are small case and excited triplet states are capital.

In designating a molecular emission transition, upper level is given first followed by the lower state.

$$N_2^+ B^2\Sigma_u^+(0) \; - \; N_2^+ X^2\Sigma_g^+(2) \tag{2.14}$$

so that the equation is the same for both excitation and emission though initial and final states are reversed. This is opposite to atomic notation of energy levels, which refers to the ionised state, whose energies are usually negative.

$$OI\ ^3P -^1 D \tag{2.15}$$

To distinguish the transition direction, an arrow can replace the hyphen if necessary.

A molecular *band system* describes all transitions between two molecular electronic states eg.

$$B^3\Pi \rightarrow A^3\Sigma \tag{2.16}$$

in which vibrational and rotational degrees of freedom are described with quantum numbers v and J respectively. This is described in Chapter 3 in more detail. A *band* is one of these transitions and is between two vibrational levels eg.

$$B^3\Pi(v' = 3) \rightarrow A^3\Sigma(v'' = 1) \tag{2.17}$$

When all bands arise from the same v' vibrational level, this is referred to as a *progression*

$$B^3\Pi(v' = 2) \rightarrow A^3\Sigma \tag{2.18}$$

and for all bands that Δv=constant, this is called a *sequence* eg.

$$B^3\Pi(v') \rightarrow A^3\Sigma(v'' = v' - 2) \tag{2.19}$$

A *rotational line* is a result of a transition between rotational energy levels within a vibrational band eg.

$$B^3\Pi(v' = 3, J' = 3) \rightarrow A^3\Sigma(v'' = 2, J'' = 4) \tag{2.20}$$

A *branch* is called a series of lines with $\Delta J = J' - J'' = constant$ governed by selection rules. For example $\Delta J = 0$ is referred to as Q, $\Delta J = -1$ referred to as R and $\Delta J = 1$ referred to as P branch.

Another piece of notation that is useful to remark here is the physical meaning of oxidation number. Chemists and physicists use terminology, which can be confusing for the unfamiliar reader. In chemistry, the oxidation number is equal to the charge of the ion in simple ions and the degree of ionisation is suffixed by roman numerals. In physics however, this is set to represent the ionisation state instead so that for example OI means neutral (O), OII singly ionised (O^+) and OIII doubly ionised oxygen (O^{2+}).

Chapter 3

Theory of rotational temperatures

Molecular spectra are described well in Jevons [1932] and Herzberg [1950] and the following chapter is a summary of the relevant theory used in this work.

The total molecular wave function Ψ_{total} is a product of electronic Ψ_e and nuclear components. The nuclear wave function is subdivided into vibrational Ψ_v, rotational Ψ_r and nuclear spin Ψ_{ns} interactions so that

$$\Psi_{total} = \Psi_e \Psi_v \Psi_r \Psi_{ns}. \tag{3.1}$$

The total Hamiltonian is a sum of the individual Hamiltonians for each interaction. The eigenstates are found as solutions to the Schrödinger equation. Because of the independent variables in multiplicative wave function, the energy is a sum of independent energies. Therefore, the molecule holds quantised potential energy in electronic structure, nuclear vibration and rotation in a transition between two energy levels that can be presented as

$$\Delta E = hc/\lambda = \Delta E_e + \Delta E_v + \Delta E_R. \tag{3.2}$$

The molecular motion is schematically described in Fig 3.1.

3.1 Wavelength distribution

The balance of electrostatic forces between two nuclei, which are bound together by outer shared electrons results in a vibrating internuclear separation. This dis-

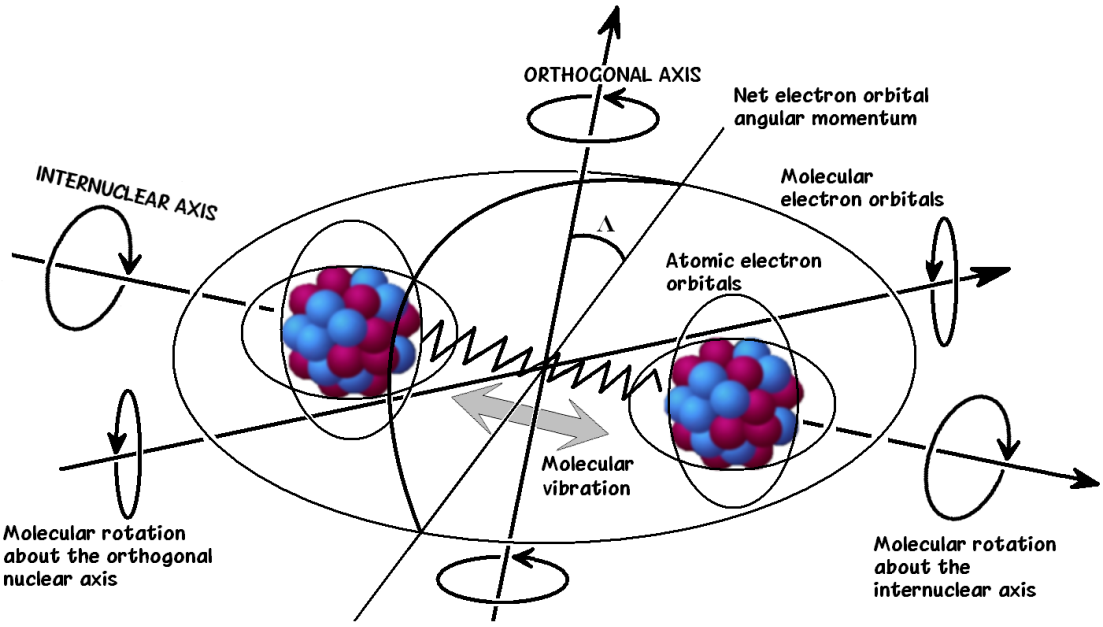

Figure 3.1: *Relevant components of electron cloud motion with nuclear vibration and rotation that govern the molecular properties. [Figure by O. Jokiaho]*

placement in the bond length forms the potential energy function known as the Morse potential. Molecular bonding between atoms is often treated as rigid rods, but this is spectroscopically not true. The bonding is better described as springs between the nuclei, some stronger, others weaker and depends on the multiplicity of the bond. The Morse function

$$U(r) = T_e + D(1 - e^{-\beta(r-r_e)})^2 \tag{3.3}$$

is a function of separation of a molecular state and a ground molecular state T_e, dissociation energy D, equilibrium internuclear distance r_e and molecular constant β.

$$D = \frac{\omega_e^2}{4\omega_e\chi_e} \qquad \beta = \sqrt{\frac{8\pi^2 c}{h}\mu\omega_e\chi_e} \tag{3.4}$$

where is $\omega_e\chi_e$ is an anharmonic constant. The molecule also has a rotational degree of freedom. It can rotate about the perpendicular component to the internuclear axis

about the center of gravity. Rotation about the internuclear axis has negligible effect.

In Newtonian mechanics the two nuclei system can be replaced by a single body vibrator. The reduced mass is

$$\mu = \frac{m_1 m_2}{m_1 + m_2} \tag{3.5}$$

Steady state solutions of the Schrödinger equation exist for quantised vibrational energy levels and quantised rotational energy levels. The energy eigenvalues have vibrational G and rotational terms F that are a function of the vibrational quantum number n and the rotational quantum number J.

$$\epsilon_{n,j} = G(v) + F(J) \tag{3.6}$$

$$\epsilon_{n,j} = \left(v + \frac{1}{2}\right)\omega_e - \omega_e\chi_e\left(v + \frac{1}{2}\right)^2 + B_v J(J+1) - D_v J^2(J+1)^2 \tag{3.7}$$

where the four terms are: equally spaced energy level array of non-rotating simple harmonic oscillator, anharmonic oscillator energy correction, rigid rotator energy component and non-rigid energy correction, where

$$\omega_e = \left(\frac{1}{2c\pi}\right)\sqrt{\frac{\kappa}{\mu}}, \qquad B_v = \frac{h}{8I_n c\pi^2} = B_e - a_e\left(v + \frac{1}{2}\right) \tag{3.8}$$

$$B_e = \frac{h}{8\pi^2 c I_e}, \qquad I_e = \mu r_e^2, \qquad a_e = \frac{6\sqrt{\omega_e\chi_e B_e^3}}{\omega_e} - \frac{6B_e^2}{\omega_e} \tag{3.9}$$

$$D_v = D_e - \beta_e(n+1), \qquad D_e = \frac{4B_e^3}{\omega_e}, \tag{3.10}$$

$$\beta_e = D_e\left(\frac{8\omega_e\chi_e}{\omega_e} - \frac{5a_e}{B_e} - \frac{a_e^2\omega_e}{24B_e^3}\right) \tag{3.11}$$

χ_e is the anharmonicity constant, v is the vibrational quantum number, ω_e is the classical vibrational frequency of the bond about equilibrium length i.e. band origin, κ

is the bond strength, μ is the reduced mass, h is Planck's constant, c is velocity of light, I is the moment of inertia about the perpendicular axis to that of the internuclear axis, J is the rotational quantum number, B_v is a rotational constant that refers to the moment of inertia at a vibrational level, B_e is the rotational term corresponding to Birge's rule and is effectively a measure of the moment of inertia of the molecule at equilibrium bond length, a_e is the vibration-rotation interaction constant and β_e is a vibrational correction to the centrifugal distortion term.

The observed vibration rotation emission spectra will then be observed at

$$\nu_{n,j} = G'(v') - G''(v'') + F'(J') - F''(J'') \tag{3.12}$$

$$\begin{aligned} \nu_{n'j',n''j''} = & \left(\left(n' + \frac{1}{2} \right) \omega'_e - \omega'_e \chi_e \left(n' + \frac{1}{2} \right)^2 \right) \\ & + \left(B'_{v'} J'(J'+1) - D'_{v'} J'^2 (J'+1)^2 \right) \\ & - \left(\left(n'' + \frac{1}{2} \right) \omega''_e - \omega''_e \chi_e \left(n'' + \frac{1}{2} \right)^2 \right) \\ & + \left(B''_{v''} J''(J''+1) - D''_{v''} J''^2 (J''+1)^2 \right) \end{aligned} \tag{3.13}$$

By standard notation, single prime corresponds to a vibrational level in a higher energy electronic state than double prime. As a result of the transition, P branch ($\Delta J = -1$), R branch ($\Delta J = +1$) and Q branch ($\Delta J = 0$) where $\Delta J = J' - J''$, can then be observed from the spectrum. A set of selection rules governs the emission. If both upper and lower electronic states involved in the transition have no electronic angular momentum component along the molecular axis (i.e. $\Lambda = \Sigma$), then $\Delta J = \pm 1$. For all other transitions $\Delta J = 0, \pm 1$. Further restriction is that a transition cannot occur from $J = 0$ state to another $J = 0$ state. For the Q-branch this means that no line appears at the band origin. Selection rules arise from the properties of wave function symmetries in the transition strength matrix element, which yields a non-zero value only under certain conditions.

Branch	*Selection rule*	*Wavenumber*
P	$J' = J - 1, J = 0, 1, 2...$	$\nu_P = \omega_e - (B'_v + B''_v)J'' + (B'_v - B''_v)J''^2$
Q	$J' = J,\ J = 1, 2, 3...$	$\nu_Q = \omega_e + (B'_v - B''_v)J'' + (B'_v - B''_v)J''^2$
R	$J' = J + 1, J = 0, 1, 2...$	$\nu_R = \omega_e + 2B'_v + (3B'_v - B''_v)J'' + B'_v - B''_v)J''^2$

Table 3.1: *Rotational wavelength distribution of diatomic molecules.*

Some properties of symmetry can also give rise to two satellite branches in each P, R, and Q-branches but will not be discussed here.

Table 3.1 shows the wavenumbers of the vibration-rotation spectra using the appropriate selection rules. For the sake of simplicity, we have ignored the anharmonicity and non-rigid terms.

The rotational quantum number here corresponds to the vibrational state in the lower electronic state. Hence standard textbook notation is always

$$J = J'' \tag{3.14}$$

unless referenced otherwise. For $B'_v > B''_v$, which indicates internuclear separation in the higher state is greater than in the lower state, the band head forms in the P-branch and in the opposite case applies for the R-branch. Band head by definition is the wavelength where the Fortrat parabola has a turning point. In the case of $B'_v \sim B''_v$, no band head will occur and all the lines of the Q-branch nearly coincide at $\tilde{\nu} \sim \omega_e$.

The well known Fortrat parabola, which is caused by the relationship between the linear and non-linear terms in the energy equations can be seen by plotting the rotational quantum number as a function of wavenumber. This fine structure occurs for every vibration-rotation electronic transition.

Spectroscopic constants are always given in wavenumber in vacuum. Therefore a conversion to wavelength in air

$$\frac{\lambda_{vac} - \lambda_{air}}{\lambda_{air}} = (n-1) = 6.4328 * 10^{-5} + \frac{2.94981 * 10^{-2}}{146 - \tilde{\nu}^2_{vac}} + \frac{2.5540 * 10^{-4}}{41 - \tilde{\nu}^2_{vac}} \tag{3.15}$$

has been applied from Morton [1991], where λ_{vac} is the wavelength in vacuum, λ_{air} is the wavelength in air, n is the refractive index of air and $\tilde{\nu}$ is the wavenumber in vacuum.

3.2 Intensity distribution

Emission intensity, or emission rate, defined as energy emitted per second is given by

$$I_{v''J''}^{v'J'} = A_{v'v''} N_{v'J'} h\nu \tag{3.16}$$

and is the energy radiated at classical frequency ν per second into unit solid angle from number of molecules $N_{n'J'}$ at state n' from unit volume of optically thin emitting gas. The Einstein coefficient for spontaneous emission is the $n' \longrightarrow n''$ transition probability per second of an emitting molecule and is defined as

$$A_{v'v''} = \frac{64\pi^4}{3h} \nu_{v'v''}^3 |R_{v'v''}|^2 \tag{3.17}$$

for transitions between non degenerate levels only, where $|R_{n'n''}|^2$ is the matrix element of the transition. The Einstein coefficient is the probability of spontaneous emission per emitter per second. For degenerate levels the formula has to be modified as

$$A_{v'v''} = \frac{64\pi^4}{3h} \nu_{v'v''}^3 \frac{\sum |R_{v_i'v_j''}|^2}{g_v} \tag{3.18}$$

where i and k refer to the degenerate sublevels and the sum is over all possible combinations of transitions. This can be rewritten as

$$A_{v'v''} = \frac{64\pi^4}{3h} \nu_{v'v''}^3 \frac{S_{v'v''}}{g_v} \tag{3.19}$$

where the degeneracy factor is

$$g_v = dd_v. \tag{3.20}$$

The electron spin $d = 2S + 1$ for $\Lambda = \Sigma$ and $d = 2(2S + 1)$ for $\Lambda \neq 0$ and rotational degeneracy $d_v = 2J+1$; for example for singlet transitions degeneracy is simply $g_v = d_v$.

The relationship between wavenumber $\tilde{\nu}$ and classical frequency ν is

$$\tilde{\nu} = \nu/c = 1/\lambda, \tag{3.21}$$

where $1/\lambda$ is expressed in inverse centimeter and is often used in spectroscopy as a convenient measure of energy. The thermal population distribution of rotational levels with associated degeneracy is given by

$$N_J = \frac{N}{Q_r}(2J' + 1)e^{-E/kT} \tag{3.22}$$

where Q_r is the rotational state sum and the energy is given by $E = F(J')hc/kT$. We can now substitute N_J and $A_{n'n''}$ into the intensity formula.

$$I^{v'J'}_{v''J''} = \frac{64\pi^4\nu^4_{v'v''}Nc}{3Q_r}\sum |R_{v'_iv''_j}|^2 e^{-F(J')hc/kT}. \tag{3.23}$$

In electric dipole radiative transitions, all of the transition probability parameters of a quantised system are controlled by a transition strength matrix element.

$$S^U_L = \sum |R_{v'_iv''_j}|^2 = |\int \Psi_{upper} * M\Psi_{lower}d\tau|^2 \tag{3.24}$$

where $\sum |R_{v'_iv''_j}|^2$ is the transition moment, Ψs are the total wavefunctions, M is the dipole moment and $d\tau$ is the volume element. The solution to the integral is

$$S^{v'J'\Lambda'}_{v''J''\Lambda''} = R^2_e(\overline{r}_{v'v''})\ q_{v'v''}\ S^{J'\Lambda'}_{J''\Lambda''} \tag{3.25}$$

This is the total line strength. The three products control the electronic, vibrational and rotational line strengths respectively. $R^2_e(\overline{r})$ conrols the overall magnitude, $q_{n'n''}$ is the Franck-Condon factor (FC) for vibrational excitation and intensity distribution. The FC factor describes the probability of excitation, which is the value of the overlap integral between two nuclear wave functions, related to the efficiency of the transition between two states. The product of the first two factors is also known as the band strength ($S_{n'n''}$) and is often controlled by the FC factors alone. $S^{J'\Lambda'}_{J''\Lambda''}$ is the transition moment matrix element i.e. Hönl-London factor, that describes the rotational line strength and intensity distribution in different branches (P, R, Q etc). Equation 3.23 hence becomes

$$I^{v'J'}_{v''J''} = \frac{64\pi^4\nu^4_{v'v''}Nc}{3Q_r}S^{J'\Lambda'}_{J''\Lambda''}e^{-F(J')hc/kT}. \tag{3.26}$$

where only the part of the line strength that depends on J is used. The various $S^{J'\Lambda'}_{J''\Lambda''}$ Hönl-London factors for branch series emission spectra for $\Delta\Lambda = 0$ [Herzberg, 1950] are

$$S^R = \frac{(J'+\Lambda')(J'-\Lambda')}{J'}, \qquad S^Q = \frac{(2J'+1)\Lambda'^{\,2}}{J'(J'+1)}, \qquad S^P = \frac{(J'+1+\Lambda')(J'+1-\Lambda')}{J'+1} \tag{3.27}$$

for $\Delta\Lambda = +1$

$$S^R = \frac{(J'+\Lambda')(J'-1+\Lambda')}{4J'}, \quad S^Q = \frac{(J'+\Lambda')(J'+1-\Lambda')(2J'+1)}{4J'(J'+1)}, \quad S^P = \frac{(J'+1-\Lambda')(J'+2-\Lambda')}{4(J'+1)} \tag{3.28}$$

and for $\Delta\Lambda = -1$

$$S^R = \frac{(J'-\Lambda')(J'-1-\Lambda')}{4J'}, \quad S^Q = \frac{(J'-\Lambda')(J'+1+\Lambda')(2J'+1)}{4J'(J'+1)}, \quad S^P = \frac{(J'+1+\Lambda')(J'+2+\Lambda')}{4(J'+1)} \tag{3.29}$$

Change in the orbital angular momentum during a transition determines the relative brightness between the P, R and Q branches. For example in a $\Delta\Lambda = -1$ emission, the Q-branch is the strongest band feature. The sum of all Hönl-London factors to a given level are always proportional to the statistical weight of that level. This is the rotational sum rule

$$\sum_{J''} S_{J'J''} = 2J' + 1 \tag{3.30}$$

These factors can be simplified, for example if $\Lambda = \Sigma$ and $\Delta\Lambda = 0$, then

$$2S^P_J = 2S^R_J = J' + J'' + 1, \qquad 2S^Q_J = 0. \tag{3.31}$$

As for the Maxwell-Boltzmann distribution law, the rotating molecules are strongly coupled to gas kinetics by collisions and excitation so that thermal equilibrium can be assumed.

$$T_{rotation} = T_{excitation} \tag{3.32}$$

If no change in the angular momentum occurs in the molecule with colliding electrons and if no redistribution occurs in the excited state, the value of rotational constant used here must correspond to the neutral N_2 ground state B''' from where the excitation takes

place, instead of that of the excited N_2^+ level B'. In fact, if B' was used the temperature obtained would be smaller by a factor of B'_v/B''_v [Ginsburg et al., 1941]. The value of J in the exponential term must correspond to the initial state of the transition. For emission, that is the higher level J'. It is assumed that the transition probability is constant for all rotational lines across the vibrational band. The rotational temperature only governs the vibrational band shape. It is independent of the total vibrational band intensity and remains constant. Taking into account that $F(J') = BJ(J+1) + DJ^2(J+1)^2$, therefore the intensity for rotational lines become

$$I_{v''J''}^{v'J'} = \frac{64\pi^4\nu_{v'v''}^4 Nc}{3Q_r} S_{J''\Lambda''}^{J'\Lambda'} e^{-B'''J'(J'+1)+D'''J'^2(J'+1)^2hc/kT_r}. \tag{3.33}$$

The splitting of each rotational energy level into two components occurring with all $\Lambda \neq 0$ states arises from the interaction between the magnetic field set up by the rotating molecule and the field along the internuclear axis. The splitting between the rotational levels only amounts a fraction of a cm^{-1} for Π-states and considerably less for Δ-states and is referred to as the Λ-type doubling. These rotational term series are usually distinguished by subscripts c and d (historically a and b) becoming gradually wider as J increases. This type of doubling is independent of electron spin.

For electron spin, each energy level for a given J consists of 2S+1 components and is referred to as doublet splitting or more generally, electron spin multiplicity splitting.

In a band, lines with a constant J'-J'' and a constant K'-K'' constitute a branch. If both of these factors are equal they are known as main branches and those for which the two factors are unequal as satellite branches.

Multiplet Σ states always belong to Hund case B, multiplet Π, Δ... belong to intermediate case a and b

3.3 Nuclear statistics

Nuclear statistics is referred to as the *hyperfine structure* in rotational line spectra and arises due to properties of the total wavefunction symmetries. The total molecu-

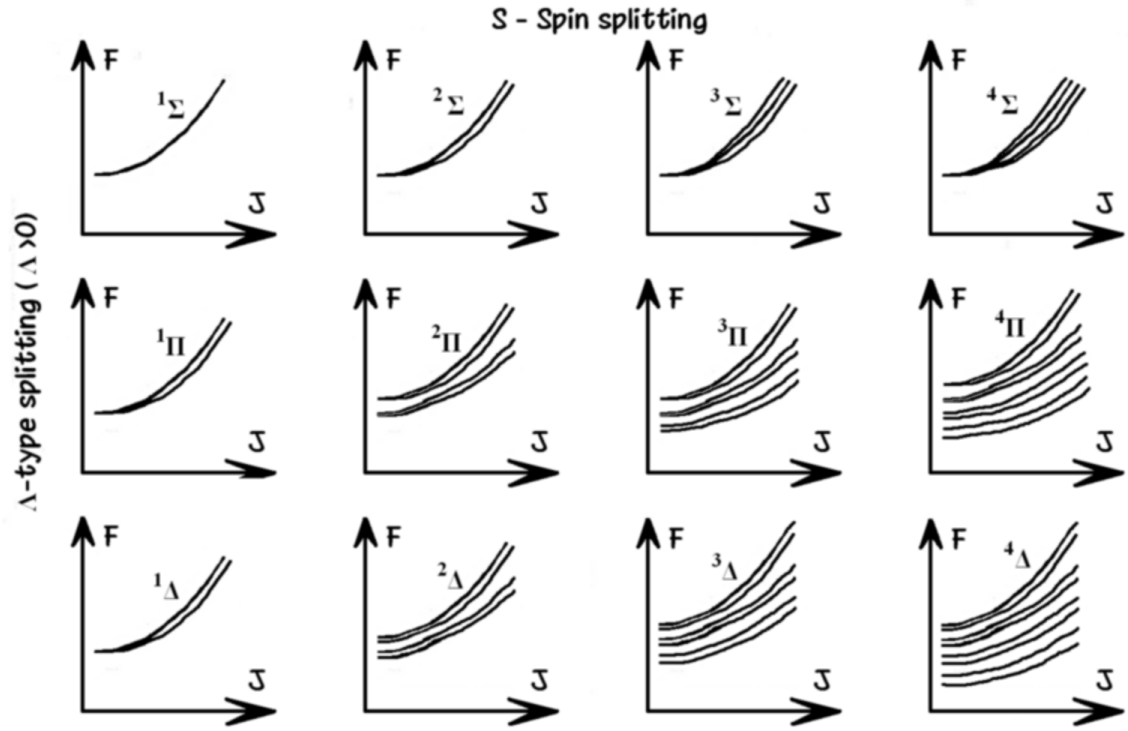

Figure 3.2: *A schematic of Λ-type splitting and spin splitting of rotational lines. [Figure by O. Jokiaho]*

lar wavefunction can either change sign with respect to reflection at the origin or not. These wavefunctions are referred to as negative (-) and positive (+) levels accordingly and correspond to either odd or even values of J. For example, if the total molecular eigenfunction depends on the rotational component alone (for $\Lambda = 0$) then even values of J are positive and odd values of J are negative, but if the electronic wavefunction changes sign by reflection at the origin then this parity is reversed. As an important selection rule positive levels can only combine with negative levels and vice versa. This is in harmony with the earlier selection rule $\Delta J = \pm 1$ when $\Lambda = 0$ and $\Delta J = 0, \pm 1$ for $\Lambda \neq 0$. In the case of the electronic state having $\Lambda \neq 0$ then rotational states are doubly degenerate in comparison to $\Lambda = 0$. This means each J has a positive and negative level of equal energy. The following discussion is for the $\Lambda = 0$ states only.

For homonuclear molecules such as N_2 and O_2 these positive or negative states are called symmetric or antisymmetric in the nuclei. As before, either even or odd levels of J are symmetric and the remaining levels antisymmetric. Spin vectors I form a resultant T, which is the total nuclear spin of the molecule. A homonuclear molecule has $I_1 = I_2 = I$.

$$T = 2I, 2I - 1, ..., 0 \tag{3.34}$$

and there are $M = 2T + 1$ degenerate states, where M is the statistical weight. The intensity ratio for a homonuclear molecule between strong and weak lines for each of the two nuclei having spin I is given by

$$R = \frac{I + 1}{I}. \tag{3.35}$$

Even values of T occur for symmetric levels and odd values of T for antisymmetric levels. Following the discussion above it can be seen how the different values of nuclear spin affect the observed hyperfine rotational spectra.

Starting with $I = 1$, the resultant nuclear spin can have values $T = 2, 1, 0$ and their corresponding degeneracy $M = 5, 3, 1$. That is, symmetric levels have degeneracy of 6 and antisymmetric 3. Therefore a molecule having nuclei with spin $I = 1$ forms an intensity alternation of 2:1 between neighbouring rotational lines. This is observed for N_2.

When $I = \frac{1}{2}$, it follows that $T = 1, 0$ and $M = 3, 1$. That is, symmetric levels have degeneracy of 1 and antisymmetric levels have degeneracy of 3. This means the intensity alternation between even and odd J is 1:3. This is observed for H_2.

$I = 0$ results in $T = 0$, $M = 1$ and $R = \infty$. This is correct as every other rotational line is missing i.e. either odd values of J or even values of J do not exist. This is indeed observed for O_2.

Molecular constants for the modelling of synthetic spectra of molecular nitrogen bands can be found in Lofthus et al. [1977].

3.4 Summary of strict selection rules and degeneracy factors

A molecular transition is allowed by the selection rules when the transition moment matrix (matrix element of the electric dipole moment) is non-zero and vice versa. These selection rules for diatomic electronic rovibronic transitions for rotational quantum numbers are:

$$\Delta J = 0, \pm 1 \qquad J = 0 \nleftrightarrow J = 0 \tag{3.36}$$

No strict selection rules govern vibrational transitions. The parity selection rule is

$$+ \longleftrightarrow - \tag{3.37}$$

except for $\Sigma - \Sigma$ transitions

$$+ \nleftrightarrow - \tag{3.38}$$

For identical nuclei

$$s \nleftrightarrow a \tag{3.39}$$

nuclei of equal charge

$$g \longleftrightarrow u \tag{3.40}$$

These selection rules have been described in Jevons [1932]. Electron spin is dealt with by setting the Hund case to either a or b. This is governed by the electron spin either coupling along internuclear axis (a) or orthogonally to the internuclear axis i.e. rotational axis (b). For both Hund cases the electronic quantum numbers follow

$$\Delta \Lambda = 0, \pm 1 \tag{3.41}$$

and electron spin multiplicity selection rule

$$\Delta S = 0. \tag{3.42}$$

For the Hund case a specifically

$$\Delta \Sigma = 0 \tag{3.43}$$

$$\Delta\Omega = 0, \pm 1 \tag{3.44}$$

and for the Hund case b specifically

$$\Delta N = 0, \pm 1 \qquad \neq 0(\Sigma - \Sigma), \tag{3.45}$$

where N is the angular momentum of the pair of nuclei in molecules. These rules vary slightly for pure rotation, or pure rovibration and are not discussed here. Degeneracy factors include electronic degeneracy

$$g_e = (2S + 1)\Theta \tag{3.46}$$

where $\Theta = 1$ for $\Lambda = 0$, $\Theta = 2$ for $\Lambda \neq 0$. Vibrational states are not degenerate

$$g_v = 1. \tag{3.47}$$

The rotational degeneracy for Hund case a is

$$g_J = 2J + 1 \tag{3.48}$$

and for Hund case b is

$$g_N = 2N + 1 \tag{3.49}$$

and are all described in Jevons [1932], Herzberg [1950]. These selection rules were needed to be adhered to in the spectral modelling of rotational lines in this work.

Chapter 4

Instruments and developments

4.1 HiTIES

The Spectrographic Imaging Facility (SIF) is a platform of optical instruments (University of Southampton and University College London), which was located in Nordlysstasjonen on Svalbard at geographic position of 78.2025N and 15.829E. The primary instrument used in this work is the High Throughput Imaging Echelle Spectrograph (HiTIES) constructed by Boston University, and is well documented Chakrabarti et al. [2001], McWhirter et al. [2003], Lanchester et al. [2003]. It was designed to measure several selected emissions simultaneously with high spectral and temporal resolution. The field of view is a narrow slit of length 8° centered on the magnetic zenith. Light is collimated, diffracted by a reflection echelon grating, and re-imaged onto the detector. High diffraction orders close to the blaze angle of the grating are used, which gives high spectral resolution and high throughput. The overlapping diffraction orders are separated by a mosaic of interference filters placed at the image plane of the light diffracted from the grating. The mosaic design determines the spectral and spatial coverage of the instrument, the design of which is described in section 4.1.1. The SIF platform also consists of four photometers and an intensified CCD low light level video camera for complementary observations.

The two axes of the image plane where the mosaic filter is placed are wavelength and position along the magnetic meridian field of view. The wavelengths that appear in each diffraction order, and on the recorded image, can be manipulated by changing the angle of the echelle grating. The angle is controlled by a micrometer and is referred

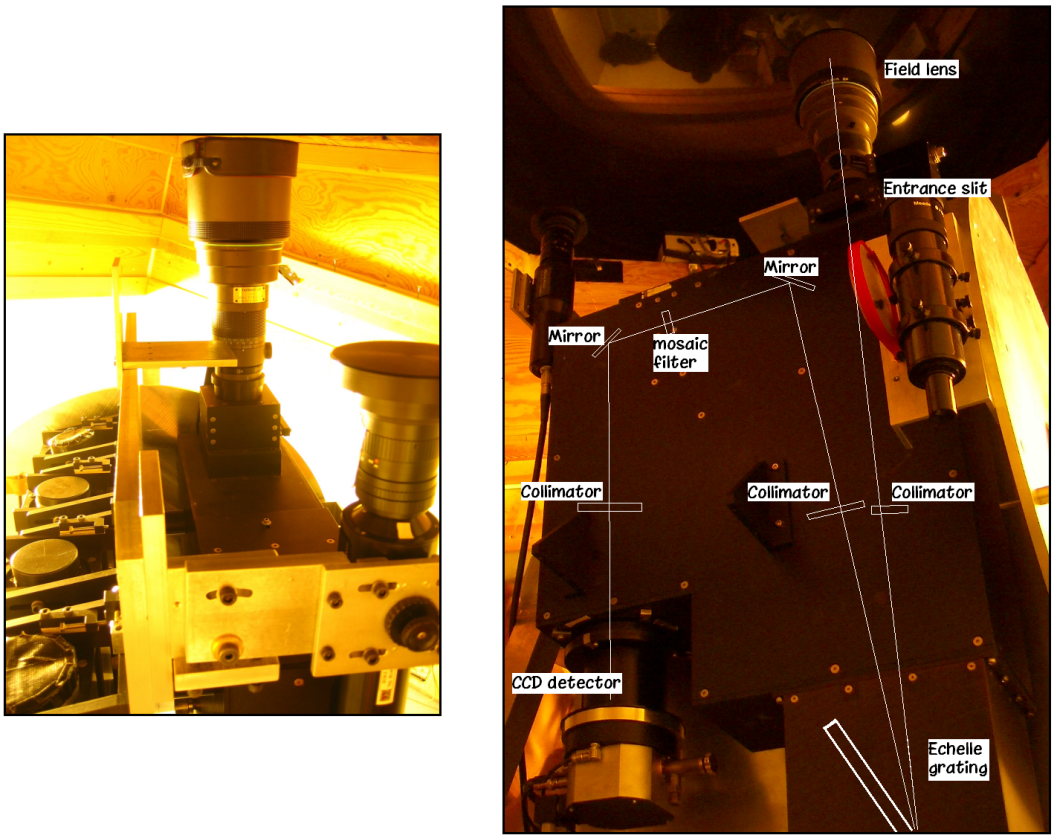

Figure 4.1: *The Spectrographic Imaging Facility (SIF) on the left including four photometers in the left, the High Throughput Imaging Echelle Spectrograph (HiTIES) in the middle and an ICCD video camera in the right. The spectrograph is presented more in detail on the right hand side figure. [Photographs by O. Jokiaho]*

to as the grating setting. The wavelength range in which each order falls increases with wavelength (see Chakrabarti et al. [2001]). Thus the instrument resolution is greatest at shorter wavelengths. There are gaps between the orders towards the red end of the spectrum, but the orders overlap towards the blue. This means that the same wavelength can be seen twice on opposite sides of the image if the two adjacent orders are transmitted. The width of the filter corresponds to a field of view of 8 degrees centred at the magnetic zenith so that only the filter windows in the central strip image the

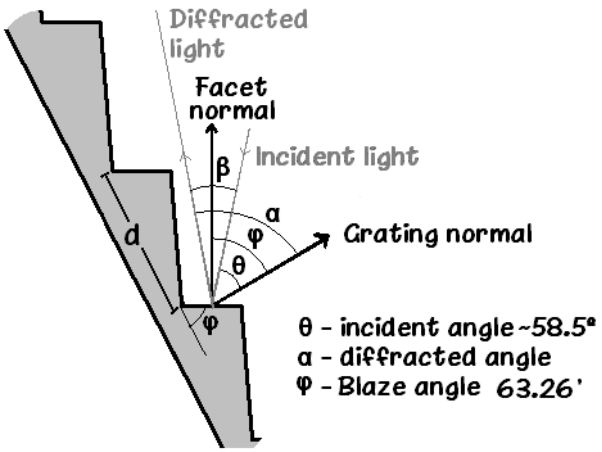

Figure 4.2: *The geometry and the actual orientation of the HiTIES echelle grating close to the blaze angle. [Figure by O. Jokiaho]*

magnetic zenith and strips off the center are off zenith.

The relationship between the line spacing of the grating and the angles of incident and diffracted beams are described by the standard grating equation. Knowing the technical specifications of the HiTIES echelle grating, the wavelength intervals for each diffraction order can be calculated following Eqs. 4.1-4.4.

$$\lambda_1 = d\frac{(sin\theta + sin\alpha_1)}{n} \tag{4.1}$$

$$\lambda_2 = d\frac{(sin\theta + sin\alpha_2)}{n} \tag{4.2}$$

where

$$\alpha_1 = \beta + \theta + \varepsilon \tag{4.3}$$

$$\alpha_2 = \beta + \theta - \varepsilon \tag{4.4}$$

where θ is the incident angle of incoming light to grating normal given by the grating setting between the values of 10 and 20, d is the groove spacing of 98.76 g/mm, α_1 and α_2 are the upper and lower boundaries of the angular spread, β is the angle

between incident and exiting beam and ε is the spread angle of the diffraction with wavelength per order (3.5°). Echelles are often operated very close to the blaze angle (Littrow configuration) so that $\varphi \approx \theta \approx \alpha$ and $\beta \approx 0$ to optimise the intensity of the diffracted light. The geometry of the above is shown in Fig. 4.2.

The HiTIES spectrograph has been used with various different types of detectors. Two of them have been used during the studies carried out here. The first is a microchannel plate Intensified CCD (MIC) photon counting detector and is described in Fordham et al. [1991]. The second detector model is the Andor Ixon DV887DCS-BV (e2v ccd97-00 back illuminated 2-phase 512x512 chip size 16μm pixel size IMO series EMCCD).

4.1.1 Mosaic filter design

In consideration of any optical filter bandpass system one must first identify the science objectives and the target wavelengths which will deliver these objectives. Optimally we try to choose bright lines or bands that are sufficiently free from any contaminating emissions. The objective here is to account for the amount of resonance scattering contributing to auroral emissions during twilight and daytime conditions. The main atmospheric species are nitrogen and oxygen both in their atomic and molecular forms which produce the majority of the observed auroral spectrum. However, molecular nitrogen ions in their ground state are highly susceptible to absorbing solar photons. They are therefore the primary species amongst the atmospheric constituents for resonance scattering during auroral excitation when sunlight is present. The excited states give rise to the 1N (B-X) in the blue end of the visible spectrum and Meinel (A-X) band emissions in the red end of the visible spectrum. The science objectives therefore suggested that both these bands should be measured. It is also beneficial to include emission features that are not affected by the resonance scattering process to use as a reference. These are the neutral N_2 bands 1P ,2P and VK, of which 2P and VK occur in the same wavelength interval as the 1N of the ion species.

As an additional scientific benefit, atomic oxygen lines of 557.7 nm, 630.0 nm, 777.4 nm and 844.6 nm, many of which appear in the day glow spectra, may be fitted into the design. These OI lines characterise low energy electron precipitation [Gustavsson, 2000]. A discussion of the OI 777.4 nm and 844.6 nm emissions is given in Lanchester et al. [2009]. The OI 630.0 nm line has been used in resonance scattering studies before by Henriksen et al. [1984]. He looked at enhancement by energy transfer from O_2^+ in mid-day gap aurora by low energy electron precipitation and correlated this with sunlight in the auroral emission region when N_2^+ ions are excited by resonance scattering. It is also considered desirable to measure hydrogen Hα and Hβ lines in order to indicate the presence of proton precipitation. The region of the Hβ line could be useful in the absence of any protons, when the background N_2 VK spectra from electron precipitation could be measured.

Brightness and contamination issues were considered for each molecular emission feature for N_2^+ 1N v'=0,1,2 progressions, using the measured auroral spectrum and average brightnesses found in Vallance Jones [1974] and Chamberlain [1961]. The 1N bands are favoured over the Meinel bands mainly because of predictable behaviour, simplicity of the spectral shape and less contamination.

Systematic uncertainties also need to be evaluated. It is not practical to make measurements in the ultraviolet range ($<$300-400nm). Significantly reduced transmission occurs because glass lenses and windows will block most light at these wavelengths. Atmospheric scattering is also greater at these wavelengths and depends on observing conditions. Furthermore, the drop off in the spectral response of the camera also set further restrictions. There are in fact many clean and strong N_2 bands below the wavelength of 400 nm but these are not given significant consideration.

Further compromises that need evaluating are natural illumination fall-off from the optical axis on the camera images known as vignetting. The instrument suffers from chromatic aberrations so that the spectrograph can only be focused cleanly into one order of wavelengths, provided that a clean calibration source such as an auroral line or a

spectral lamp is provided. Concentrating the design effort into one colour region would therefore be most sensible. Manufacturing the panels for different thicknesses to allow simultaneous focusing of all channels has also been considered, but would require measuring the difference in the focal point between different colours. The situation can be improved with compensating for the optical path difference with filter panels of different glass substrate thicknesses. The effect of this can be estimated by using the old 3 panel Hγ-Hβ-Hα mosaic filter, tweaking the grating setting with the hydrogen lamp on and finding the focus positions of the lines. The required extra glass thicknesses for each panel can then be calculated, the difference between the different panels being less than 1 mm. In the event due to the mechanical design of the spectrograph this was not possible.

The mosaic consists of a set of interference filters at the image plane, each of them separating the overlapping diffraction orders by transmitting the light in the desired order and blocking the others. The blocking is required at the wavelength appearing on the other end of the filter in the next diffraction order. The greater the physical length of the filter the smaller $\Delta\lambda$ can be used moving spatially from transmission to blocking due to the close proximity of the wavelengths from neighbouring orders. The transmittance of the filter is affected by the substrate material and is typically high in the red part of the wavelength spectrum and becomes poorer towards the blue and ultraviolet wavelengths.

An example of how the various molecular bands and atomic lines position on the image plane for a grating setting of 15.39 is seen in Fig. 4.3. The yellow lines are wavelength boundaries estimated to be sufficient to fully image the spectral features of the labelled bands or lines, if bright enough. The atomic oxygen lines are marked with a single yellow line.

The design process was initiated in August 2006 and the filter was finally delivered in January 2007. Several design plans were drawn up following the spatial positions seen in Fig. 4.3. The emissions drawn here are N_2^+ 1N (0,1), (0,2), (1,1), (1,2), (1,4),

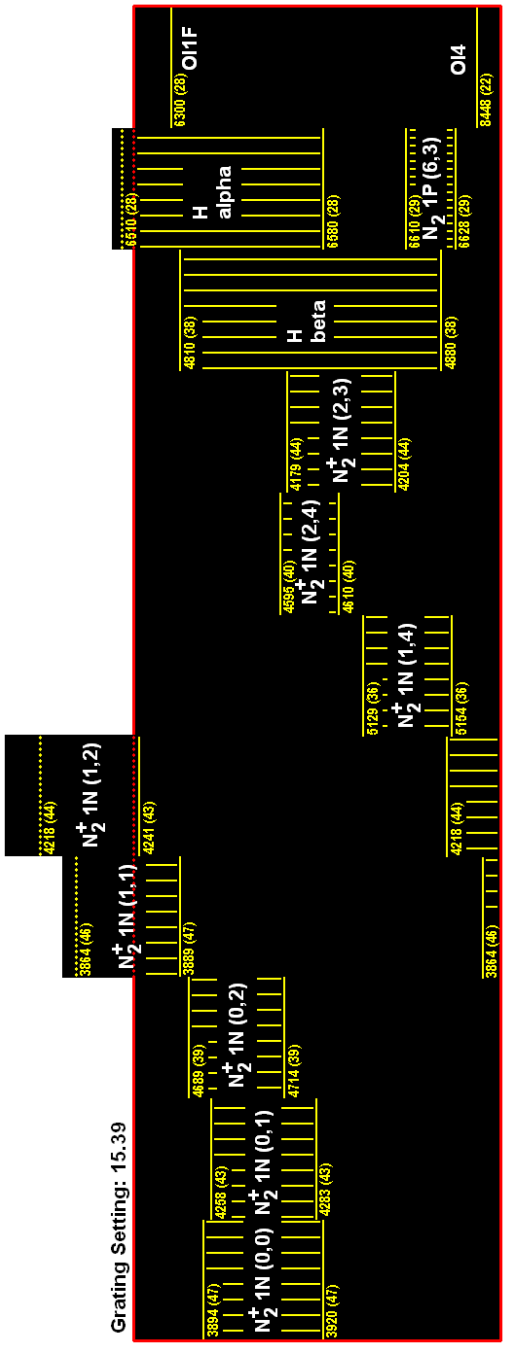

Figure 4.3: *The position of various molecular bands and atomic lines on the image plane when the grating setting at 15.39. The wavelengths are labelled in yellow in Angstroms followed by the diffraction order in brackets. The image has only one dimension and is in the vertical describing the wavelength scale. The horizontal component has only been used to spread out the overlapping spectral features.*

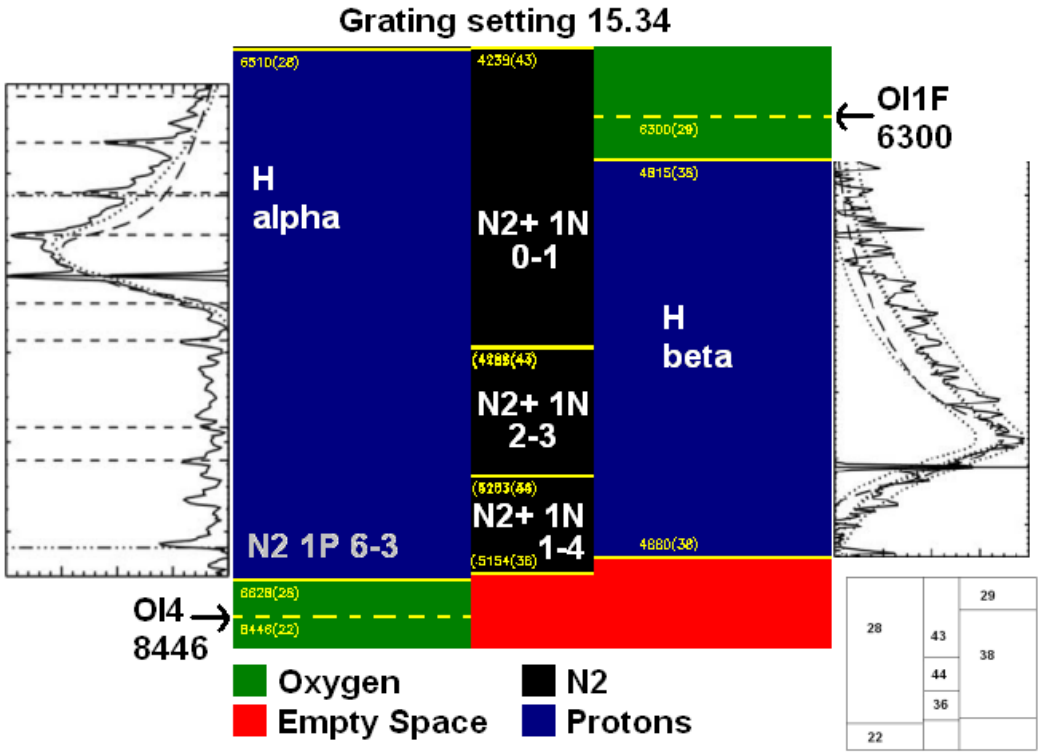

Figure 4.4: *The first mosaic filter design with a grating setting of 15.34. The horizontal component correlates to angle in the field of view and the vertical component to wavelength. A miniature mosaic on the bottom right corner shows the different diffraction orders used. The spectral profiles of Hα and Hβ have been skectched on the panels from Galand et al. [2004].*

(2,4), N_2 1P (6,3), Hα, Hβ, OI 844.8 nm and OI 630.0 nm. Other lines did not fit in this configuration (such as OI 557.7 nm and 777.4 nm). The red lines at the top and the bottom indicate the boundaries of the imaged area. Changing the grating setting the orders move up and down on the image plane. Three different variants of the new mosaic filter were constructed. Two of them are seen in Figs. 4.4 - 4.5.

The most important part of the image plane is the centre which is reserved for primary targets of N_2^+. The centre of the image plane also coincides with the direction of the magnetic zenith. The areas towards the edges of the image plane suffer more

from vignetting and pincushion distortion and should therefore be used for secondary targets. Band heads form towards the longer wavelength part of the emission and it is mainly the band head that would be measured in cases other than the (0,1) band. Therefore, the filter lengths can be compromised from the shorter wavelength side (top part corresponding to shorter wavelength of the image plane) if necessary when the the diffraction orders of the desired bands overlap. This is also the case for the first draft of the mosaic filter seen in Fig. 4.4 based on the setting seen in Fig. 4.3. It manages to capture the (0,1) in the 43rd order, (1,4) in the 36th order and (2,3) in the 44th order of N_2^+ 1N in one central strip of the mosaic. The off-zenith areas of the filter are used for Hα and N_2 1P (6,3) in one filter, OI 845 nm, Hβ and OI 630 nm. This would still leave space available but due to cost it would most likely be used for extending the adjacent filters to save costs and thus become a 7-band mosaic.

It was also considered to split the central filter strip into two narrower filters. This is seen in Fig. 4.5. It is beneficial to include N_2^+ 1N (0,1) and N_2^+ 1N (1,2) in a single filter across the zenith to simplify the design and keep the cost down. Here the grating setting is reduced by 1.04 mm moving the spectral lines down the image. The two central filter strips would now accommodate N_2^+ 1N (0,1) and (1,2) comfortably with N_2^+ 1N (2,3) and (1,1) alongside. The N_2^+ 1N (2,3) can be replaced with the bright N_2^+ 1N (0,0) band so that one continuous filter would then include N_2^+ 1N (0,0) and N_2^+ 1N (1,1), but the disadvantage is that they may both be too far towards the UV to be detected properly. The Hα and Hβ would still fit on the off-zenith panels together with OI 630 nm. Some available filter space would remain as seen in red. The adjacent filters could then be extended to complete the mosaic filter. This would form a 6-band mosaic.

The final solution in Fig. 4.6 was a trade-off between cost and practicality. The new mosaic design for HiTIES is a 5-band filter. The new mosaic is split into three segments, which view different parts of the 8 degree meridian slit. The middle zenith section is used for N_2^+ 1N (0,1), (1,2) and (2,3) bands, all affected by resonant scattering. The two remaining areas of the mosaic are filled with Hβ and Hα bands, still leaving enough

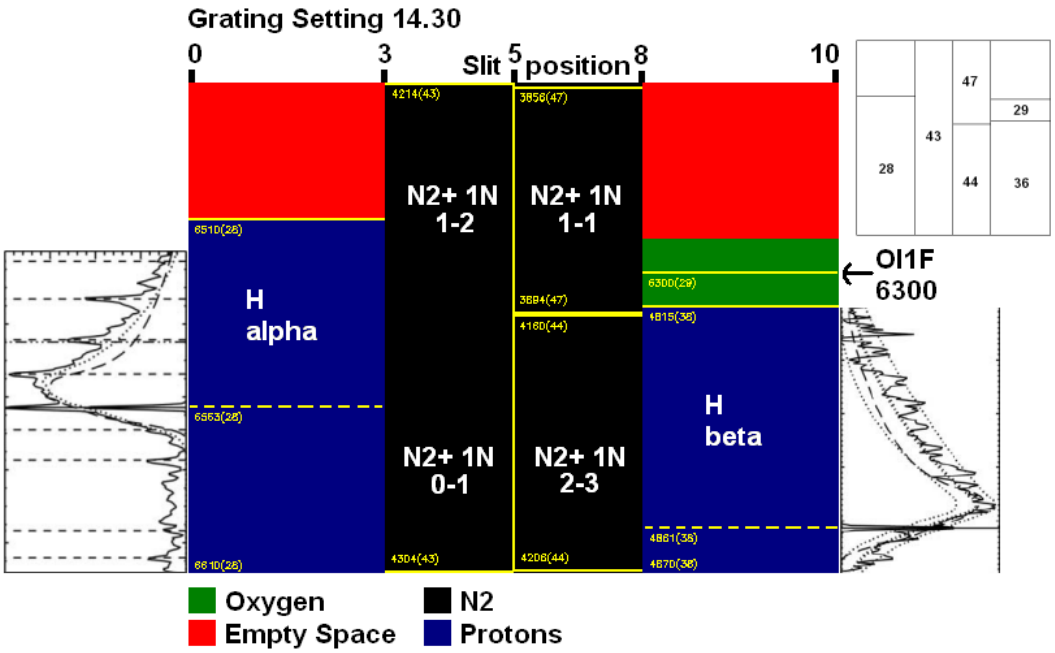

Figure 4.5: *The second mosaic filter design with a grating setting of 14.30. The horizontal component correlates to angle in the field of view and the vertical component to wavelength. A miniature mosaic on the top right corner shows the different diffraction orders used. The spectral profiles of Hα and Hβ have been sketched on the panels from Galand et al. [2004].*

room for one molecular nitrogen band unaffected by resonant scattering, that is N_2 2P (0,3), which will be used as a reference for the 1N bands during sunlit conditions. The hydrogen panels will suffer slightly from vignetting but this has been compensated with larger filter widths.

The filter edges are painted black to reduce the effect of any stray light and panels glued together with a very narrow joint width (<0.5mm). A block factor of 5 in optical density was required and a blocking range of 200 nm - 1100 nm. The filters are also required to have imaging quality, which allows greater control over the spherical and chromatic aberrations than normal interference filters. Hard anti-reflectance coatings are requested for safe handling. Filters are specified in terms or their centre wavelength (CWL) and full width at half maximum (FWHM). In this case they were specified more

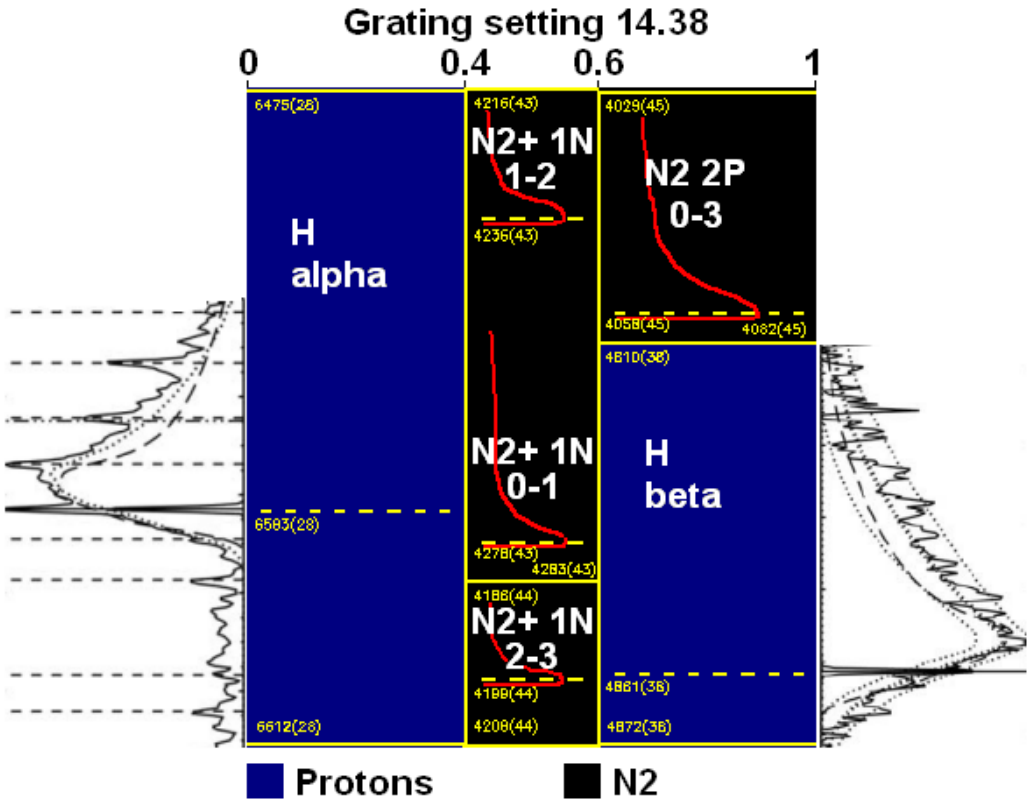

Figure 4.6: *The third mosaic filter design with a grating setting of 14.38. The horizontal component correlates to angle in the field of view and the vertical component to wavelength. The spectral profiles of Hα and Hβ have been sketched on the panels from Galand et al. [2004].*

for the bandpass, minimum transmittance and next order blocking. The quotation request that was sent is seen in Table 4.1.

The N_2 and N_2^+ bands occur in orders 43 - 45 in panels labelled N1, N2 and N3. This is where HiTIES would be focused. The H panels are used to record emissions from orders 28 and 38 and consequently they would not be in focus. A high transmittance of at least 70% is required. The bandpass is stated as modelled in Fig. 4.3, unless spatially limited by neighbouring filters or the edge of the filter. Next order blocking is required at optical density of 3 at a point when the shorter wavelength of the $n-1$ order emerges at the image plane and through the filter and similarly when the longer wavelength of

Diff. order	Panel	T	bandpass	Next order blocking at OD3	$\Delta\lambda$
45	N1	>70%	402.9 nm-406.2 nm	λ <399.5 nm	3.4 nm
				λ >412.0 nm	5.8 nm
44	N2	>70%	418.6 nm-420.8 nm	λ <411.5 nm	7.1 nm
				λ >428.0 nm	7.2 nm
43	N3	>70%	421.6 nm-428.3 nm	λ <418.8 nm	2.8 nm
				λ >431.6 nm	3.3 nm
38	H1	>70%	481.0 nm-487.2 nm	λ <475.0 nm	6.0 nm
				λ >493.5 nm	6.3 nm
28	H2	>70%	647.5 nm-661.2 nm	λ <639.0 nm	8.0 nm
				λ >493.5 nm	9.8 nm

Table 4.1: *The quotation request sent to Glen Spectra in tabular form.*

the $n+1$ order emerges at the image plane and through the filter, where n is the imaged order. The maximum allowed width $\Delta\lambda$ in wavelength required between passband and blocking is seen in the final column.

A schematic drawing of the mosaic filter is seen in Fig. 4.7 with dimension given in millimetres and the bandpass wavelengths in Ångström. The manufacturer provided theoretical curves for review and it was found that the next order blocking (N1 0.3%, N2 0.03%, N3 0.1%, H1 0.03% and H2 0.02%) was greater than required while the transmission was too low at the edges of the bandpass filters (N1 23.0%, N2 18.0%, N3 3.2%, H1 19.4% and H2 15.1%). It was therefore requested that the next order blocking to be reduced up to 1%.

Our initial required peak transmittance is 70% and the bandpass should be within 75% of the peak. The peak transmission for the N1, N2 and N3 filters will not achieve the desired peak transmission due to the material used in constructing the filters is more absorbant in this wavelength region.

The final product was delivered in the mid January 2007. The transmittance characteristics of the final product is seen in Fig. 4.8 accompanied by a photograph of the filter.

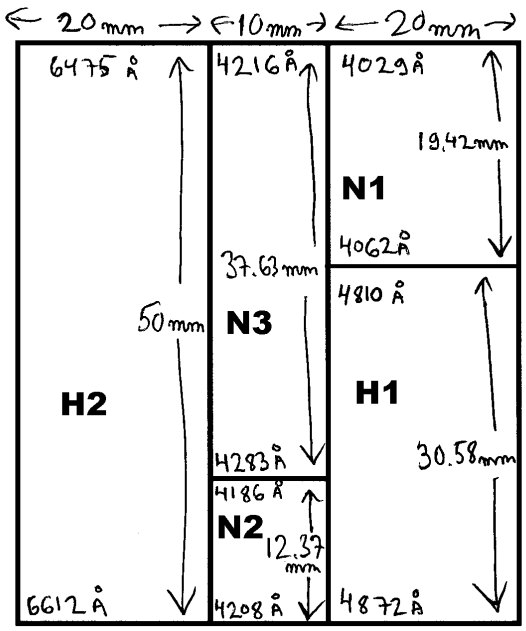

Figure 4.7: *The quotation request sent to Glen Spectra in schematic form.*

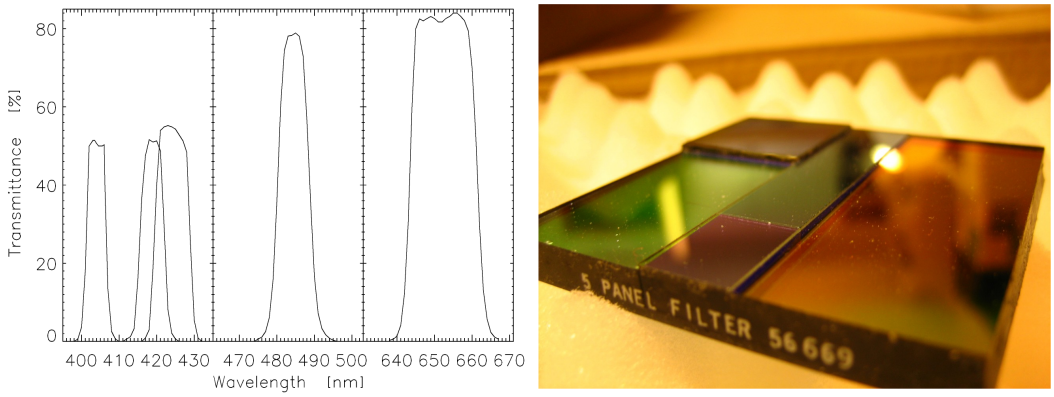

Figure 4.8: *The transmittance characteristics of the finished five band mosaic filter for optical selection (left) and a photograph of the final product. The filter measures 50mm x 50mm in size. [Photograph by O. Jokiaho]*

4.2 ASK

The ASK instrument is made up of three co aligned cameras with image rates of up to 32 frames per second, and two photometers with selected narrow band filters pointed toward magnetic zenith. The instrument is described in Dahlgren et al. [2008] and Ashrafi et al. [2007]. The imagers are each equipped with an Andor iXon EMCCD detector with 512×512 pixel chip attached to a Kowa 75mm F/1 lens, which gives a field of view of $6° \times 6°$. It can be fitted onto a removable telescope to make a 150 mm, f/1.0 lens. The resulting field of view is $3° \times 3°$ which is equivalent to 5×5 km at 100 km height. During the winter of 2006/2007 the ASK instrument was located at the EISCAT site in Ramfjordmoen, Norway.

The studies conducted in this thesis form part of a comparison between ASK measurements and modelling described in Lanchester et al. [2009]. The particular contribution made by the author is contained in Ashrafi et al. [2009], in which the crossection for the N_2 1P bands measured by ASK were determined. The cameras are named ASK1, ASK2 and ASK3. The ASK1 filter had a central wavelength of 673.0 nm, with width containing the vibrational band emissions from transitions (4,1) and (5,2) of the N_2 1P. The ASK2 filter is designed to measure emission from the oxygen ion at 732.0 nm, caused by the $O^+(^2P-^2D)$ transition. The ASK3 filter measured 777.4 nm from atomic oxygen. Synthetic line spectra are evaluated against the transmittance profiles of the ASK camera filters to quantify the total transmittance factor of the desired spectral emissions. This is used in the ion chemistry model as a vital parameter to form an analytical basis for the measured intensities.

4.2.1 Filter transmission curves with synthetic spectra

The method of modelling synthetic spectra within the interference filter transmission curves is valuable in order to estimate the factor for total band throughput. These factors are needed when comparing measured emission rates with those obtained with the ionchemistry model. Interference filters are used in three different intrumenta-

tion modes. Spectral lines are recorded at high resolution with the HiTIES spectrograph, image recording for cameras such as the ASK instrument and bulk photon counting in photometers. Since for a spectrograph, wavelength is one of the degrees of freedom, the determination of synthetic spectra is more significant in the latter two in order to assess more accurately what the instrument is recording.

In order to determine synthetic spectra from the model described in Chapter 3, the correct rotational constants are needed for the two vibrational levels between which the de-excitation is taking place, as well as the correct band origin(s). The correct number of branches are needed to be calculated from the net electron orbital angular momentum and the net electron spin together with various intensity distribution factors such as Hönl-London and the nuclear spin.

The shape of the spectra can be visualised more easily if the theoretical lines from the synthetic spectrum are convolved with an instrument function. The convolved shape changes dramatically with narrowing of the instrument function and when approaching infinite resolution the lines are seen exactly as the individual lines of the synthetic spectra. Apart from ease of visualisation in imaging filters, the convolution process of synthetic spectra is fundamental in studying spectrographic images where the instrument function is real.

The relative brightness of the spectral lines were integrated with respect to wavelength with and without the interpolated filter transmission curve. The ratio of these two gives the transmitted fraction of the total intensity by the filter. This procedure was repeated for different rotational temperatures. The various interference filters in use by the Space Environment Physics group are assessed here.

4.2.1.1 N_2 1P $B^3\Pi_g$-$A^3\Sigma_u^+$ (4,1) and (5,2) at 665-685 nm

The ASK imagers use 3″ interference filters. One filter is centered at 673.0 nm with a FWHM of 15 nm. This filter typically measures high energy electron precipitation and excitation of the neutral molecular species with peak altitudes of 100-120 km

[Lanchester et al., 2009, Ashrafi et al., 2009].

The $B^3\Pi_g$-$A^3\Sigma_u^+$ transition exhibits an intensity alternation for rotational lines of 2:1 due to nuclear spin. The involved states have net electon spin of 1 with a resulting multiplicity of 3 and the occurring energy levels are split into three. The Π state is also split due to Λ-type doubling. During the transition the electron orbital angular momentum decreases by one. Apart from the standard Hönl-London factors and nuclear spin effects, all 27 branches of the 1P bands are treated as equal intensities. This may not be strictly correct as deviation from this in the form of three weaker branches has been reported, but only qualitatively. A characteristic of the first positive band is the strong Q-branch.

Wave origins for (4,1) are 14726 cm^{-1}, 14766 cm^{-1} and 14801 cm^{-1} and for (5,2) 14910 cm^{-1}, 14950 cm^{-1} and 14985 cm^{-1}. An instrument function of 0.5 nm for the half width at half maximum (HWHM) was used for the convolution. The N_2 first positive band was studied in detail by Naude [1931] who reported Δ_{12}=40 cm^{-1}, Δ_{23}=35 cm^{-1}, Δ_{total}=75 cm^{-1} and A=37.5cm^{-1} and later in Naude [1932] reports molecular constants of Δ_{12}=42 cm^{-1}, Δ_{23}=37 cm^{-1}, Δ_{total}=79 cm^{-1} and A=39.5cm^{-1}.

The relative intensities between the two (4,1) and (5,2) bands are within 4% of each other [Vallance Jones, 1974]. The interference filter measures more of the (4,1) band intensity than the (5,2) band intensity. Even at low rotational temperatures of 200 K the transmittance is about 84% and 64% respectively as can be seen in Fig. 4.9. As the thermal distribution of rotational populations develop towards higher temperatures the brightness distribution shifts towards the blue. At around 1000 K the transmittance of the (4,1) and (5,2) bands is 80% and 50% respectively. Considering the relative populations of atmospheric species with altitude the lower temperature limit is a more realistic approximation for the neutral molecules. The total transmittance of the two bands as a function of rotational temperature is shown in Fig. 4.10. A throughput factor between 70-75% is appropriate for most conditions.

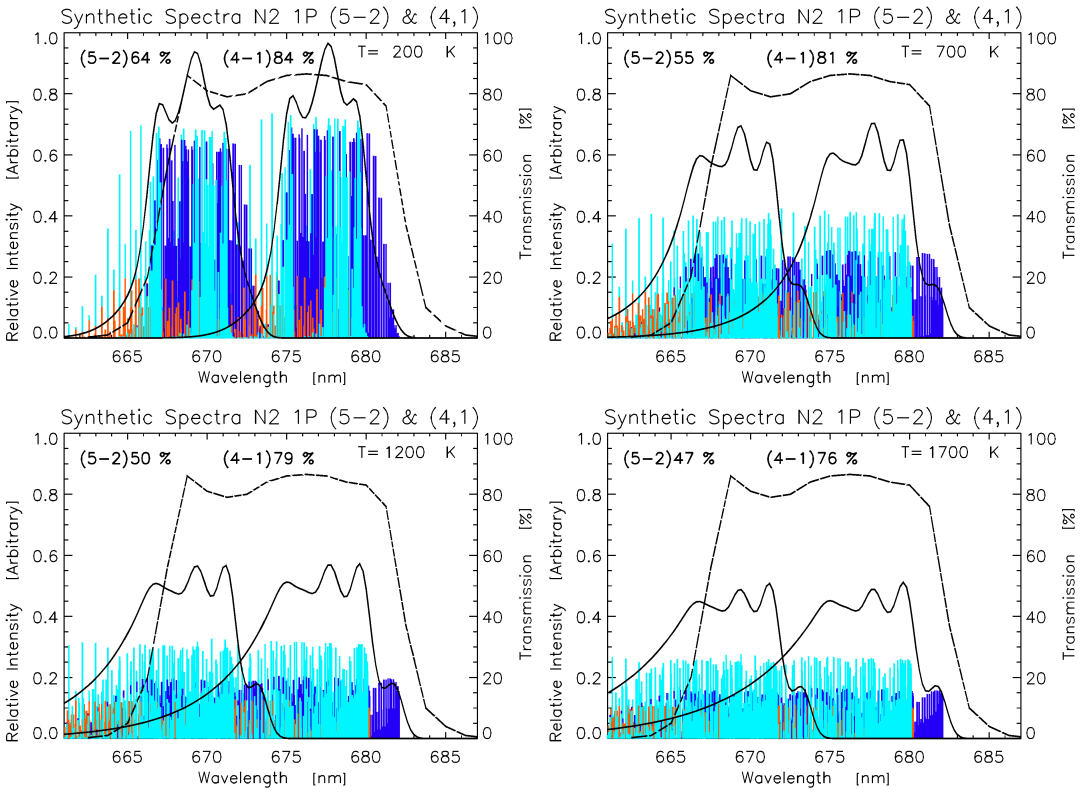

Figure 4.9: *N_2 1P $B^3\Pi_g$-$A^3\Sigma_u^+$ (4,1) and (5,2) rotational spectra profiles for four different temperatures with filter transmittance curve (dashed line) and the convolved shape (solid line).*

4.2.1.2 N_2 1P $B^3\Pi_g$-$A^3\Sigma_u^+$ (6,4) and (5,3) at 720-740 nm

Another 3″ ASK camera filter measures the OII ^2D-^2P (6,4) centered at 731.9 nm with a FWHM of 1.0 nm. It is used to measure the high altitude and low energy component in aurora. This atomic line lies between two N_2 1P (6,4) and (5,3) bands, whose relative intensities are approximately 1:3. The (5,3) band is also 30% brighter than the (4,1) and (5,2) bands described in the previous subsection. The molecular properities are the same as in the bands in the previous subsection, however, the band origins here are: 13743 cm^{-1}, 13783 cm^{-1} and 13818 cm^{-1} for (6,4) and 13533 cm^{-1}, 13573 cm^{-1} and 13608 cm^{-1} for (5,3). The instrument function for the convolved profile is 0.5 nm at HWHM and for low excitation temperatures of the N_2 1P the filter excludes these

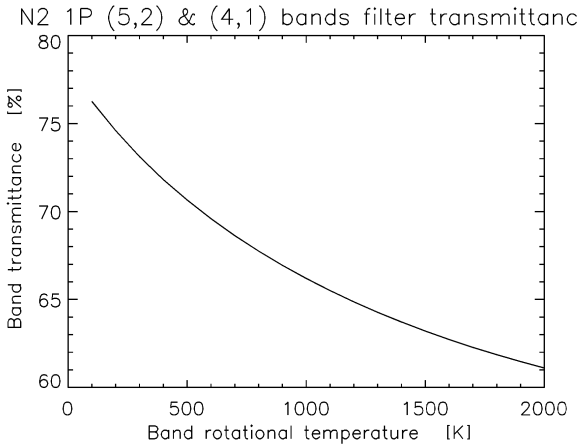

Figure 4.10: *N_2 1P $B^3\Pi_g$-$A^3\Sigma_u^+$ (4,1) and (5,2) filter transmittance as a function of T_r.*

emissions well, but with increasing temperature the (5,3) band starts to overlap with the OII ^2D-^2P line. This is seen in the convolved profile in figure 4.11.

4.2.1.3 N_2^+ 1N $B^2\Sigma_u^+$-$X^2\Sigma_g^+$ (0,1) at 427.8 nm

Another 3″ ASK camera filter measures the auroral blue line of the N_2^+ 1N band centered at 426.7 nm with a FWHM of 4.0 nm. N_2^+ measures the high energy component in conditions of non sunlit aurora. The 1N transition is between $B^2\Sigma_u^+$ and $X^2\Sigma_g^+$, which indicates the molecular electrons possess zero net orbital angular momentum (Λ=0 and $\Delta\Lambda$=0) and therefore no Q-branch appears. The net electron spin is $\frac{1}{2}$ due to an unpaired electron, which makes this a doublet transition, but is approximated to a very good precision by a singlet synthetic model. The usual N_2 intensity of 2:1 between odd and even rotational lines applies from nuclear spin.

An instrument function of 0.04 nm at HWHM was used. The filter transmits 50% of the (0,1) band at low rotational temperatures of 200 K, reducing to 39% at 1500 K as indicated in figures 4.12 and 4.13.

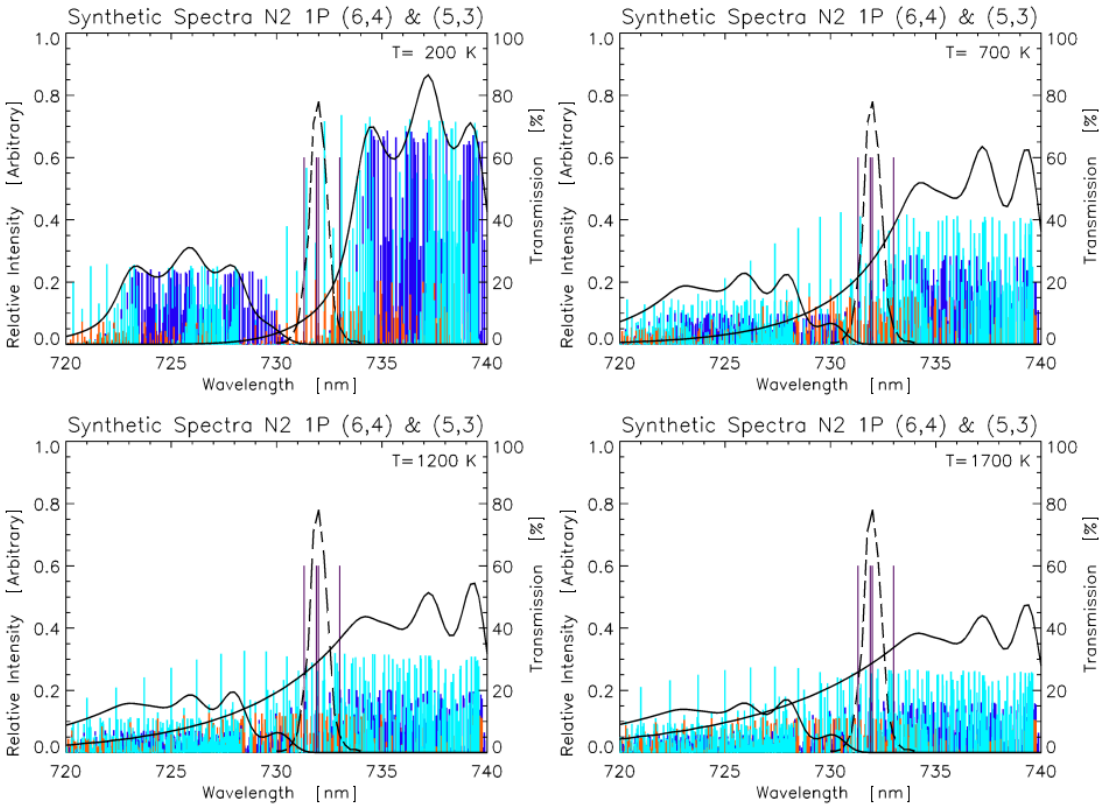

Figure 4.11: *OII ^2D-^2P (6,4) with profiles of N_2 1P $B^3\Pi_g$-$A^3\Sigma_u^+$ (6,4) and (5,3) as potential contaminants. The filter transmittance curve is seen as a dashed line and the convolved shape of the molecular bands as solid line*

4.2.1.4 N_2^+ 1N $B^2\Sigma_u^+$-$X^2\Sigma_g^+$ (1,4) at 514.9 nm

The (1,4) band represents the same $B^2\Sigma_u^+$ and $X^2\Sigma_g^+$ transition as the (0,1) in the previous subsection. This 2" interference filter with a FWHM of 2 nm centered at 514.0 nm is used on a photometer. The instrument function used here for convolving a singlet profile is 0.04 nm at HWHM. This filter curve is narrower than the (0,1) and hence throughputs less in higher rotational temperatures, as seen in figure 4.14. It has a higher transmittance at the peak, which is not located at the band head. Thus, as compared to Fig. 4.12, the band transmittance is higher at low temperatures as compared

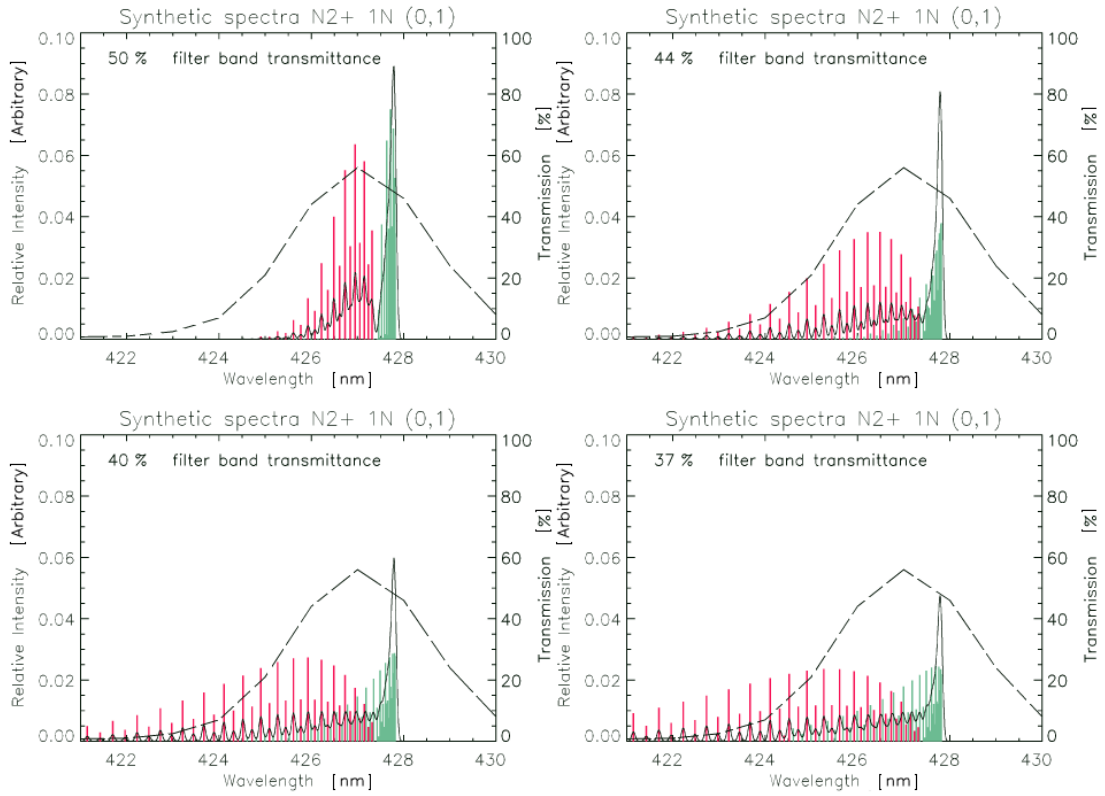

Figure 4.12: *N_2^+ 1N $B^2\Sigma_u^+$-$X^2\Sigma_g^+$ (0,1) rotational spectra profiles for four different temperatures with filter transmittance curve (dashed line) and the convolved shape (solid line).*

to the (0,1) filter. Figure 4.15 shows the band transmittance as a function of rotational temperature starting from 60% at 200 K, 40% at 700 K and 30% at 1600 K.

4.2.1.5 O_2^+ 1N $b^4\Sigma_g^-$-$a^4\Pi_u$ (1,0) at 563.2 nm

A fourth 3″ ASK camera filter is centered at 562.0 nm with a FWHM of 2.6 nm. It measures the $b^4\Sigma_g^-$-$a^4\Pi_u$ transtion of the oxygen molecular ion. The molecule has net electron spin of $1\frac{1}{2}$ and during the transition gains orbital angular momentum by one. Hence it has an electron spin multiplicity of 4 and four distinct energy levels exist. The Π state also is split due to Λ-type doubling. In comparison to $B^3\Pi_g$-$A^3\Sigma_u^+$ of N_2 1P the structure looks similar apart from a difference in missing lines at the beginning

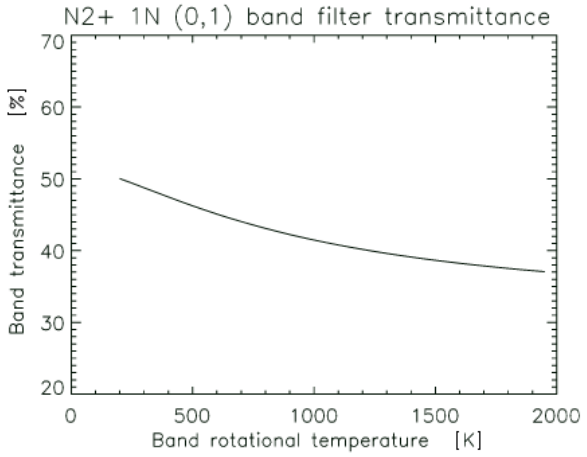

Figure 4.13: *N_2^+ 1N $B^2\Sigma_u^+$-$X^2\Sigma_g^+$ (0,1) filter transmittance as a function of T_r.*

of the branches, a new set of Hönl-London factors and also that O_2 1N is a quintet band with a total of 48 branches. There is no intensity alternation as every other rotational line is missing as is expected according to the configuration of the nuclear spin. The four band origins are separated by nearly 50 cm^{-1} at 17755 cm^{-1}, 17797 cm^{-1}, 17852 cm^{-1} and 17900 cm^{-1}. We assume constant intensity ratios set by the Hönl-London factors. The foundation for the rotational analysis of O_2^+ 1N was provided by Nevin [1938, 1940]. The main contamination comes from the oxygen 557.7 nm line, which overlaps the oxygen 1N (1,0) band on the short wavelength side. The N_2 1P bands (5,0) and (6,0) also overlap the O_2^+ 1N (1,0) band, but their average intensities are nearly two orders of magnitude less significant [Vallance Jones, 1974].

The synthetic convolved profile with an instrument function of 0.5 nm and the filter transmission curve can be seen in figure 4.16 as a function of rotational temperature. This filter captures up to 22% of the total O_2^+ 1N (1,0) band intensity at T_r=200 K reducing gradually to around 15% for temperatures of 1000 K.

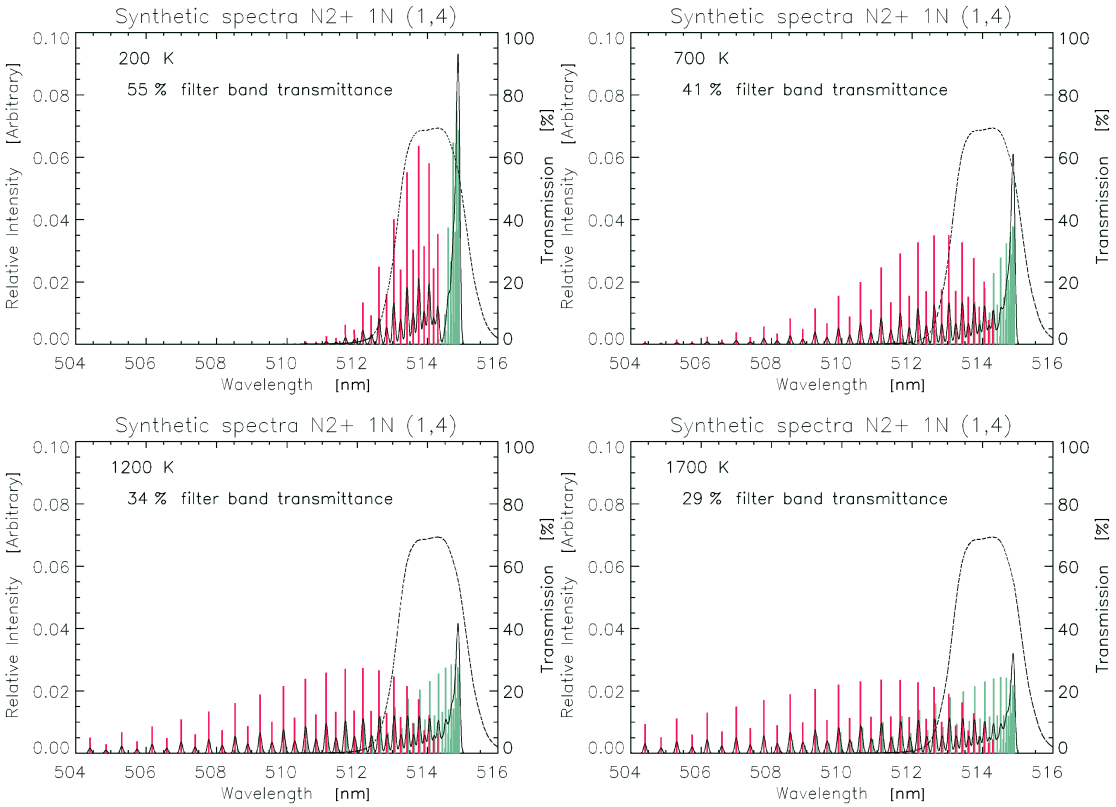

Figure 4.14: *N_2^+ 1N $B^2\Sigma_u^+$-$X^2\Sigma_g^+$ (1,4) rotational spectra profiles for four different temperatures with filter transmittance curve (dashed line) and the convolved shape (solid line).*

4.3 Svalbard EISCAT radar

The EISCAT radar utilises the incoherent Thompson scattering of high power radio waves by ionospheric electrons, which allows a direct measurement of the densities and temperatures of electrons and ions as a function of height in the ionosphere. The European Incoherent Scatter (EISCAT) Svalbard Radar (ESR) is situated 7 km from Nordlysstasjonen on Svalbard. The radar runs are characterised by a choice of different radar programmes that accommodate specific pulse lengths, sampling rates, height resolution, range and time resolution, a full description of which is outside the scope of this thesis.

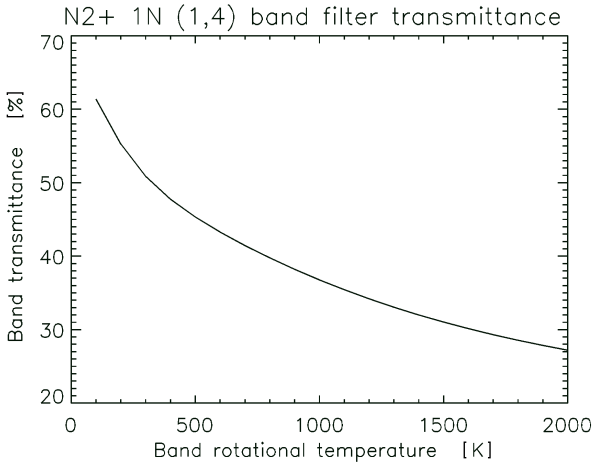

Figure 4.15: *N_2^+ 1N $B^2\Sigma_u^+$-$X^2\Sigma_g^+$ (1,4) filter transmittance as a function of T_r.*

The data from the radar used in the research described here was taken with an experiment called TAU0. This is an alternating code experiment with two 960 μs pulses (15×64 s). The range separation of the samples is 2.4 km, but adjacent samples are not completely independent. The range covered is from below 100 km in the E region to the topside at 1000 km. The integration time in TAU0 is 12.8 s. However, the basic quantum is the time taken to transmit and receive the 64 repetitions of the modulation scheme needed to decode the alternating code, which is 640 ms. The integration time can be reduced to any multiple of this figure, with the aim of using the highest time resolution possible, depending on signal to noise ratio. An integration time of 6.4 s was used in the experiment. In order to increase the signal to noise pre-analysis integration of 32s was used in the present work, which corresponds to the resolution of the spectrograph used.

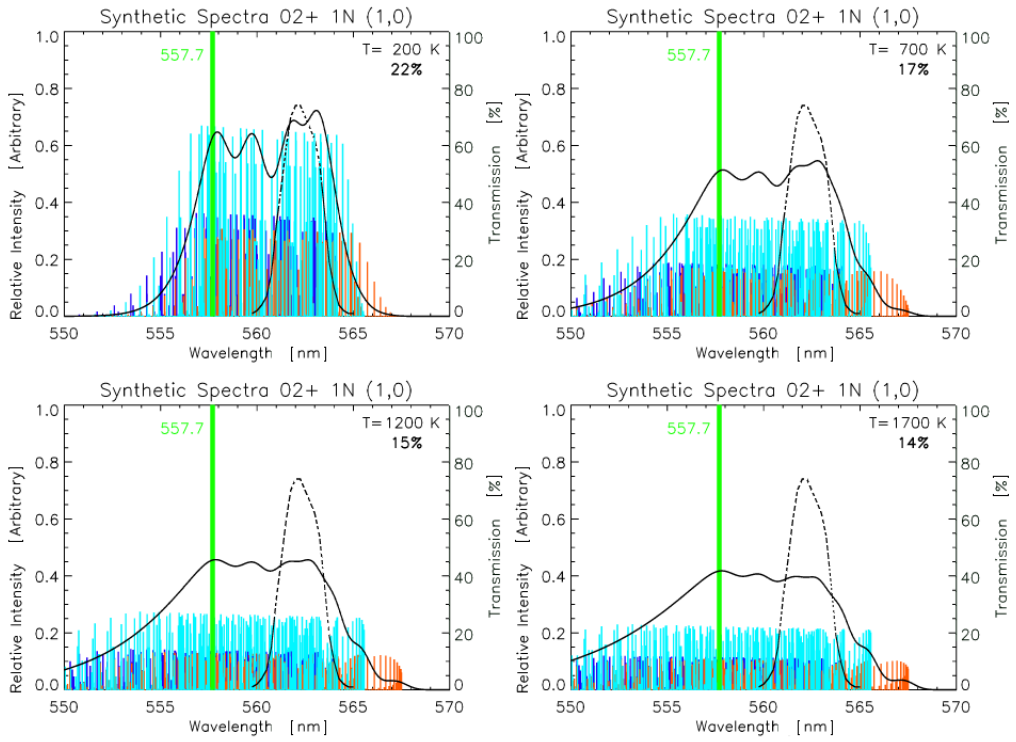

Figure 4.16: *O_2^+ 1N $b^4\Sigma_g^-$-$a^4\Pi_u$ rotational spectra profiles for four different temperatures with filter transmittance curve (dashed line) and the convolved shape (solid line).*

Published as: O. Jokiaho, B. S. Lanchester, N. Ivchenko, G. J. Daniell, L. C. H. Miller and D. Lummerzheim – *"Rotational temperature of N_2^+ (0,2) ions from spectrographic measurements used to infer the energy of precipitation in different auroral forms and compared with radar measurements,"* Annales Geophys., 26, 853-866, 2008.

Chapter 5

Rotational temperature of N_2^+ (0,2) ions from spectrographic measurements

5.1 Introduction

It has been recognised for more than half a century that spectral measurements of the rotational molecular bands of emitting species in the upper atmosphere can be used to deduce the temperature of the neutral atmosphere. In order to do this it is assumed that the emitting species are in thermal equilibrium with their local environment. If the height profile of the atmospheric temperature is known or modelled, this process can be reversed to provide the height of the emitting species and hence the energy of the precipitating electrons.

In the study of aurora, observing the temporal and spatial changes in the energy distribution of the incoming particles is key to understanding the source regions of these energetic particles. The advent of charge coupled device (CCD) detectors in the field of spectroscopy has provided the means to increase sensitivity as well as resolution in wavelength and time. Imaging spectrographs are currently the optimal instruments for high spectral resolution measurements of auroral signatures. Such measurements allow us to build on techniques that were well understood in the 1950s, and obtain more accurate estimates of the physical processes.

Koehler et al. [1981] provide a comprehensive description of the first measurements of rotational temperatures of emitting N_2^+ ions, and the subsequent application of these results to auroral physics. These early publications include Vegard [1932], Harang [1951], Shepherd and Hunten [1955], Hunten et al. [1963], Brandy [1964], Hilliard and Shepherd [1966], Miller and Shepherd [1968], Zwick and Shepherd [1973], Shepherd and Eather [1976]. Once the atmospheric temperature profile was established, following satellite measurements and modelling studies [Hedin, 1991], it became clear that spectroscopic information on rotational temperatures was valuable for ground-based studies of the energy of precipitation.

Several workers (e.g. Romick et al. [1978], Vallance Jones et al. [1987], Koehler et al. [1981], Holma et al. [2000, 2003]) used photometer channels with carefully selected narrow band interference filters, to measure the P and R branches of the N_2^+ 1N (0,1) band. The ratio of the intensities of these channels gives an estimate of the variation in the shape of the rotational band, and thus of the neutral temperature. A more accurate measure of the shape of the rotational band is obtained with scanning spectrometers or imaging spectrographs. By fitting such measurements to synthetic spectra, the temperature of the emitting ions can be obtained, and hence the height of the emission region can be estimated from the neutral temperature profile, with similar assumptions mentioned above.

Henriksen et al. [1987] addressed the question of whether variations in neutral temperature could be caused by the changing height of the emission region, or by local heating. They used a 1 m Ebert-Fastie spectrometer to measure the N_2^+ 1N (0,3) band and four O_2^+ 1N bands. Ratios of different emissions have also been used for many years to estimate the energy of precipitation by association with the height of the emitting regions (e.g. Rees and Luckey [1974], Kaila [1989]). The intensity ratio of N_2^+ 1N (0,3) to O_2^+ 1N (1,0) is dependent on height; Henriksen et al. [1987] used this ratio to derive the height of the aurora. The result was compared with that obtained by fitting the shape of the rotational bands to obtain the neutral temperature. The results from both

methods were similar, inferring that changes in temperature were caused by changes in the height of the aurora and not by heating.

Temporal variations in the incident electron spectrum can be inferred from incoherent radar measurements in the magnetic zenith. Vallance Jones et al. [1987] compared such estimates of the average energy with those derived from optical emissions at Sondre Stromfjord, Greenland. Two optical methods were used: the intensity ratio I(6300)/I(4278) and also rotational temperatures derived from two photometer channels in the P and R branches of the N_2^+ 1N (0,1) band. All three estimates gave similar results for the average primary electron energy. These authors used the results to validate a theoretical model of ion chemistry and optical emissions in the aurora. They calculated electron density height profiles from ionisation rate profiles, which were estimated from optical emissions (primary energies from N_2^+ rotational temperatures and total energy flux from I(4278)), and found a good agreement with the radar measurements.

The spectral signatures of the aurora contain information about the energy distribution of precipitating particles, and the state of the high altitude atmosphere. Theoretical models and synthetic spectra can be used to deduce much of this information. Higher spectral resolution gives more accurate results, allowing the clear separation of the rotational lines in the P and R branches, as long as there is sufficient signal in the wavelength region. The present work combines such high spectral resolution (0.08 nm) measurements from an imaging spectrograph viewing the magnetic zenith with narrow angle camera images, incoherent scatter radar measurements and an ion chemistry model of the auroral ionosphere. Analysis of spectral measurements of the N_2^+ 1N (0,2) band (470.9 nm) has been performed with particular attention to the errors when fitting the measured spectra to synthetic spectra. This molecular band provides significant line intensities free of any contamination and overlapping from neighbouring bands. The present work highlights the importance of estimating the correct background to be subtracted from the emissions, as well as the effect that small deviations in wavelength

calibration can have on the results.

5.2 Experimental Details

For the observations described here, HiTIES was equipped with a three panel mosaic, with spectral intervals for H_β, N_2^+ 1N bands 463.5–466.0 nm and 469.0–471.5 nm, and with all panels covering the 8° slit length. The detector used during these observations was the Microchannel Intensified CCD [Fordham et al., 1991]. It is a photon counting detector, with very low dark count rate and no read-out noise. The spectral resolution of the spectrograph is determined by the slit width, which requires a compromise with the amount of light that enters the instrument. In these observations the resolution is 0.08 nm for the FWHM instrument function. Typical integration times are 10–60 s. Measurements can be integrated over different sections of the meridian slit as required. In the present measurements, time resolution of 30 s was used with readout time of 2 s, and integration over the slit was performed in steps of 1°.

The platform housed two photometer channels at the wavelengths of the H_β line near 486.1 nm, and of the N_2^+ 1N (1,3) band at 465.2 nm. A narrow angle camera measured the emissions in a field of view of 12° by 16° in the magnetic zenith. A short wavelength cut-off filter (645 nm) was used to eliminate the forbidden emissions from atomic oxygen, and to allow the prompt emission of N_2^+ Meinel and N_2 1P bands to be imaged.

5.3 Theory

The following section includes some repetition from chapter 3, but it is included here for the convenience of the reader in order to provide continuity and completeness.

Intensity calculations of the N_2^+ 1N band spectra, which is a transition between two electronic states of N_2^+, are well documented Herzberg [1950], Degen [1977]. The energy of the molecule has terms corresponding to the vibrational and rotational degrees of freedom in addition to the energy of the electron states and can be acquired with harmonic oscillator and rigid rotor models in the following equation:

$$\overline{\epsilon}_{v,j} = \left(v + \frac{1}{2}\right)\overline{\omega} + \overline{B}_v J(J+1) \tag{5.1}$$

where

$$\overline{\omega} = \left(\frac{1}{2c\pi}\right)\sqrt{\frac{\kappa}{\mu}}, \quad \overline{B}_v = \frac{h}{8I_n c\pi^2} = \overline{B}_e - a\left(v + \frac{1}{2}\right) \tag{5.2}$$

v is the vibrational quantum number, $\overline{\omega}$ is the classical vibrational frequency of the bond i.e. band origin, κ is the bond strength, μ is the reduced mass, h is Planck's constant, c velocity of light, I is the moment of inertia of the system about its axis of rotation, J is the rotational quantum number, $\overline{B}_v$ is a rotational constant, $\overline{B}_e$ is the rotational term corresponding to the equilibrium bond length and a is the vibration-rotation interaction constant. Notation is in wavenumber. The sets of spectral lines forming within a vibrational band are known as the P ($\Delta J = -1$) and R ($\Delta J = +1$) branches in the Σ - Σ state transitions. No Q-branch forms because the molecule has no unpaired electrons. For $\overline{B}'_v > \overline{B}''_v$ the band head forms in the P-branch, as in the transition in our study, and in the opposite case in the R-branch. Band head by definition is the wavelength where the Fortrat parabola has a turning point. By standard notation, single prime corresponds to a vibrational level in a higher energy electronic state than double prime. Using the appropriate selection rules the positions of the vibration-rotation lines are predicted to lie at wavenumbers given by

$$\overline{\nu}_P = \overline{\omega} - (\overline{B}'_v + \overline{B}''_v)J'' + (\overline{B}'_v - \overline{B}''_v)J''^2 \tag{5.3}$$

$$\overline{\nu}_R = \overline{\omega} + 2\overline{B}'_v + (3\overline{B}'_v - \overline{B}''_v)J'' + (\overline{B}'_v - \overline{B}''_v)J''^2 \tag{5.4}$$

The rotational quantum number here corresponds to the vibrational state in the lower electronic state. The relation between wave number in air and vacuum has been applied from Morton [1991]. The emission intensity distribution of these rotational lines follows the Maxwell-Boltzmann distribution law multiplied by a degeneracy factor $2J + 1 = J' + J'' + 1$, and becomes

$$I_{em} = \frac{C_{em}\bar{\nu}^4}{Q_r}(J' + J'' + 1)e^{-\overline{B}_{N2}J'(J'+1)hc/kT_r} \tag{5.5}$$

where C_{em} (for emission) is a constant depending on the total number of molecules in the initial vibrational level and change of dipole moment. Q_r is the rotational state sum, B_{N_2} is the rotational constant in the neutral N_2 ground state, T_r is the rotational temperature and k is the Boltzmann constant. For a given band, it follows that the relative intensities of a rotation vibration band are given by

$$I_P \propto \bar{\nu}_P^4(2J)d_n e^{-\overline{B}_{N2}(J-1)Jhc/kT_r} \tag{5.6}$$

$$I_R \propto \bar{\nu}_R^4(2J + 2)d_n e^{-\overline{B}_{N2}(J+1)(J+2)hc/kT_r} \tag{5.7}$$

where d_n is the statistical weight for nuclear spin, which introduces an intensity alternation of neighbouring rotational lines. It follows from the selection rule $J' - J = \pm 1$ that the even rotational number energy levels of N_2 X can only combine with the odd energy levels of N_2^+ X and that the transitions can only connect with rotational levels of equal nuclear spin degeneracy. This results in molecular nitrogen bands having an intensity ratio of 2:1 between even and odd numbers of rotational quantum number. Molecular constants for the modelling of synthetic spectra of molecular nitrogen bands can be found in Lofthus et al. [1977]. A typical modelled rotational structure of the N_2^+ 1N (0,2) band can be seen in Fig. 5.1. The behaviour of a typical Fortrat parabola that is expected on the basis of equations 5.3 and 5.4 is observed. Synthetic line spectra are convolved with a triangular instrument function of FWHM of 0.08 nm to acquire a theoretical convolved intensity as shown in Fig. 5.2 for the recorded HiTIES wavelength range 468.5–471.5 nm.

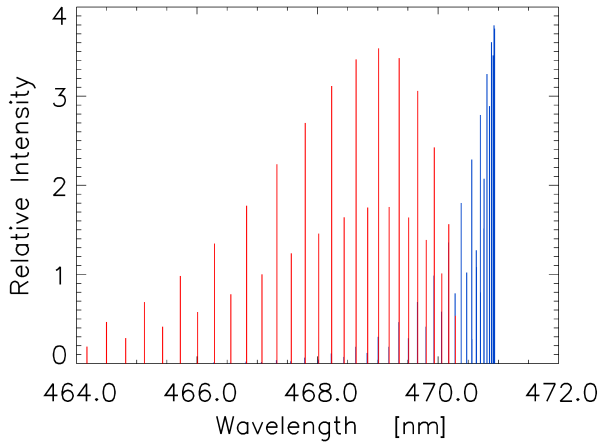

Figure 5.1: *Relative rotational intensities of P-branch (blue) and R-branch (red) of N_2^+ 1N (0,2) synthetic spectra at 700 K. The band head forms in the P branch since $\overline{B}' > \overline{B}''$.*

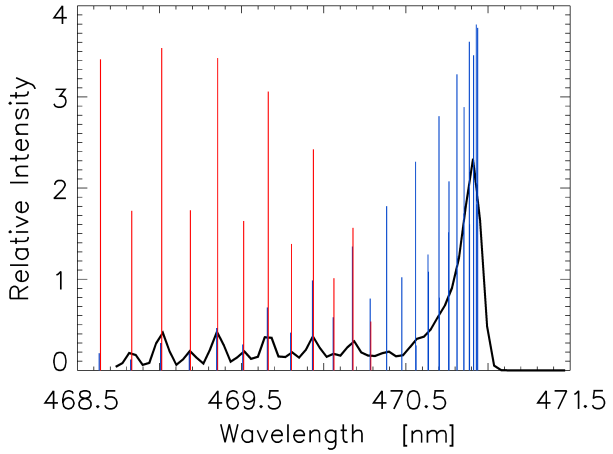

Figure 5.2: *Relative synthetic convolved spectra (black) superimposed on the synthetic rotational P- (blue) and R- (red) branches at 700 K within the recorded wavelength interval of N_2^+ 1N (0,2) in HiTIES.*

5.4 Data Analysis

The rotational temperature distribution of neutral N_2 is in thermal equilibrium with the surrounding species. Electron impact excitation from neutral N_2 X to N_2^+ B preserves

the distribution between the rotational levels so that for the ions $T_r = T_n$, where T_n is the neutral temperature. Therefore it is assumed that measurements of the N_2^+ 1N band structure yields the neutral temperature of the emitting species.

The χ^2 statistic [Squires, 2001] is used to fit the observed profile and theoretical curve, where both scale factor and background are variable. This is given by

$$\chi^2 = \sum_{i=1}^{N} \left(\frac{e_i - \beta - \alpha t_i(T_r)}{\sigma_i} \right)^2 \tag{5.8}$$

where the e_i represent observed spectral intensities, β the background level, α the scale factor of the theoretical convolved line intensities t_i, T_r the rotational temperature, σ the standard deviation of the measured intensities and N the number of independent data points.

χ^2 is minimised with respect to α, β and T_r. Since the expression is a quadratic in α and β, this leads to the linear equations

$$\alpha = \frac{\sum e_i t_i(T_r) - \sum e_i \sum t_i(T_r)}{\sum t_i^2(T_r) - \sum t_i(T_r) \sum t_i(T_r)} \tag{5.9}$$

$$\beta = \sum e_i - \frac{\sum e_i t_i(T_r) - \sum e_i \sum t_i(T_r)}{\sum t_i^2(T_r) - \sum t_i(T_r) \sum t_i(T_r)} \sum t_i(T_r)$$

Minimisation of χ^2 is performed by plotting χ^2 with respect to T_r. Some typical curves are shown later in Fig. 5.10. If there is no aurora in the field of view then there may be no parabolic minimum in χ^2. In order to estimate the magnitude of the errors, the accuracy of the spectrograph allows us to assume the data points along the wavelength scale are statistically independent, so that the number of independent data points is simply the wavelength range divided by the spectrograph resolution.

It is not practical to measure σ, so the following argument is used to estimate the error ΔT_r in T_r. Assuming that the expected value of χ^2 from N independent measurements is equal to N allows an estimate of σ^2 to be made. If T_r is changed from $T_{rminimum}$ by one standard deviation ΔT_r, χ^2 should increase by unity. So for any constant σ

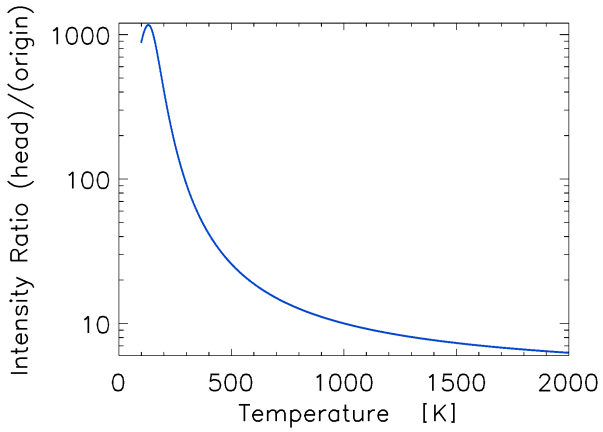

Figure 5.3: *Variation of the ratio of the intensity at the band head (470.9 nm) to the intensity at the band origin (470.5 nm) as a function of temperature.*

$$\chi^2(T_{rminimum} + \Delta T_r) = \frac{N+1}{N}\chi^2(T_{rminimum}) \tag{5.10}$$

The most dynamic aspect of the rotational spectrum as a function of temperature is the intensity at the band origin at 470.5 nm with respect to the intensity at the band head at 470.9 nm. The variability of this ratio is shown in Fig. 5.3. At $T_r < 500$ K the P-branch is mostly situated at the band head and the band origin is void of any rotational lines from the R-branch. Above this temperature the P-branch starts to spread beyond the band origin and overlap with the R-branch as seen in Fig. 5.1. A single temperature is fitted to a height integrated temperature profile and in order to make the fitting at the band origin agree with the overall χ^2 fit the relative standard deviation used is made dependent on wavelength.

As a consequence of the narrow rectangular slit at the input of the spectrograph, the CCD image is curved in the magnetic north-south direction [Chakrabarti et al., 2001]. This is due to off-axis diffraction, the magnitude of which is wavelength dependent and means that the measured rotational lines are shifted on the wavelength scale along the magnetic meridian. A polynomial function was therefore applied to straighten the image. Because of the importance to match the synthetic spectra to the high resolution data

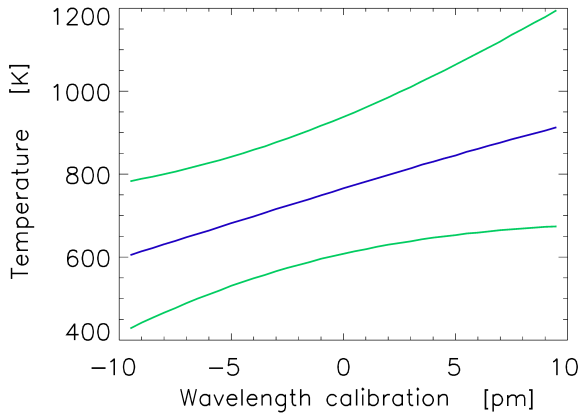

Figure 5.4: *The effect of wavelength calibration on best fitted temperature (blue) and error range (green) during a typical auroral event. Wavelength scale is in picometers.*

accurately, fine wavelength calibration was also verified. To do this the pre-convolution theoretical spectrum was shifted with respect to the observed data. With the instrument function this will directly affect the shape of the convolved theoretical band. As a result, it can be seen in Fig. 5.4 that shifts of only 0.005 nm can lead to changes in temperature of the order of 100 K.

Measurements from the N_2^+ 1N (1,3) band are also used as an additional source of information. This wavelength range of the HiTIES mosaic filter includes the lines of the multiplet O^+ (^4P-$^4D^0$), which blend with the N_2^+ 1N(1,3) band, and are of comparable strength. An example of a measured spectrum from the spectrograph which includes both emissions, and a convolved theoretical spectrum of the nitrogen band are shown in Fig. 5.5. The relative intensity of the O^+ lines and N_2^+ bands is directly related to the energy of the incoming electron distribution [Ivchenko et al., 2004].

More supporting observations are electron density height profiles from the Eiscat Svalbard Radar (ESR). These are combined with an auroral model which provides a method of estimating the energy flux and peak energy of the incident electrons. It uses a one-dimensional electron transport code [Lummerzheim and Lilensten, 1994] and ion-chemistry equations (see appendix Lanchester et al. [2001]). For the present

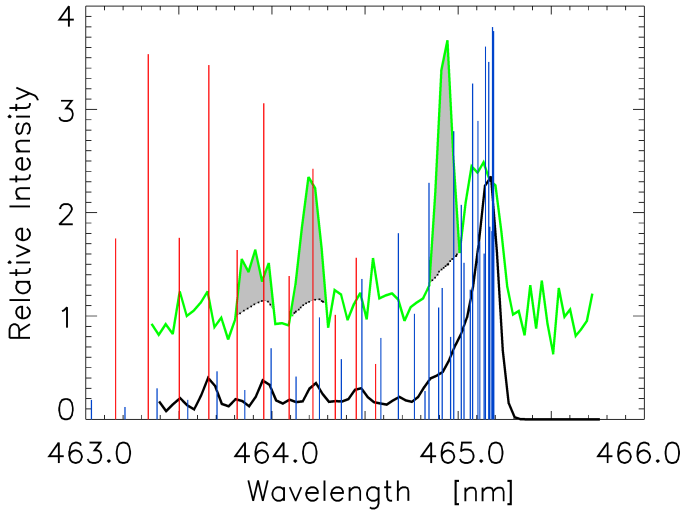

Figure 5.5: *Theoretical relative intensities of N_2^+ 1N (1,3) P-branch (blue) and R-branch (red) with superimposed theoretical convolved intensities (black) and measured spectrographic profile (green) lifted up in the vertical scale, in which the three O^+ (^4P-$^4D^O$) lines are clearly visible and marked grey.*

data a simple method is used to fit the radar measurements to model height profiles of ionisation rates. However, the method shows clearly that the real energy spectrum of precipitating electrons is a much more complicated combination of several shapes, especially at time resolution of 30 s.

A flow diagram of the experimental approach is given in Fig. 5.6, following a similar system described in Vallance Jones et al. [1987]. The spectrographic optical data provide the intensity of the two nitrogen bands (1,3) and (0,2). The latter is used to give a single, height integrated rotational temperature, which is then combined with the MSIS neutral temperature as a function of height, $T_{\mathrm{n}}(h)$, to give an estimate of the height of the emissions. Thus the average energy $\langle E \rangle$ of the precipitating electrons can be estimated from height integrated emission profiles. This can correspond to either Maxwellian or Gaussian distribution or partly both. The intensity of the oxygen lines found within the wavelength range of the N_2^+ 1N (1,3) band relative to the intensity of the nitrogen bands

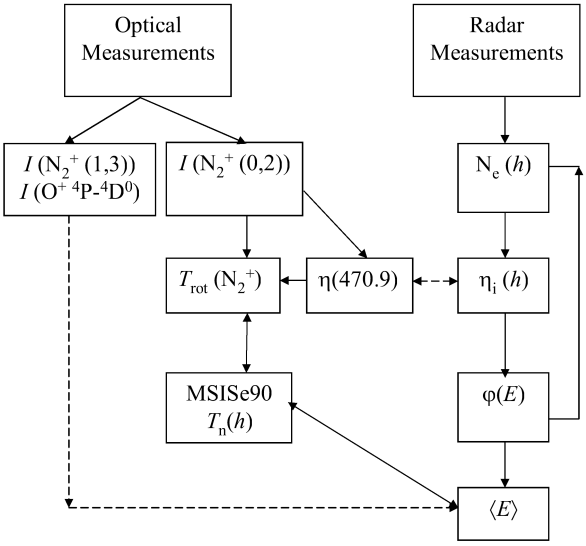

Figure 5.6: *Schematic diagram showing measured and modelled quantities starting from optical and radar input. Arrows show the possible paths linking the two.*

is an additional route to the average energy. The radar measurements give height profiles of electron densities and ionisation rate profiles, and thus an energy distribution function $\phi(E)$ and an estimate of the average energy. The height integrated production of 470.9 nm emission can be calculated by the model and compared with that measured, to complete the cycle. The last step will be done in future studies when more data sets at higher time resolution will be available. The present work is primarily to report the full details of the method for obtaining rotational temperatures from high resolution spectral data.

5.5 Results

5.5.1 Magnetic zenith

Strong electron precipitation was observed over Svalbard on 14 January, 2002. An overview of the events analysed in this work is shown in Fig. 5.7, which is a time se-

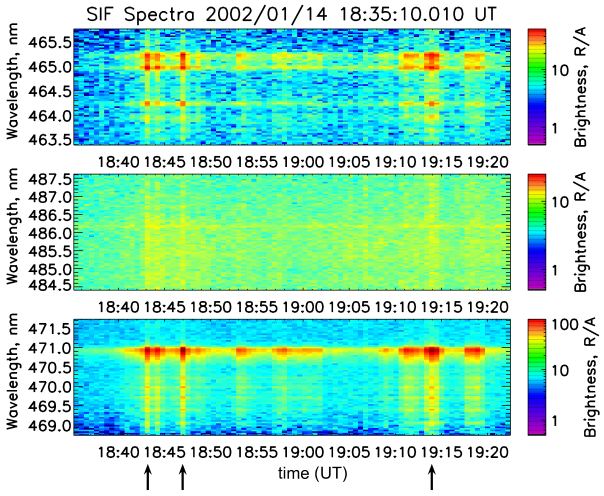

Figure 5.7: *Electron precipitation events between 18:30–19:25 UT on 14 Jan 2002, measured with HiTIES: (first panel) N_2^+ 1N (1,3) (465.2 nm) and $O^+(^4P\text{-}^4D^O)$ lines, (second panel) H_β (486.1 nm), (third panel) N_2^+ 1N (0,2) (470.9 nm).*

ries of the spectrographic measurements over an hour from 18:30 UT. The top panel is N_2^+ 1N (1,3) with band head at 465.2 nm. This includes the $O^+(^4P\text{-}^4D^0)$ lines, which have been reported in Ivchenko et al. [2004]. The middle panel contains the Balmer H_β line; in the chosen interval there is a faint unshifted line at 486.1 nm from geocoronal hydrogen, and background Vegard-Kaplan band at the times of electron precipitation. This confirms that there is no significant Doppler shifted H_β, and therefore no proton precipitation during these events. The third panel is the N_2^+ 1N (0,2) with band head at 470.9 nm. Arrows mark the times of three main events used for the temperature analysis at around 18:42 UT, 18:46 UT and 19:13 UT.

The radar (ESR) data from the same interval are shown in Fig. 5.8. The arrows again mark the events at 18:42 UT, 18:46 UT and 19:13 UT. The top panel shows that there is a strong increase in ion temperature preceding the first of these intervals, indicating the presence of electric fields in the region in advance of the auroral activity. There is also a large increase in electron temperature (panel 2) accompanying the event at

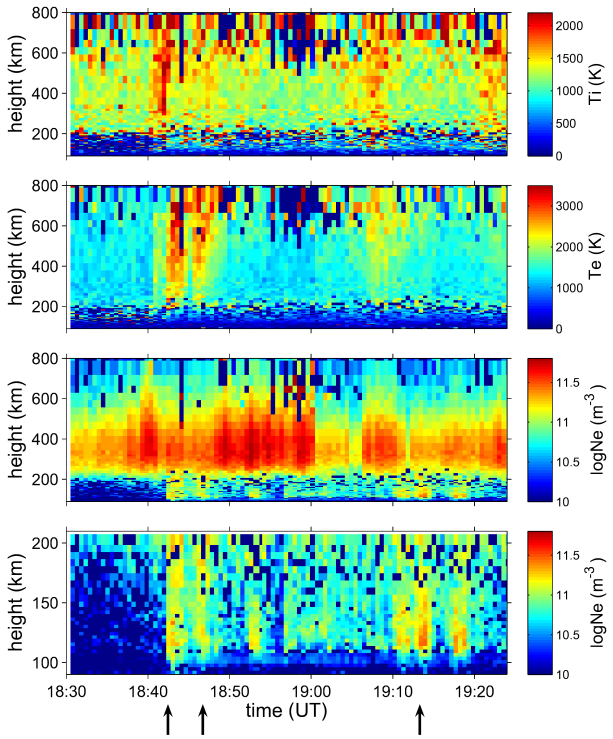

Figure 5.8: *Overview of radar measurements between 18:30–19:25 UT on 14 January, 2002. Height profiles of ion temperature (first panel), electron temperature (second panel), F-region electron density (third panel) and E-region electron density (fourth panel).*

18:42 UT, and again to a lesser extent at 18:46 UT, but not at 19:13 UT. The F-region electron density in panel 3 is variable throughout the hour and could be the result of ionisation moving into the region across the polar cap, or soft precipitation causing ionisation at these heights. The precipitation that produces the auroral signatures is seen at the lowest heights in panel 3. These E region densities have been reproduced in panel 4 to show the differences in the distribution of ionisation in the chosen events over the height range 90–210 km.

The fitted N_2^+ 1N (0,2) band for the chosen intervals are shown in Fig. 5.9. Frames from the auroral imager demonstrate the type of aurora that was in the field of view during the spectrographic and radar measurements are shown on the right. The spectral

profiles are taken from 1° of the slit in the magnetic zenith and integrated over 30 s. The auroral image, on the other hand, is one frame lasting only a fraction of a second. In the first event, starting at 18:42:22 UT, the aurora was almost totally made up of rays, sometimes in rayed arc formation. In the second example shown (part of the same event), starting at 18:43:27 UT, the rayed arc is more evident with rays still dominating the aurora. In the third example (second event), starting at 18:46:13 UT, another auroral arc moved from the north into the field of view. This arc is without rayed structure, and has a curl forming along its length. The arc moved from the north (bottom) into the region of the magnetic zenith without fully entering the radar beam. (Note that the radar beam is in the southern region of the slit.) Temperature analysis was successfully performed, both in the zenith position and along the slit to the north, discussed below. Comparison with radar data is used only as a source of background ionisation in this event. In the final event, starting at 19:13:19 UT, the aurora was very different in nature. Diffuse forms moved across the field of view, with dark lanes appearing at times. All of the above features are difficult to represent in still images.

The χ^2 fitted curves for the three distinct auroral events are shown in Fig. 5.10. The minimum of the parabola represents the best fit temperature. A wider parabola indicates uncertainty in T_r which can be due to random errors in the data and systematic errors due to a wider emission altitude range. The temperatures resulting from these fits, with their errors, are given at the top of each panel in Fig. 5.9 and in Table 5.1. At 18:42 UT and the subsequent interval shown in Fig. 5.9 one minute later, the aurora was dominated by rayed arcs, and the temperature was the highest value (800 K and 779 K respectively). At 18:46 UT the aurora was in the form of a curling arc, with a lower temperature of 754 K in the zenith, which contained the highest part of the arc. Its lower border remained to the north of the zenith. This event is the best example of when the temperature from along the meridian slit is valuable. It is discussed further in Sect. 5.3. At 19:13 UT, during diffuse aurora, the temperature was at its lowest in the zenith (646 K).

The next stage of this analysis involves a simple application of a one-dimensional auroral model developed for the purpose of estimating energy fluxes and peak energies in electron precipitation regions [Palmer, 1995]. In this method, an ionisation rate profile inferred from radar data is matched against model ionisation rate profiles, both Maxwellian and Gaussian (10% width), computed with a neutral atmosphere appropriate for the given position and date. This method provides an estimate of the main contributor to the energy spectrum. It is clear from previous work [Lanchester et al., 1997] and from this present analysis with relatively long integration times that the input spectrum is invariably much more complex, and is usually a mixture of more than one simple distribution. This has implications for the present results in the form that the electron energy spectra is an average of various energies over the time period in question.

Two examples are shown in Fig. 5.11 of the fitted ionisation rate profiles. The EISCAT electron densities have been converted to ionisation rate profiles, assuming a constant recombination rate coefficient. Although this is an approximation, it allows a good estimate of the peak energy of the precipitating flux. It also gives reasonable limits for the energy flux. In the first panel of Fig. 5.11 at 18:42 UT, the radar profiles are fitted well by a Maxwellian distribution at the lowest heights, with peak energy of about 1 keV. However, above 170 km the measured profile is not fitted. Another distribution is present at these heights. In the second panel, at 19:13 UT, both a Maxwellian and a Gaussian have been fitted, showing that the real spectrum is a mixture of more than one distribution. The peak energy from the Gaussian is 3.4 keV. Again, there is another distribution this time above 140 km, but not as marked as in the previous example. This difference can be seen in Fig. 5.8, comparing the times marked with the first and third arrows. There is a clear region of increased electron density above 170 km at 18:42 UT, and a less intense increase at around 150 km at 19:13 UT. The peak energies inferred from the fitted profiles for three times shown in Fig. 5.9 are included in Table 5.1. The rayed aurora is associated with smaller values of energy of precipitation (maximum of

1 keV) and corresponds to larger neutral temperatures. As already noted, the curling arc of the second event was not fully measured by the radar at 18:46 UT and is not included in the zenith analysis. Larger values of precipitation energy (maximum of 3.4 keV) occurred during the diffuse aurora, which corresponds to the smallest neutral temperatures in the zenith.

Estimates of the energy flux are also included in the table, although these are only a guide for comparison between events. The fits do not account for populations observed in the upper E region, which also means that the peak energy is representative of only one population. The average energy from neutral temperature will include contributions from all populations.

As described in the flow diagram of Fig. 5.6, the two approaches taken above can be compared by estimating the energy of the precipitation from both optical and radar measurements. The MSISe90 atmospheric model for the 14 January 2002 has been used to convert the derived neutral temperatures to average heights of emission. The results are included in Table 5.1. The auroral model [Palmer, 1995] is again used to provide a value for the energy associated with maximum emission at the estimated heights. These are included in Table 5.1. In the first two intervals, Maxwellian distributions were used following the evidence from the radar observations. Monoenergetic beams of electrons approximated by a Gaussian distribution were used for the third event. This is of course a gross assumption, since the ionisation rate profiles clearly show that the real distributions must be much more complex, and in all cases lower energy populations were also present. However, the agreement between the energy from optical methods, and the peak energy from radar is reasonable. In all cases the peak energy is approximately double the optically derived energy. This is not a property of the Maxwellian or Gaussian shape assumed, but of the profile-integration included in the optical method, and not in the radar method. The spectral emissions from the spectrograph are height integrated averages whereas the peak energy comes from the peak of the electron density profiles.

time (UT)	*type*	T_n *zenith* (K)	*height* (km)	$\langle E \rangle$ *optical* (keV)	*main* $\varphi(E)$ *radar*	*E, radar* (keV)	*Flux, radar* (mWm^2)	*emission ratio* $I(O/N)\times 100$
18:42	rays	$800 \pm 50/47$	156 ± 6	0.5 (M)	Maxwellian	1.0	2.4	17.32
18:43	rayed arc	$779 \pm 67/62$	154 ± 8	0.5 (M)	Maxwellian	1.0	4.0	
18:46	curled arc	$754 \pm 50/49$	150 ± 5	1.2 (G)				6.90
19:13	diffuse	$646 \pm 34/32$	139 ± 4	1.5 (G)	Gaussian	3.4	4.1	10.23

Table 5.1: *Summary of derived temperature, estimated energy distributions, and ratio of emissions* I(O^+)/I(N_2^+ *(0,2)) at four chosen times, in different types of aurora.*

5.5.2 Emission ratios

The events of 14 January 2002 during the same time interval have been used in a separate analysis by Ivchenko et al. [2004]. The purpose of that work was to report observations of O^+ lines in electron aurora over Svalbard, and to use measurements of the brightness of these lines compared with the brightness of the N_2^+ 1N (0,2) band (see Fig. 5.5) to estimate the cross section for production of the multiplet in electron collisions. That work showed how the variation of the ratio of the brightnesses is linked with the type of aurora, and hence with the energy of precipitation, and the height at which the emissions are maximum. The most common value of the ratio of these emission brightnesses was found to be about 0.1. In the first event here, the predominance of O^+ lines over the N_2^+ is very clear with a ratio 0.17, and confirms the observation that the O^+ emissions are associated with low energy precipitation within rayed aurora. The second event with the curling arc (well-measured by the spectrograph but not the radar) gives a ratio well below 0.1, when the N_2^+ emission dominates. In the third event the ratio is at a normal level close to 0.1. The temperature results from the same events are consistent with the above interpretation, and provide the dashed link in the flow diagram of Fig. 5.6.

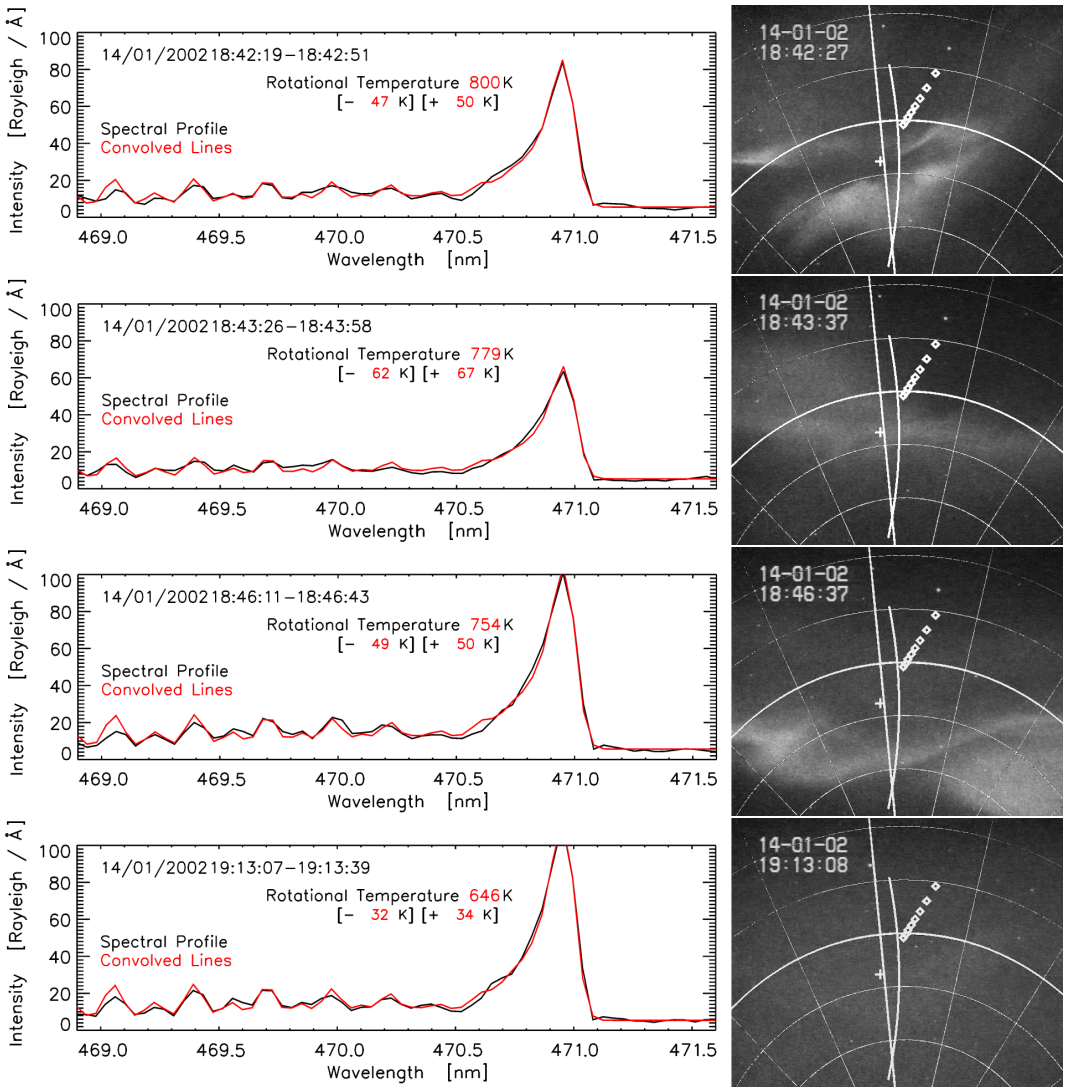

Figure 5.9: *Spectral fits for aurora at 18:42 UT, 18:43 UT, 18:46 UT and 19:13 UT (left). Rotational temperature decreases from top (rays) to bottom (diffuse). Images from the narrow angle auroral imager (right); the spectrograph slit position and the radar beam projected to heights 100–240 km with 20 km separation are shown in each image. South is at the top and east on the right. The location of the magnetic zenith is indicated with a cross.*

5.5.3 Along the meridian slit

The original spectrograph design was intended to provide information about auroral variations along the magnetic meridian centred on the magnetic zenith. At the time

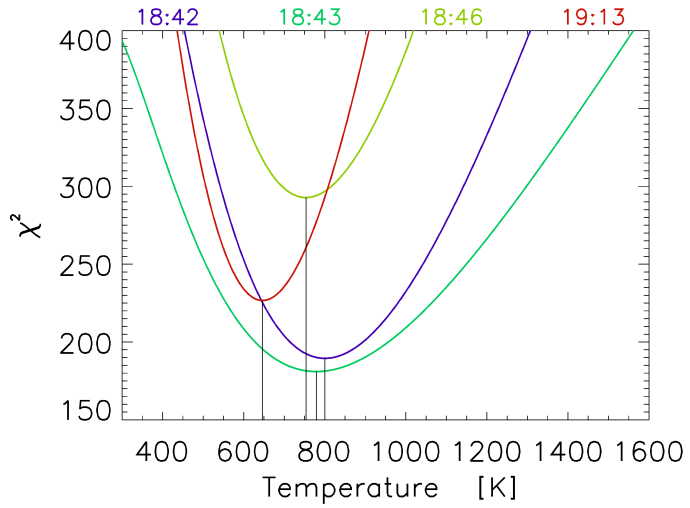

Figure 5.10: χ^2 *fit curves for the four intervals of electron precipitation at 18:42 UT, 18:43 UT, 18:46 UT and 19:13 UT on 14 January, 2002.*

resolution of the present data of 30 s, the variations in the aurora must be considered carefully. As an extra check on the validity of the zenith results, the variation of derived temperatures across the meridian slit of the spectrograph has been examined in all of the above events. In the first event, the aurora was consistently rayed, which can be approximated by a distribution along the slit with lower energies nearer the middle. In the second event, the curling arc was seen to reach the zenith, and stay with its lower border to the north of the zenith for most of the integration time. In this example it was advantageous that a measurement of temperature could be made at the maximum intensity in the arc, with less contamination from the integrated profile. The third event was made up of diffuse aurora which mostly filled the slit, with the exception of dark lanes for short intervals.

The geometry of the optical instruments is shown in Fig. 5.12 with three possible arc positions marked. Arc A corresponds to the results of Sec.5.1, where the zenith measurements are necessarily an integration over all heights in the aurora that enters this region; the derived temperatures are therefore dominated by the type of aurora that

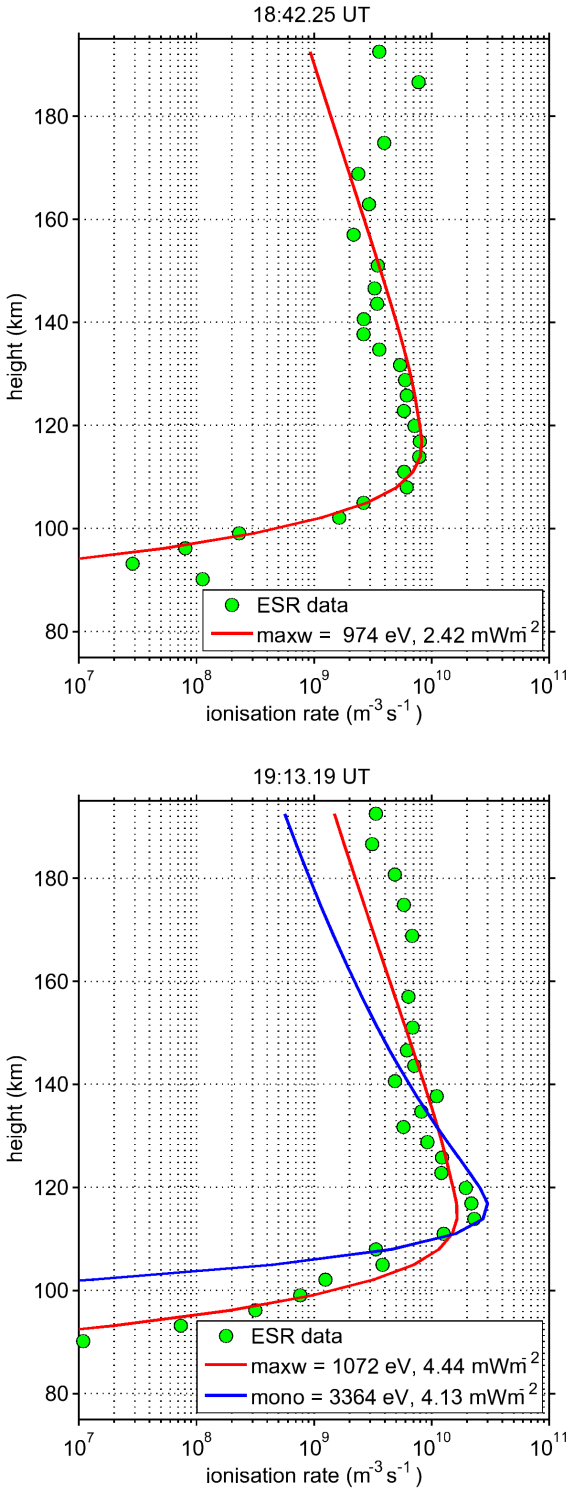

Figure 5.11: *Ionisation rate profiles from radar, and fitted profiles from model for rayed aurora (18:42 UT) and diffuse aurora (19:13 UT).*

is present. In order to estimate changes in the temperature associated with different heights within an auroral feature, ideally an arc must stay in a position such as that marked B for the integration interval. In such a case, the region to the edge of the slit measures the lower part of the arc (lower temperatures and marked in green) with temperature increasing towards the zenith point. Another possible situation is described by an arc in position C, which has its lower border out of the field of view of the slit, but its highest part is measured on the edge of the slit. This figure also demonstrates how each elevation angle (other than the magnetic zenith) may contain contributions from more than one auroral form. The data have been interpreted with careful consideration of all these possibilities.

The main problem with this approach is the need for temporal integration of the spectrograph profiles, which in the present data was 30 s, necessary for the detector in use at the time. From the video sequences throughout the events described it is clear that the aurora often varied on much shorter time scales than this, resulting in some spatial and temporal averaging. Given this caviat, the temperature fits for the data in the three events are consistent with the geometry of the aurora measured, and with the zenith measurements.

Each of the three events is represented in Fig. 5.13. The left hand panels in each are taken from the narrow angle camera, and show the variations in intensity in the region corresponding to the spectrograph slit for the integration interval of 30 s, shown as the time axis. The right hand panels are temperature fits in 1° slices. (The zenith value in each case is the temperature given in Table 5.1.). The spectrograph data from the N_2^+ 1N (1,3) filter with band head at 465.2 nm have been used as a diagnostic for the varying emissions along the slit. The $O^+(^4P\text{-}^4D^0)$ lines at 464.9 nm (the brightest), 464.2 nm and 463.9 nm, produced by low energy precipitation, were measured with variable brightnesses in different regions of the slit in each event. In Fig. 5.14 two spectra have been chosen from different elevation angles, to show the different contributions of the $O^+(^4P\text{-}^4D^0)$ lines relative to the N_2^+ 1N (1,3) band head. For the first event, starting at 18:42 UT

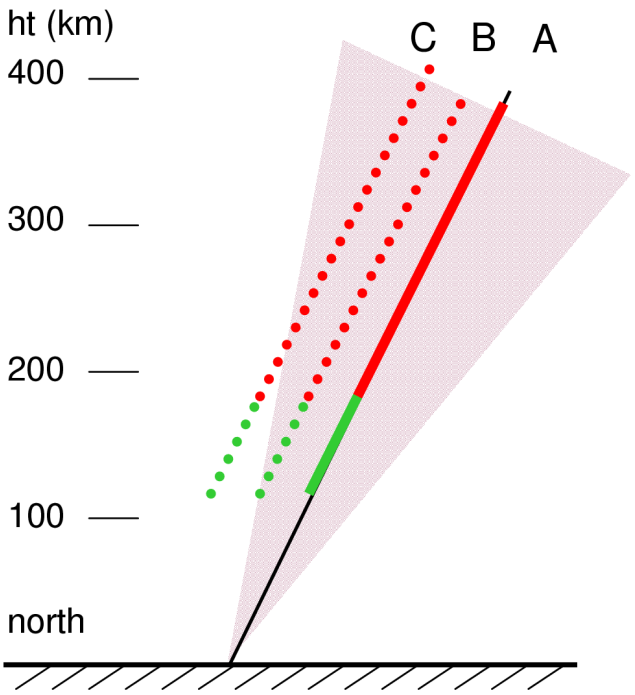

Figure 5.12: *Schematic diagram (not to scale) of the geometry of the HiTIES spectrograph with auroral arcs in three positions in the field of view. The shaded area represents the 8° slit along the magnetic meridian. Arc at position A corresponds to the magnetic zenith. Green colour corresponds to low altitudes and low rotational temperatures, the red colour corresponds to high altitude and high rotational temperatures.*

oxygen lines dominate, and in particular at the position 1° north of the zenith, where the temperature is indeed even higher (850 K) than that in the zenith (800 K). The nitrogen band is stronger to the south of the zenith where the temperature decreases with angle of elevation, as given by aurora in position B in Fig. 5.12. This result agrees with the observation that the rays were distributed through this region and the brighter features were seen mostly in the southern half of the field of view. The second interval at 18:43 UT is a continuation of the same event of rayed arcs in the field of view. It gives a similar result, with maximum temperature of 800 K at the zenith position, decreasing to 600 K away from the zenith. This corresponds to a temporal integration producing an

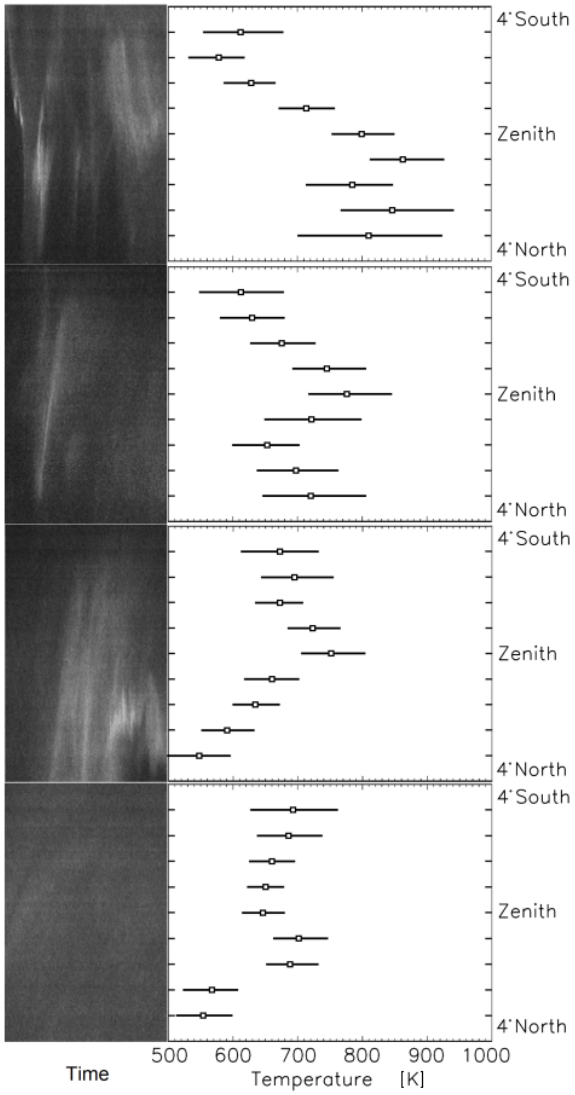

Figure 5.13: *From top to bottom at 18:42 UT, 18:43 UT, 18:46 UT and 19:13 UT: (left panels) intensity in slit measured by narrow angle camera over 30 s; (right panels) rotational temperatures in 1° steps along the HiTIES slit.*

average temperature profile at each elevation angle. The intensity of the oxygen lines is above that of the nitrogen band over the whole slit.

In the second event at 18:46 UT, a curling arc approached from the north and only

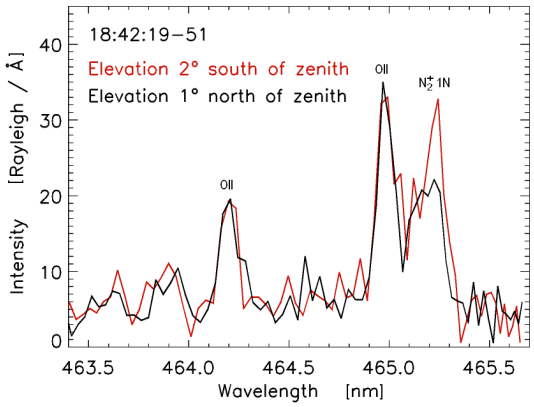

Figure 5.14: *Spectra from two elevation angles across the HiTIES slit at 18:42 UT, showing the relative change in intensity of the Oxygen lines with respect to the Nitrogen band head, corresponding to changes in the derived temperature seen in Fig. 5.13.*

briefly moved into the zenith. Weaker aurora was seen for part of the interval just south of the zenith. The resulting temperature profile is in agreement with this finding, with lowest temperatures of 550 K at the northern edge, corresponding to the lower border of the arc, and highest temperatures in the zenith. This corresponds to an energy in the lower border of the arc of a few keV, originating from heights of 120 km, a very reasonable result for a curling bright arc [Rees, 1989]. Fig. 5.15 shows that the nitrogen band head dominates the spectral measurements on the northern side of the slit. South of the zenith in weaker aurora, the oxygen lines are slightly more prominent again.

Finally, the event at 19:13 UT is quite different in all respects. The aurora shows very little structure along the slit, as do the temperatures. In the southern half of the slit the temperatures do not reduce towards the edge and are all below 700 K. The zenith measurement of 650 K is in fact the lowest value, with an increase of nitrogen band here (not shown). The very low temperature at the northern edge appears to be associated with a sharp edge between diffuse aurora and a dark lane that moves across the field of view. Higher time resolution is needed to study such features.

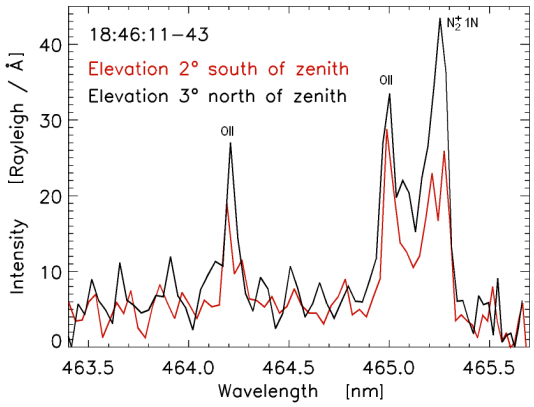

Figure 5.15: *Spectra from two elevation angles across the HiTIES slit at 18:46 UT, showing the dominance of the Nitrogen band head at elevation angle 3° north of zenith, corresponding to low values of derived temperature shown in Fig. 5.13.*

5.6 Discussion

The fitting of measured nitrogen bands to theoretical spectra convolved with the HiTIES instrument function as a function of temperature is the primary motivation for the present work. The analysis has been performed with particular attention to errors in the fit, with consideration for the assumptions inherent in noisy data. The inclusion of the background as an unknown parameter in the fitting means that this is a dynamic process, and much more likely to produce accurate temperatures than the use of an average background value. The consistency of the resulting temperatures with our understanding of the physical processes in the auroral ionosphere gives confidence in the experiment.

The analysis has been performed for magnetic zenith profiles, as well as for measurements at small elevation angles away from the zenith which, with careful choice, represent measurements at different heights of an auroral form. The time resolution of the data is the limitation in such an analysis, and this has been taken into account in the events chosen. Higher time resolution using a new detector will be used in future.

The spread in fitted temperatures between 500–900 K corresponds to a height range of approximately 120–170 km when compared with the MSIS atmospheric model. This is very close to the height range of emission maxima in aurora at the latitude of Svalbard. As can be seen from the table of results, the inferred average energies using the optical route are in good agreement with those derived from radar and modelling. The former gives energy estimates which are necessarily an average value, since they are derived from an integrated zenith measurement. The latter gives estimates of peak energy, derived from a height profile of ionisation rates. These peak energies are expected to be larger than the optical values, since they ignore the ionisation rate increases above the peak. In order to calculate a neutral temperature more accurately in the magnetic zenith, the analysis could be improved by fitting a height integrated temperature profile rather than a single temperature. This would compare more favorably with height integrated intensities derived from model and radar.

Interest in the chosen date and time interval stemmed from the results described in Ivchenko et al. [2004]. In their work, O^+ lines were found to dominate the N_2^+(1,3) band region at times of rayed aurora, and low energy precipitation. A very detailed analysis was made in that work of the intensity ratio $I(O^+)/I(N_2^+(0,2))$. The ratio is largest for the time of lowest energy, and highest temperature (18:42 UT). The lowest ratio is at the time of the curled arc (18:46 UT), when the N_2^+ bands were stronger. In this event, the measurements along the meridian are valuable. The temperature fits taken from north of the zenith confirm that the peak energy in this arc was several keV. For the final event with diffuse aurora the $I(O^+)/I(N_2^+(0,2))$ ratio has the average value of 0.1. The ionisation rate profiles from the radar indeed show that the distribution is not a single Maxwellian nor the result of a monoenergetic beam, but a combination of both in the lower E region, and another broader distribution above 150 km.

The possible effect of changes to the temperature of electrons and ions can be considered from the radar data. Electron temperatures, T_e, were raised to values above 2000 K over a wide height range as seen in Fig. 5.8 at the time of the first event between

18:42 UT and 18:44 UT. T_e will increase from heating due to precipitation, but also from the presence of field-aligned currents through Ohmic heating [Lanchester et al., 2001, Zhu et al., 2001]. The analysis of this event shows that there is an abundance of low energy electrons, with an increase in the ionisation rate profile above 170 km superimposed on the fitted Maxwellian. Low energy electrons are the main contributor to field-aligned current density. The measured increase in ion temperature immediately preceding this event also indicates the presence of strong currents, with horizontal electric fields and flows in the immediate region of the auroral precipitation [Lanchester et al., 1996, Zhu et al., 2001].

The absence of an increase in T_e in the diffuse aurora at 19:13 UT is also significant, suggesting that there are no strong field aligned currents, and not much heating from precipitation [Lanchester et al., 2001]. Here the neutral temperature is lower, as a result of an increase in precipitation energy. The values of the energy flux throughout the interval 18:30–1930 UT calculated from the 1-D auroral model show very similar energy fluxes for the times with rays and with diffuse aurora (see Table 5.1). As found by Henriksen et al. [1987], the fact that the results obtained for the energy of precipitation from optical and radar measurements are in good agreement implies that the changes in neutral temperature were caused by changes in the height of the emission region, and not on local heating. There is no evidence that the electron temperature increase has any direct effect on the neutral temperature measurements, although it corresponds with the time of greatest T_n. Further studies will be made to confirm this conclusion.

5.7 Conclusions

First results from spectrographic measurements at high spectral resolution provide neutral temperatures in the magnetic zenith and within auroral features close to the zenith. The analysis is more accurate than previous measurements, with particular attention paid to the errors associated with the background subtraction and wavelength calibration.

A clear trend in neutral temperature is found, with higher values for times of lower energy precipitation and vice versa. The events chosen contain times of very different auroral types, and clear differences in the neutral temperatures associated with them. The variation in neutral temperatures across the meridian slit was shown to be consistent the result from the zenith, with higher temperatures for regions at greater heights nearer the zenith, and lower temperatures in the lower borders of one arc in particular. An increasing temperature profile along the slit, from the edge of the slit to the zenith, was found during the time of rayed aurora, on both sides of the zenith.

Although there were large variations in the electron temperatures measured by the radar, the results suggest that there was no direct effect on the neutral temperature. Rather it is considered that the increases in both T_e and T_n at the time of rayed aurora were both associated with low energy precipitation. While the measured T_e increase is an actual temperature increase, the measured T_n increase results from the change of emission altitude in this type of precipitation.

Chapter 6

Modelling of populations of vibrational levels in the N_2 and N_2^+ molecular systems

6.1 Introduction

This chapter develops the theoretical basis for modelling of molecular nitrogen emissions from both the ASK imagers and the HiTIES spectrograph. N_2 1P emissions are measured by one of the ASK filters, from the (4,1) and (5,2) bands. Section 6.2 provides the foundation for results published in Ashrafi et al. (2009), which use the modelled N_2 emissions. Section 6.3 is the foundation for the statistical study which uses three N_2^+ 1N emission bands (0,1), (1,2) and (2,3) measured by HiTIES, as well as one N_2 2P (0,3) band. The results from this section are used in Chapter 7.

Molecular band emission profiles depend on the concentration of the parent vibrational level. Therefore modelling of these vibrational levels is a prerequisite for resolving the population factors of each vibrational level of each electronic state as a function of various ionospheric conditions. The N_2 and N_2^+ molecular emissions behave in different ways. The main processes for both populations are electron impact excitation followed by radiative transitions. We exclude other forms of excitation (i.e. photoionisation). Additionally, the N_2 emission profiles are affected by cascade transitions whereas the N_2^+ emission profiles are affected by resonance scattering and quenching, which are height dependent. The modelled emission profiles used in both studies are height integrated from the magnetic zenith.

An updated auroral ion chemistry model is used to compare modelled emission

rates with those measured by SIF and ASK, and therefore provides a means of estimating the energy spectrum of the precipitation producing the emissions. The ion chemistry model is based on the work of Palmer [1995] and is a time-dependent model which solves the electron transport equation, the coupled continuity equations for all important positive ions and minor neutral species, and the electron and ion energy equations. In order for the model to be run, the shape of the energy spectrum, peak energy and the energy flux for the precipitating electrons need to be specified for each time step. In the present work, a downward energy flux of 1 mW/m^2 is typically used and the ionisation rate profiles are generated for maxwellian and gaussian (10% width) spectra. The atmospheric conditions are set by geographic location and date using the MSIS-90 thermospheric model [Hedin, 1991]. Other inputs to the model calculations are electron impact cross sections of the major atmospheric neutral constituents. Cross sections for excitation and the energy losses of each individual excited state are required to calculate the energy degradation at each step, and the resulting emission profiles.

Solving the balance equations for the N_2 vibrational populations is required in the modelling of N_2 1P (4,1) and (5,2) emission rates. The production and loss terms of all the vibrational levels of the electronic states involved are needed to quantify the cascade contribution from higher levels to these two emission bands as opposed to emission resulting from direct excitation only. Observations from the ASK auroral imager in Tromsø, Norway in October 2006 have been used to compare with modelled emission rates in the two nitrogen bands. Several sets of cross sections have been considered, and selected cross sections have been used to construct emission cross sections for the observed bands. The resulting brightnesses are compared with those measured by ASK. The importance of specific contributions from cascading is found, with more than 50% of the total brightness resulting from cascading. This work is published in Ashrafi et al., 2009.

The solution of the balance equations to give the N_2^+ vibrational populations is used in the modelling of the N_2^+ 1N (0,1), (1,2) and (2,3) band emission ratios. These emission

profiles are significantly different depending on whether the aurora is non-sunlit or sunlit. No effect from cascading occurs within the ion species apart from the ground state. Observations from the HiTIES spectrograph in Svalbard, Norway, during the period of January to March of 2007 have been used to compare with these simulations. The comprehensive statistical study is the subject of Chapter 7 and was published in Jokiaho et al. [2009].

6.2 N_2 C, B, B', W and A states

The time dependent population of vibrational levels in the C, B and B', W and A states is described by

$$\frac{dn}{dt} = Production - Losses \tag{6.1}$$

The states are given in the order of decreasing zero point energy. The production of the excited populations is considered to be entirely due to electron impact on N_2 X. Radiative transitions from higher electronic states with vibrational energy levels v', to lower electronic states with vibrational energy levels v'' result in additional production of the lower electron states.

Loss terms of all vibrational levels are entirely due to all such radiative cascade transitions out of each level. The ion life time is several orders of magnitude longer than radiative lifetimes and hence is only important for the A state, whose radiative lifetimes of vibrational levels are 2 seconds and also the zeroth vibrational level of the W state, of the order of tens of seconds.

Inter-cascading affects the B, B', W and A states. In this case the energy of the topmost vibrational levels of a lower energy electronic state exceeds the energy of the ground vibrational level of a higher energy electronic state. This allows transitions occurring in the direction of $v'' \rightarrow v'$ and is by convention treated as a negative transition probability.

All electronic transitions involved in the modelling are tabulated in Table 6.1. The

potential energy curves can be found in Rees [1989]. The C, B, B' W and A states are created by direct electron impact on the neutral N_2 in the ground state. These states cascade down to lower levels. Molecules in the C electronic state de-excite down to the B-state following the appropriate transition probabilities. Likewise, the B state decays to the A state, from which the molecules react back into the ground state. Notice the inter-cascading between some of the states. These occur between the states of B↔A, B↔B' and B↔W. The C state is not affected by cascades.

excitation	cascades				
X → C	C → B	B → A	B' → B	W → B	A → X
X → B		B → B'			A → B
X → B'		B → W			
X → W					
X → A					

Table 6.1: *Considered electronic transitions.*

The equations for steady state populations ($\frac{dn}{dt} = 0$) are given in Eqs. 6.2- 6.6. The standard prime convention is used to describe vibrational levels. v''' relates to the N_2 X vibrational levels. The vibrational levels in the excited states are given by v' and v'', where the former is of higher energy than the latter. In the case of inter-state cascading $v'*$ is the higher vibrational level and v' is the lower level vibrational level of the cascade. The considered vibrational levels are 0-4 of the ground state, 0-4 for the C-state and 0-21 for the B, B', W and A states. These form altogether 93 excited vibrational levels.

The left hand side of the equations corresponds to production terms. The first term of Eqs. 6.2- 6.6 is the direct excitation term to each vibrational level of the involved states, where the excitation of N_2 X depends on the excitation rate η to each state (which depends on the electron impact excitation cross section and the incident electron energy flux). The vibrational population distribution depends on the Franck-Condon factors $q_{(v'''\rightarrow v')}$ from the ground state to the excited state. We use $\Upsilon_{v'''}$ to describe the thermal

distribution of vibrational levels in the X state as a function of vibrational temperature so that $\sum_{v'''} \Upsilon = 1$. Each product $q\Upsilon$ is summed over the X state vibrational levels 0-4 whose population distribution is thermal. The second term of Eqs. 6.3- 6.6 (there are no cascades to C state) is the cascading term from all the levels of the other states that have vibrational energies above the one considered and which are allowed by selection rules. These are the production terms resulting from cascade transitions, where the As are the transition probabilities and the ns are the source populations.

The right hand side of the equations corresponds to the loss terms. The first term here in Eqs. 6.2- 6.6 is the sum of all radiative losses from the vibrational level considered. The second loss term is the molecular collision frequency, which is insignificant for most levels (see above).

$$\sum_{v'''}(q^{C}_{(v'''\rightarrow v')}\Upsilon_{(v''')})\eta^{C} = \sum_{v''} A_{v'\rightarrow v''}n^{C}_{v'} + \frac{n^{C}_{v'}}{\tau} \quad (6.2)$$

$$\sum_{v'''}(q^{B}_{(v'''\rightarrow v')}\Upsilon_{(v''')})\eta^{B} + \sum_{C,B',W,A}^{\alpha}(\sum_{v'*} A_{v'*\rightarrow v'}n^{\alpha}_{v'*}) = \sum_{v''} A_{v'\rightarrow v''}n^{B}_{v'} + \frac{n^{B}_{v'}}{\tau} \quad (6.3)$$

$$\sum_{v'''}(q^{B'}_{(v'''\rightarrow v')}\Upsilon_{(v''')})\eta^{B'} + \sum_{v'*} A_{v'*\rightarrow v'}n^{B}_{v'*} = \sum_{v''} A_{v'\rightarrow v''}n^{B'}_{v'} + \frac{n^{B'}_{v'}}{\tau} \quad (6.4)$$

$$\sum_{v'''}(q^{W}_{(v'''\rightarrow v')}\Upsilon_{(v''')})\eta^{W} + \sum_{v'*} A_{v'*\rightarrow v'}n^{B}_{v'*}) = \sum_{v''} A_{v'\rightarrow v''}n^{W}_{v'} + \frac{n^{W}_{v'}}{\tau} \quad (6.5)$$

$$\sum_{v'''}(q^{A}_{(v'''\rightarrow v')}\Upsilon_{(v''')})\eta^{A} + \sum_{v'*} A_{v'*\rightarrow v'}n^{B}_{v'*}) = \sum_{v''} A_{v'\rightarrow v''}n^{A}_{v'} + \frac{n^{A}_{v'}}{\tau} \quad (6.6)$$

These equations can now be rearranged and written as

$$\mathrm{M}_{i,j}n_j = S_i \quad (6.7)$$

where $M_{i,j}$ is the matrix of coefficients containing all the production and loss processes whose layout is seen on the left of Fig. 6.1 describing the above equations. The Einstein coefficients depend only on the populations of the originating state. Therefore, for production, the Einstein coefficients depend on their states and vibrational levels

of origin (yellow) whereas for the loss factors, one is only interested in the total sum of Einstein coefficients i.e. molecules leaving the vibrational level in question (green). A convenient way to read the matrix is to consider each of the rows to describe the individual sources (in yellow) producing the particular vibrational level on that row. Likewise, each column describes the levels into which a specific vibrational levels decays (in yellow). The n_j are the steady state populations of all the vibrational levels in all the states and S_i is the constant matrix given by components involved in direct excitation. The S_i matrix element is seen on the right in Fig.6.1. Following the sign convention, terms describing the direct excitation terms are positive quantities, cascade production terms are negative and losses positive.

Solutions for the populations n_j of all the vibrational levels in all the states is obtained via matrix inversion.

$$n_j = M_{j,i}^{-1} S_i \tag{6.8}$$

The subscript j of matrix M^{-1} translates to vibrational level v', but because the total number of 93 vibrational levels belong to more than one state we assign an index k so that the first five indices are the vibrational levels belonging to the C state levels 0-4, the next indices between 6-27 belong to the 21 vibrational levels of the B state etc. The source vibrational levels are assigned with i. We are interested in emission profiles of

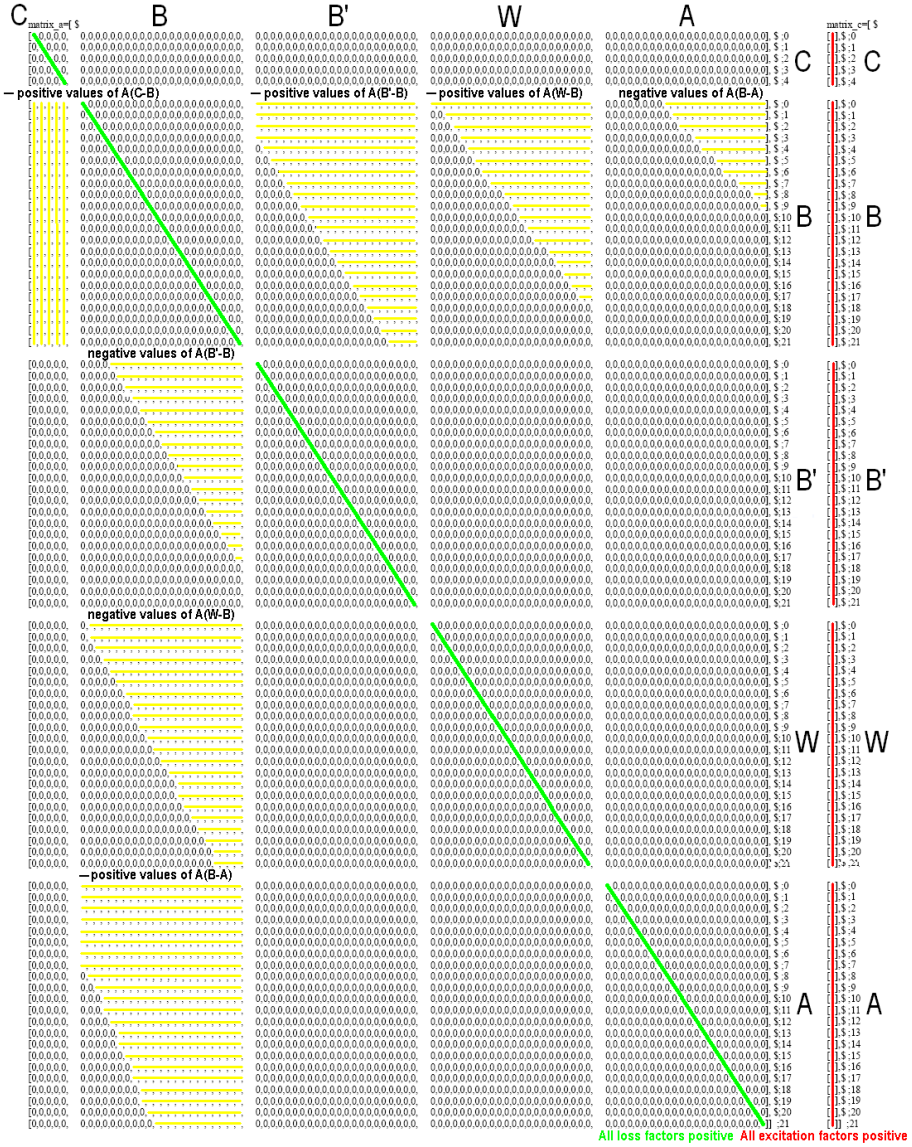

Figure 6.1: *The layout of the matrix of coefficients, $matrix_a$, for the 93 vibrational levels of C, B, B', W and A states of N_2. Production terms are marked in yellow and loss terms in green. The indices in one specific column in the matrix represent where the population of that level in question is lost: yellow indicates the individual loss transitions and green is the sum of all those radiative losses. The indices in one specific row in the matrix represents where population in that vibrational level in question is coming from: yellow indicates the individual production transitions and green is again the sum of all radiative loss factors. The $matrix_c$ of direct excitation is marked in red. The remainder of the indices in the matrix are zeros.*

the 1P system. Therefore, the emission rate between levels v' of B state and v'' of A is

$$\begin{aligned}
\eta_{v'-v''} &= A_{v'-v''} n^B_{v'} && (6.9)\\
&= A_{v'-v''} \sum_{i=1,5}^{C} (M^{-1}_{k,i} \sum_{v'''=0,4}^{C} q^{C}_{(v'''\to v')} \Upsilon_{(v''')}) \eta^C && (6.10)\\
&+ A_{v'-v''} \sum_{i=6,27}^{B} (M^{-1}_{k,i} \sum_{v'''=0,4}^{B} q^{B}_{(v'''\to v')} \Upsilon_{(v''')}) \eta^B \\
&+ A_{v'-v''} \sum_{i=28,49}^{B'} (M^{-1}_{k,i} \sum_{v'''=0,4}^{B'} q^{B'}_{(v'''\to v')}) \Upsilon_{(v''')}) \eta^{B'} \\
&+ A_{v'-v''} \sum_{i=50,71}^{W} (M^{-1}_{k,i} \sum_{v'''=0,4}^{W} q^{W}_{(v'''\to v')} \Upsilon_{(v''')}) \eta^W \\
&+ A_{v'-v''} \sum_{i=72,93}^{A} (M^{-1}_{k,i} \sum_{v'''=0,4}^{A} q^{A}_{(v'''\to v')} \Upsilon_{(v''')}) \eta^A
\end{aligned}$$

The emission rate can be written as

$$\eta_{v'-v''} = W_C \eta_C + W_B \eta_B + W_{B'} \eta_{B'} + W_W \eta_W + W_A \eta_A \quad (6.11)$$

where we can define

$$\begin{aligned}
W_C &= A_{v'-v''} \sum_{i=1,5}^{C} (M^{-1}_{k,i} \sum_{v'''=0,4}^{C} q^{C}_{(v'''\to v')} \Upsilon_{(v''')}) && (6.12)\\
W_B &= A_{v'-v''} \sum_{i=6,27}^{B} (M^{-1}_{k,i} \sum_{v'''=0,4}^{B} q^{B}_{(v'''\to v')} \Upsilon_{(v''')}) && (6.13)\\
W_{B'} &= A_{v'-v''} \sum_{i=28,49}^{B'} (M^{-1}_{k,i} \sum_{v'''=0,4}^{B'} q^{B'}_{(v'''\to v')}) \Upsilon_{(v''')}) && (6.14)\\
W_W &= A_{v'-v''} \sum_{i=50,71}^{W} (M^{-1}_{k,i} \sum_{v'''=0,4}^{W} q^{W}_{(v'''\to v')} \Upsilon_{(v''')}) && (6.15)\\
W_A &= A_{v'-v''} \sum_{i=72,93}^{A} (M^{-1}_{k,i} \sum_{v'''=0,4}^{A} q^{A}_{(v'''\to v')} \Upsilon_{(v''')}) && (6.16)
\end{aligned}$$

We can further write

$$\eta_{state} = \sigma_{state}\ \Phi(E) \tag{6.17}$$

where η_{state} is the production rate of a particular state, σ_{state} is the excitation cross section and $\Phi(E)$ the incident electron intensity which is a function of its energy E, (and also height and pitch angle), which can be acquired from the electron transport model.

We require an emission cross section σ_{total} that in product with the incoming electron flux yields the emission rate of the required emission band $\eta_{v'-v''}$. Therefore it can be written,

$$\begin{aligned} \sigma_{total}\ \Phi(E) = \ \eta_{v'-v''} &= W_C\sigma_C\ \Phi(E) + W_B\sigma_B\ \Phi(E) && (6.18)\\ &+ W_{B'}\sigma_{B'}\ \Phi(E) + W_W\sigma_W\ \Phi(E) + W_A\sigma_A\ \Phi(E). && (6.19) \end{aligned}$$

and the total emission cross section can be written as

$$\begin{aligned} \sigma_{total} &= W_C\sigma_C + W_B\sigma_B && (6.20)\\ &+ W_{B'}\sigma_{B'} + W_W\sigma_W + W_A\sigma_A, && (6.21) \end{aligned}$$

In the bands measured by the ASK instrument we model two emissions, N_2 1P (4,1) and (5,2), therefore $v' = 4$ and 5 are assigned with $k = 9$ and $k = 10$. The matrix is solved for the values of $W_C, W_B, W_{B'}, W_W$ and W_A for the two specified emission rates. Thermal equilibrium at 300 K of the neutral species is assumed. These are seen in Table 6.2.

The matrix is also solved for the general relative populations of vibrational levels of all the states as seen in Fig. 6.2 and Fig. 6.3 for each state respectively and with respect to the total excited N_2 population.

These distributions of populations are fixed with the assumption that radiative lifetimes are much faster than the ion life time and only depend on the vibrational distribution of levels in the thermal N_2 ground state. The emission rate ratio of η_{4-1} to η_{5-2} can further be modelled. This ratio is found to be 1.26 for excitation to C state only, 0.96 for the B-state only, 0.81 for B′ and 0.87 for W only so that

	(4,1)	(5,2)
W_C	0.0127	0.0107
W_B	0.0313	0.0351
$W_{B'}$	0.0312	0.0411
W_W	0.0292	0.0359
W_A	0.0104	0.0105

Table 6.2: *Values of $W_C, W_B, W_{B'}, W_W$ and W_A for emission rates of N_2 1P (4,1) and (5,2) for vibrational temperature of 300 K.*

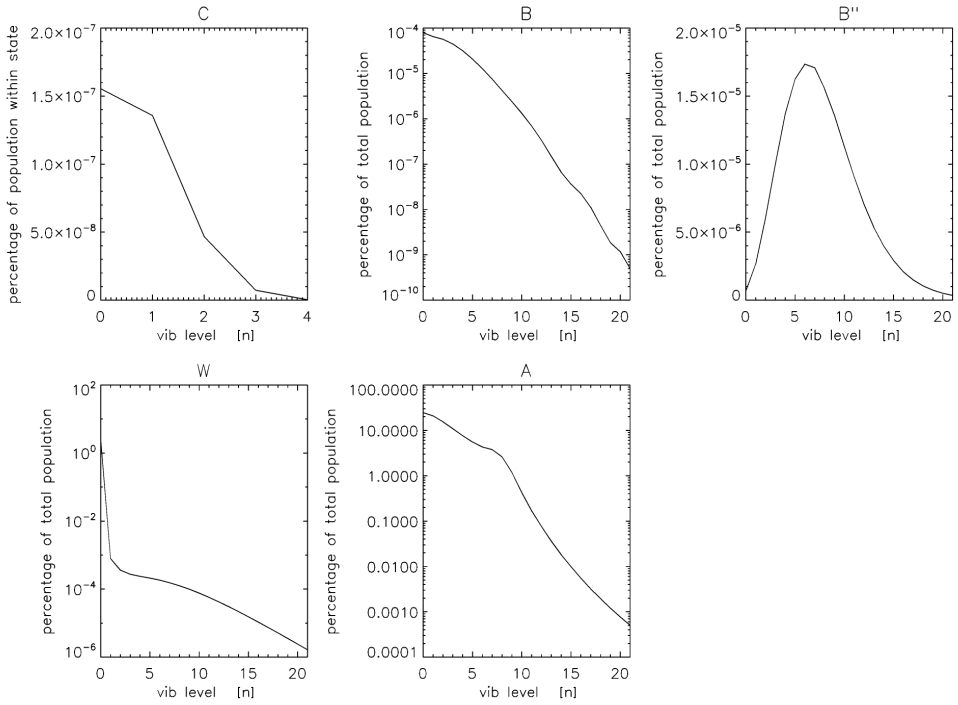

Figure 6.2: *The percentage vibrational population of N_2 C, B, B', W and A states.*

$$\frac{\eta_{4-1}}{\eta_{5-2}} = 1.26\,\gamma_C + 0.96\,\gamma_B + 0.81\,\gamma_{B'} + 0.87\,\gamma_W \tag{6.22}$$

where the γs are the excitation rates of each particular state over the total production.

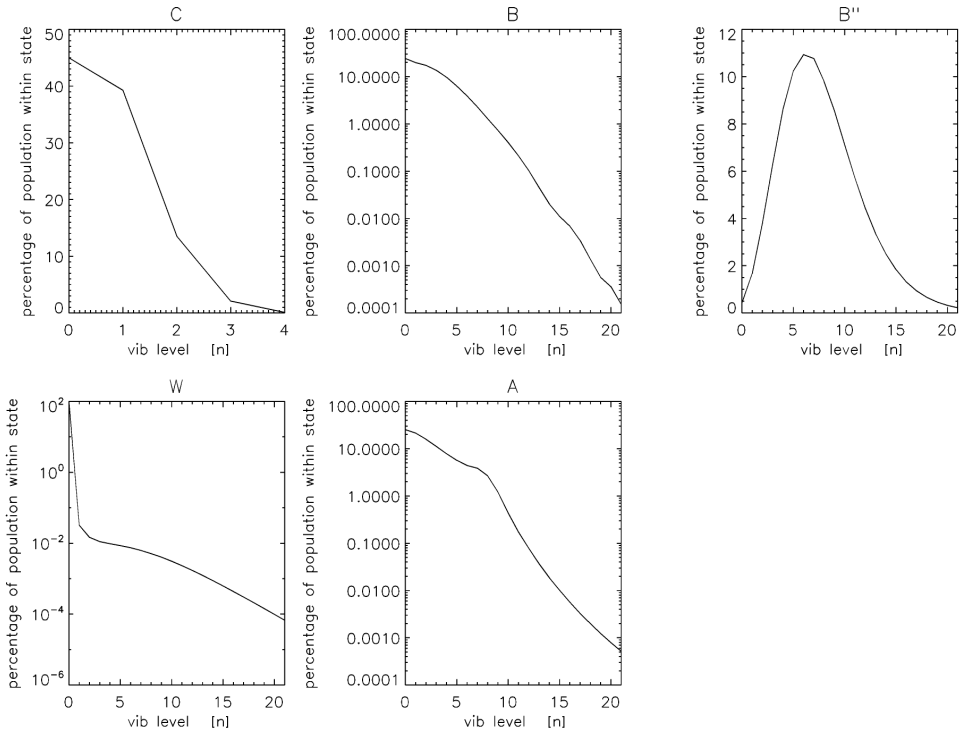

Figure 6.3: *The percentage vibrational population of N_2 C, B, B', W and A states with respect to the total excited population.*

6.3 N_2^+ X, A and B states

The N_2^+ 1N band system results from simultaneous ionisation and excitation of the N_2X state via electron collisions to the N_2^+ B state followed by radiative de-excitation to the ion ground state. During non-sunlit conditions, the emission is proportional to the ionisation rate.

The N_2^+ ion ground state is an efficient scatterer of solar photons. The molecules in the X state that are sunlit above the shadow height are excited to the N_2^+ A and N_2^+ B states through a resonance process, resulting in increased brightness in the Meinel and the 1N band systems respectively. Following Broadfoot [1967] and Degen [1981], we consider excitation and de-excitation of vibrational levels of N_2^+ X, A, B states to

determine the brightness of the 1N bands in sunlit aurora in different conditions.

The time dependent population of the vibrational levels in the X, A and B states is described the same way as in the previous section by

$$\frac{dn}{dt} = Production - Losses \tag{6.23}$$

Sources of the N_2^+ X state include direct excitation from the N_2 X state via electron impact and radiative transitions from the N_2^+ A and B states. Sources for the A and B states also include direct excitation via electron impact from the N_2 X state. Another source for the excited N_2^+ A and B states is the resonance absorption of solar photons from the N_2^+ X ground state vibrational levels.

Loss factors for the N_2^+ X state are resonance absorption of solar photons into the higher states and for the N_2^+ A and B states the loss factors are prompt emissions. All states are affected by ion chemical losses through collisions. This ion life time depends on the relevant reaction rate and is height dependent.

The ion chemistry model treats N_2^+ as a single species and produces time dependent height profiles of the N_2 molecular concentration using the relevant electron impact excitation cross sections and input primary electron spectra. We assume only local production of N_2^+. We also do not take into account ionisation by photoelectrons or excitation from N_2^+ X to A and B by soft electrons [Degen, 1981].

6.3.1 Direct Excitation

The production of ions in different vibrational levels v' of N_2^+ X, A, B states is given by

$$\eta^d_{v'''\rightarrow v'',v'} = \int_E n_{v'''}\ f(E)\sigma^e(E)\ \varepsilon\ (X,B,A)\ q_{(v'''\rightarrow v'',v')}\ dE \tag{6.24}$$

where $\eta^d_{(v'''\rightarrow v'',v')}$ is the production rate of N_2^+ into level v' or v'' from a particular v''', $n_{v'''}$ is the concentration of ground state N_2 molecules, $f(E)$ is the incident electron

differential energy flux, $\sigma^e(E)$ is the total electron ionising excitation cross section of the N_2 ground state to all three ion states and $q_{v'''\rightarrow v'',v'}$ is the Franck-Condon factor for each level. We use ε (X, A, B) to describe the ionisation efficiency, given by the branching ratios between the production rate of X, A and B states, which are 0.50, 0.39, 0.11 respectively (Rees, 1989). The standard prime convention is used to describe vibrational levels. v''' relates to the N_2 X vibrational levels, v'' relates to the N_2^+ X vibrational levels and v' relates to the excited N_2^+ A, B vibrational levels. Franck-Condon factors are taken from Gilmore et al. [1992], listed in Table 6.3 for three N_2^+ B vibrational levels from the $v''' = 0$ vibrational level of N_2 X. Franck-Condon factors from Lofthus et al. [1977] are also listed for reference. At vibrational temperatures above 1000 K, higher vibrational levels need to be considered.

If the total ion production rate is known, e.g. from the ion chemistry model, Eq. 6.24 can be rewritten as

$$\eta^d_{(v'''\rightarrow v'',v')} = \varepsilon\ (X, B, A)\ q_{(v'''\rightarrow v'',v')}\ \eta^d_{N_2^+} \tag{6.25}$$

where $\eta^d_{N_2^+}$ is the total production rate of N_2^+.

v', v'''	0,0	1,0	2,0
[a]N_2 X-N_2^+ B	8.83-1	1.14-1	2.31-3
[b]N_2 X-N_2^+ B	8.864-1	1.112-1	2.335-3

Table 6.3: *Franck-Condon factors from Gilmore et al. [1992][a] and Lofthus et al. [1977][b]*

6.3.2 Resonance absorption of solar photons

When N_2^+ molecules in the X-state are sunlit, resonance absorption of solar photons results in excitation rate η^s into the A and B ion states.

$$\eta^s_{v''\rightarrow v'} = \pi F_{v''\rightarrow v'}\ f_{v''\rightarrow v'}\ \frac{\pi e^2}{m_e c}\ \frac{1}{4\pi\epsilon_0}\ \frac{\lambda^2}{c}\ n_{v''} \tag{6.26}$$

where $\pi F_{v''\to v'}$ is the solar flux per unit wavelength [photons $m^{-2}s^{-1}m^{-1}$], $f_{v''\to v'}$ is the absorption oscillator strength, $\frac{\pi e^2}{m_e c}\ \frac{1}{4\pi\epsilon_0}\ \frac{\lambda^2}{c}$ [m^3] is the photon absorption cross section multiplied by the line width. The factor $\frac{\lambda^2}{c}$ is for conversion from spectral flux per unit frequency to flux per unit wavelength. $n_{v''}$ is the concentration of N_2^+ in the X state vibrational level v''.

6.3.3 Emission processes

Radiative transitions to the N_2^+ X state are loss processes for the A and B states. The emission rate in a particular band is given by the Einstein coefficient as follows

$$\eta_{v'\to v''} = A_{v'\to v''} n_{v'}. \tag{6.27}$$

Total radiative loss for a given v' state is

$$\eta_{v'} = \Sigma_{v''} A_{v'\to v''} n_{v'} \tag{6.28}$$

with the emission in each particular band given by the branching ratio

$$b_{v'\to v''} = \frac{\eta_{v'\to v''}}{\eta_{v'}} = \frac{A_{v'\to v''}}{\sum_{v''} A_{v'\to v''}}. \tag{6.29}$$

Einstein coefficients are available from several sources. We have used the most recent values of Gilmore et al. [1992]. These are given in Table 6.4 along with those from Lofthus et al. [1977] and Vallance Jones [1974] for comparison.

6.3.4 Ion lifetime

The ion lifetime is the time before collisional deactivation and depends therefore on the atmosperic density. Figure 6.4 shows the ion lifetime resulting from the ion chemistry model using input from MSIS atmospheric model for a typical atmosphere at 07:00 UT in January over Svalbard with Ap index of 7 and monthly average solar radio flux F10.7 of 77. However, there is some uncertainty in the MSIS model because it is only a statistical average model, which is not particularly good at high latitudes due to plasma

v', v''	0,1	1,2	2,3
$^a A_{v'v''}$	3.71+6	4.28+6	3.47+6
$^b A_{v'v''}$	3.48+6	3.87+6	3.03+6
$^c A_{v'v''}$	3.35+6	3.81+6	3.13+6
$^a \sum_{v''} A_{v'v''}$	16.05+6	16.11+6	15.91+6
$^b \sum_{v''} A_{v'v''}$	14.05+6	13.82+6	13.34+6
$^c \sum_{v''} A_{v'v''}$	15.15+6	15.97+6	16.64+6

Table 6.4: *Einstein coefficients from Gilmore et al. [1992][a], Lofthus et al. [1977][b], and Vallance Jones [1974][c]*

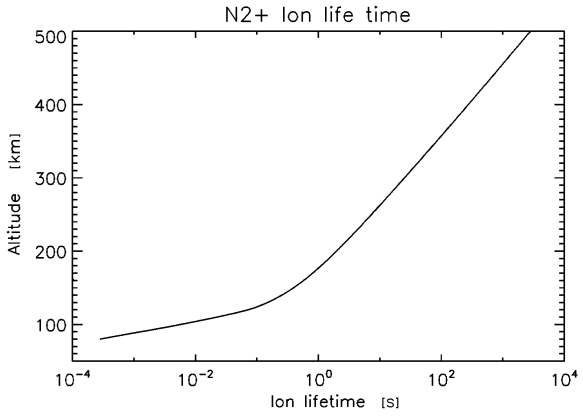

Figure 6.4: *Ion lifetime derived from the ion chemistry model using the MSIS atmospheric thermal model for a typical atmosphere at 07:00 UT in January over Svalbard with Ap index of 7 and monthly average solar radio flux F10.7 of 77.*

convection and the highly variable nature of the ionosphere during auroral precipitation. Moreover, during the statistical study in Chapter 7, the MSIS model has only been taken for one instance in time in the analysis.

6.3.5 Steady state solutions

Equation 6.23 can be solved in a time dependent manner, which is outside the scope of this chapter. Setting $\frac{dn}{dt}$ to zero we perform calculations for steady state conditions for each vibrational level of the N_2^+ A, B and X states, as described in Eqs. 6.30, 6.31 and 6.32 respectively, where the gain and loss terms are as previously described.

$$\sum_{v'''} \varepsilon(A) q_{(v'''\rightarrow v')} \eta^d_{N_2^+} + \sum_{v''} \pi F_{v''\rightarrow v'}\ f_{v''\rightarrow v'}\ \frac{\pi e^2}{m_e c}\ \frac{1}{4\pi\epsilon_0}\ \frac{\lambda^2}{c}\ n_{v''} = \sum_{v''} A_{v'\rightarrow v''} n_{v'} + \frac{n_{v'}}{\tau} \tag{6.30}$$

$$\sum_{v'''} \varepsilon(B) q_{(v'''\rightarrow v')} \eta^d_{N_2^+} + \sum_{v''} \pi F_{v''\rightarrow v'}\ f_{v''\rightarrow v'}\ \frac{\pi e^2}{m_e c}\ \frac{1}{4\pi\epsilon_0}\ \frac{\lambda^2}{c}\ n_{v''} = \sum_{v''} A_{v'\rightarrow v''} n_{v'} + \frac{n_{v'}}{\tau} \tag{6.31}$$

$$\sum_{v'''} \varepsilon(X) q_{(v'''\rightarrow v'')} \eta^d_{N_2^+} + \sum_{v'} A_{v'\rightarrow v''} n_{v'} = \sum_{v'} \pi F_{v''\rightarrow v'}\ f_{v''\rightarrow v'}\ \frac{\pi e^2}{m_e c}\ \frac{1}{4\pi\epsilon_0}\ \frac{\lambda^2}{c}\ n_{v''} + \frac{n_{v''}}{\tau} \tag{6.32}$$

These balance equations can be regrouped as a linear system of equations as in the previous section in the form of

$$\Sigma_j \mathbf{M}_{ij} n_j = \eta_i^d \tag{6.33}$$

where $\mathbf{M}_{ij}$ is the matrix characterising production and loss processes, n_j is the concentration of each particular electronic-vibration level and η_i^d is the direct production rate of each electronic-vibration state due to auroral precipitation. The indices of the matrix are shown in Tables 6.5 and 6.6.

The level populations can then be solved by matrix inversion

$$n_j = \mathbf{M}_{ij}^{-1} \eta_i^d \tag{6.34}$$

NB3×	NB2×	NB1×	NB0×	NA5×	NA4×	NA3×	NA2×	NA1×	NA0×
$-A^{1N}_{(3-5)}$	$-A^{1N}_{(2-5)}$	$-A^{1N}_{(1-5)}$	$-A^{1N}_{(0-5)}$	$-A^{M}_{(5-5)}$	$-A^{M}_{(4-5)}$	$-A^{M}_{(3-5)}$	$-A^{M}_{(2-5)}$	$-A^{M}_{(1-5)}$	$-A^{M}_{(0-5)}$
$-A^{1N}_{(3-4)}$	$-A^{1N}_{(2-4)}$	$-A^{1N}_{(1-4)}$	$-A^{1N}_{(0-4)}$	$-A^{M}_{(5-4)}$	$-A^{M}_{(4-4)}$	$-A^{M}_{(3-4)}$	$-A^{M}_{(2-4)}$	$-A^{M}_{(1-4)}$	$-A^{M}_{(0-4)}$
$-A^{1N}_{(3-3)}$	$-A^{1N}_{(2-3)}$	$-A^{1N}_{(1-3)}$	$-A^{1N}_{(0-3)}$	$-A^{M}_{(5-3)}$	$-A^{M}_{(4-3)}$	$-A^{M}_{(3-3)}$	$-A^{M}_{(2-3)}$	$-A^{M}_{(1-3)}$	$-A^{M}_{(0-3)}$
$-A^{1N}_{(3-2)}$	$-A^{1N}_{(2-2)}$	$-A^{1N}_{(1-2)}$	$-A^{1N}_{(0-2)}$	$-A^{M}_{(5-2)}$	$-A^{M}_{(4-2)}$	$-A^{M}_{(3-2)}$	$-A^{M}_{(2-2)}$	$-A^{M}_{(1-2)}$	$-A^{M}_{(0-2)}$
$-A^{1N}_{(3-1)}$	$-A^{1N}_{(2-1)}$	$-A^{1N}_{(1-1)}$	$-A^{1N}_{(0-1)}$	$-A^{M}_{(5-1)}$	$-A^{M}_{(4-1)}$	$-A^{M}_{(3-1)}$	$-A^{M}_{(2-1)}$	$-A^{M}_{(1-1)}$	$-A^{M}_{(0-1)}$
$-A^{1N}_{(3-0)}$	$-A^{1N}_{(2-0)}$	$-A^{1N}_{(1-0)}$	$-A^{1N}_{(0-0)}$	$-A^{M}_{(5-0)}$	$-A^{M}_{(4-0)}$	$-A^{M}_{(3-0)}$	$-A^{M}_{(2-0)}$	$-A^{M}_{(1-0)}$	$-A^{M}_{(0-0)}$
$\sum_{v''} A_{(3-v'')}$	0	0	0	0	0	0	0	0	0
0	$\sum_{v''} A_{(2-v'')}$	0	0	0	0	0	0	0	0
0	0	$\sum_{v''} A_{(1-v'')}$	0	0	0	0	0	0	0
0	0	0	$\sum_{v''} A_{(0-v'')}$	0	0	0	0	0	0
0	0	0	0	$\sum_{v''} A_{(5-v'')}$	0	0	0	0	0
0	0	0	0	0	$\sum_{v''} A_{(4-v'')}$	0	0	0	0
0	0	0	0	0	0	$\sum_{v''} A_{(3-v'')}$	0	0	0
0	0	0	0	0	0	0	$\sum_{v''} A_{(2-v'')}$	0	0
0	0	0	0	0	0	0	0	$\sum_{v''} A_{(1-v'')}$	0
0	0	0	0	0	0	0	0	0	$\sum_{v''} A_{(0-v'')}$

Table 6.5: *Matrix coefficients of vibrational level populations of N_2^+ in order of X(5,4,3,2,1,0), B(3,2,1,0) and A(5,4,3,2,1,0).*

NX5×	NX4×	NX3×	NX2×	NX1×	NX0×	= constant matrix
$c_2[I_5+J_5]+\frac{1}{\tau}$	0	0	0	0	0	$\varepsilon_X \sum_{v'''}^{directtoX}[q_{(v'''-5)}N(N2)_{v'''}]$
0	$c_2[I_4+J_4]+\frac{1}{\tau}$	0	0	0	0	$\varepsilon_X \sum_{v'''}^{directtoX}[q_{(v'''-4)}N(N2)_{v'''}]$
0	0	$c_2[I_3+J_3]+\frac{1}{\tau}$	0	0	0	$\varepsilon_X \sum_{v'''}^{directtoX}[q_{(v'''-3)}N(N2)_{v'''}]$
0	0	0	$c_2[I_2+J_2]+\frac{1}{\tau}$	0	0	$\varepsilon_X \sum_{v'''}^{directtoX}[q_{(v'''-2)}N(N2)_{v'''}]$
0	0	0	0	$c_2[I_1+J_1]+\frac{1}{\tau}$	0	$\varepsilon_X \sum_{v'''}^{directtoX}[q_{(v'''-1)}N(N2)_{v'''}]$
0	0	0	0	0	$c_2[I_0+J_0]+\frac{1}{\tau}$	$\varepsilon_X \sum_{v'''}^{directtoX}[q_{(v'''-0)}N(N2)_{v'''}]$
$-c_2\pi F^B_{(3-5)}f^B_{(3-5)}$	$-c_2\pi F^B_{(3-4)}f^B_{(3-4)}$	$-c_2\pi F^B_{(3-3)}f^B_{(3-3)}$	$-c_2\pi F^B_{(3-2)}f^B_{(3-2)}$	$-c_2\pi F^B_{(3-1)}f^B_{(3-1)}$	$-c_2\pi F^B_{(3-0)}f^B_{(3-0)}$	$\varepsilon_B \sum_{v'''}^{directtoB}[q_{(v'''-3)}N(N2)_{v'''}]$
$-c_2\pi F^B_{(2-5)}f^B_{(2-5)}$	$-c_2\pi F^B_{(2-4)}f^B_{(2-4)}$	$-c_2\pi F^B_{(2-3)}f^B_{(2-3)}$	$-c_2\pi F^B_{(2-2)}f^B_{(2-2)}$	$-c_2\pi F^B_{(2-1)}f^B_{(2-1)}$	$-c_2\pi F^B_{(2-0)}f^B_{(2-0)}$	$\varepsilon_B \sum_{v'''}^{directtoB}[q_{(v'''-2)}N(N2)_{v'''}]$
$-c_2\pi F^B_{(1-5)}f^B_{(1-5)}$	$-c_2\pi F^B_{(1-4)}f^B_{(1-4)}$	$-c_2\pi F^B_{(1-3)}f^B_{(1-3)}$	$-c_2\pi F^B_{(1-2)}f^B_{(1-2)}$	$-c_2\pi F^B_{(1-1)}f^B_{(1-1)}$	$-c_2\pi F^B_{(1-0)}f^B_{(1-0)}$	$\varepsilon_B \sum_{v'''}^{directtoB}[q_{(v'''-1)}N(N2)_{v'''}]$
$-c_2\pi F^B_{(0-5)}f^B_{(0-5)}$	$-c_2\pi F^B_{(0-4)}f^B_{(0-4)}$	$-c_2\pi F^B_{(0-3)}f^B_{(0-3)}$	$-c_2\pi F^B_{(0-2)}f^B_{(0-2)}$	$-c_2\pi F^B_{(0-1)}f^B_{(0-1)}$	$-c_2\pi F^B_{(0-0)}f^B_{(0-0)}$	$\varepsilon_B \sum_{v'''}^{directtoB}[q_{(v'''-0)}N(N2)_{v'''}]$
$-c_2\pi F^A_{(5-5)}f^A_{(5-5)}$	$-c_2\pi F^A_{(5-4)}f^A_{(5-4)}$	$-c_2\pi F^A_{(5-3)}f^A_{(5-3)}$	$-c_2\pi F^A_{(5-2)}f^A_{(5-2)}$	$-c_2\pi F^A_{(5-1)}f^A_{(5-1)}$	$-c_2\pi F^A_{(5-0)}f^A_{(5-0)}$	$\varepsilon_A \sum_{v'''}^{directtoA}[q_{(v'''-5)}N(N2)_{v'''}]$
$-c_2\pi F^A_{(4-5)}f^A_{(4-5)}$	$-c_2\pi F^A_{(4-4)}f^A_{(4-4)}$	$-c_2\pi F^A_{(4-3)}f^A_{(4-3)}$	$-c_2\pi F^A_{(4-2)}f^A_{(4-2)}$	$-c_2\pi F^A_{(4-1)}f^A_{(4-1)}$	$-c_2\pi F^A_{(4-0)}f^A_{(4-0)}$	$\varepsilon_A \sum_{v'''}^{directtoA}[q_{(v'''-4)}N(N2)_{v'''}]$
$-c_2\pi F^A_{(3-5)}f^A_{(3-5)}$	$-c_2\pi F^A_{(3-4)}f^A_{(3-4)}$	$-c_2\pi F^A_{(3-3)}f^A_{(3-3)}$	$-c_2\pi F^A_{(3-2)}f^A_{(3-2)}$	$-c_2\pi F^A_{(3-1)}f^A_{(3-1)}$	$-c_2\pi F^A_{(3-0)}f^A_{(3-0)}$	$\varepsilon_A \sum_{v'''}^{directtoA}[q_{(v'''-3)}N(N2)_{v'''}]$
$-c_2\pi F^A_{(2-5)}f^A_{(2-5)}$	$-c_2\pi F^A_{(2-4)}f^A_{(2-4)}$	$-c_2\pi F^A_{(2-3)}f^A_{(2-3)}$	$-c_2\pi F^A_{(2-2)}f^A_{(2-2)}$	$-c_2\pi F^A_{(2-1)}f^A_{(2-1)}$	$-c_2\pi F^A_{(2-0)}f^A_{(2-0)}$	$\varepsilon_A \sum_{v'''}^{directtoA}[q_{(v'''-2)}N(N2)_{v'''}]$
$-c_2\pi F^A_{(1-5)}f^A_{(1-5)}$	$-c_2\pi F^A_{(1-4)}f^A_{(1-4)}$	$-c_2\pi F^A_{(1-3)}f^A_{(1-3)}$	$-c_2\pi F^A_{(1-2)}f^A_{(1-2)}$	$-c_2\pi F^A_{(1-1)}f^A_{(1-1)}$	$-c_2\pi F^A_{(1-0)}f^A_{(1-0)}$	$\varepsilon_A \sum_{v'''}^{directtoA}[q_{(v'''-1)}N(N2)_{v'''}]$
$-c_2\pi F^A_{(0-5)}f^A_{(0-5)}$	$-c_2\pi F^A_{(0-4)}f^A_{(0-4)}$	$-c_2\pi F^A_{(0-3)}f^A_{(0-3)}$	$-c_2\pi F^A_{(0-2)}f^A_{(0-2)}$	$-c_2\pi F^A_{(0-1)}f^A_{(0-1)}$	$-c_2\pi F^A_{(0-0)}f^A_{(0-0)}$	$\varepsilon_A \sum_{v'''}^{directtoA}[q_{(v'''-0)}N(N2)_{v'''}]$

Table 6.6: *Matrix coefficients of vibrational level populations of N_2^+ in order of X(5,4,3,2,1,0), B(3,2,1,0) and A(5,4,3,2,1,0) where* $c_2 = \frac{\pi e^2}{mc}$, $I_n = \sum_{v'}^{B} \pi F^B_{(v'-n)} f^B_{(v'-n)}$ *and* $J_n = \sum_{v'}^{A} \pi F^A_{(v'-n)} f^A_{(v'-n)}$

to provide equilibrium concentrations of all considered electronic-vibration states. Absolute values of the densities of the states are proportional to the total ionisation rate as the system is considered linear, while the ratios of densities are constant and are given by the molecular constants, solar flux and ion lifetime.

The steady state equilibrium density distribution within the N_2^+ X, A and B states are plotted in Fig. 6.5(a),(b) and (c) as a function of ion lifetime assuming the ionosphere is sunlit. The percentage population of N_2^+ in the X state is plotted for vibrational levels $v'' = 0 - 5$, in the A state for vibrational levels $v' = 0 - 5$ and in the B state for vibrational levels $v' = 0 - 3$. At high altitudes the long ion lifetime allows more scattering to take place and is therefore dominated by resonance absorption, whereas at low altitudes the short ion lifetime enforces a distribution that is dominated by direct excitation. The vibrational distribution that follows from the latter depends on the vibrational temperature T_{vib} of the N_2 X state. This is indicated in the figure by the expansion of the coloured lines in the range of $100 - 10000$ K in steps of 1000 K. The values for $T_{vib} = 1000$ K are highlighted in black, and are close to those for $T_{vib} = 100$ K.

Although about half of the ions are produced in the A and B states, they immediately radiate into the X state so that at any given time nearly all the ions lie in the X state, from which resonance absorption takes place. The fraction $p_{v'}$ of A and B state vibrational level populations with respect to the total N_2^+ concentration can be found from the relation

$$p_{v'} = \frac{n_{v'(A,B)}}{\sum_{v',v''} n_{v',v''}}. \tag{6.35}$$

Figure 6.6 describes how this fraction varies with ion lifetime. As expected, at steady state and at longer ion lifetimes the density builds up in the X state so that only a very small fraction of the total density is maintained in the A and B states via direct excitation. At long ion lifetimes the B state contributes only a fraction of 10^{-6} and the A state a fraction of 10^{-4} to the total ion content.

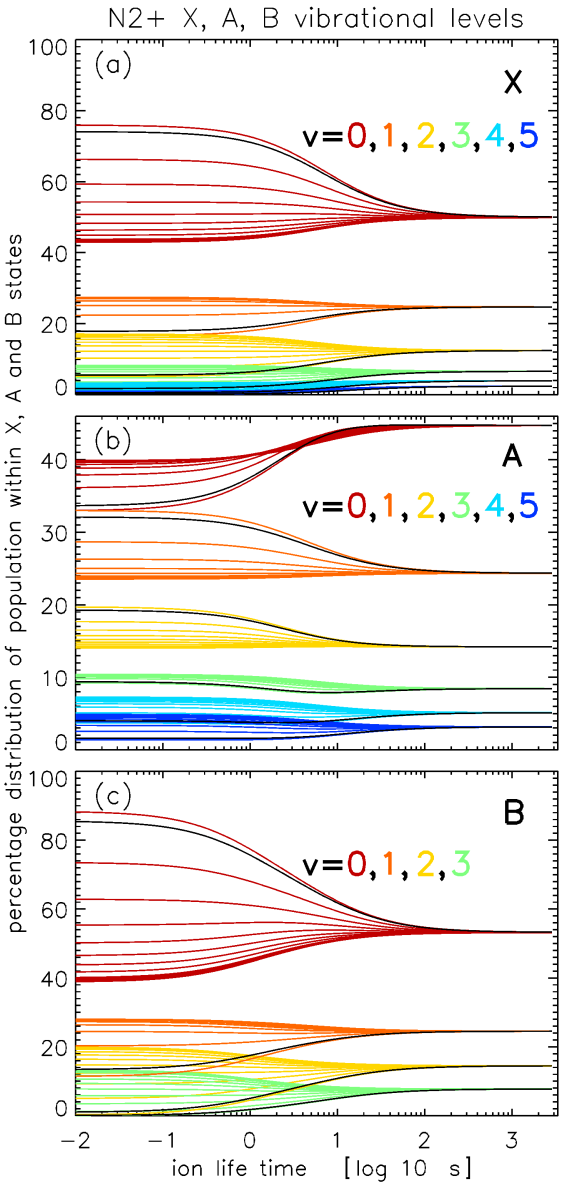

Figure 6.5: *Vibrational distribution of ion states as a function of ion chemical lifetime, for* $T_{vib} = 100 - 10000$ *K in steps of 1000 K (*$T_{vib} = 1000$ *is highlighted in black and is very close to* $T_{vib} = 100$*): (a)* $v'' = 0 - 5$ *for* N_2^+ *X, (b)* $v'' = 0 - 5$ *for* N_2^+ *A and (c)* $v'' = 0 - 3$ *for* N_2^+ *B.*

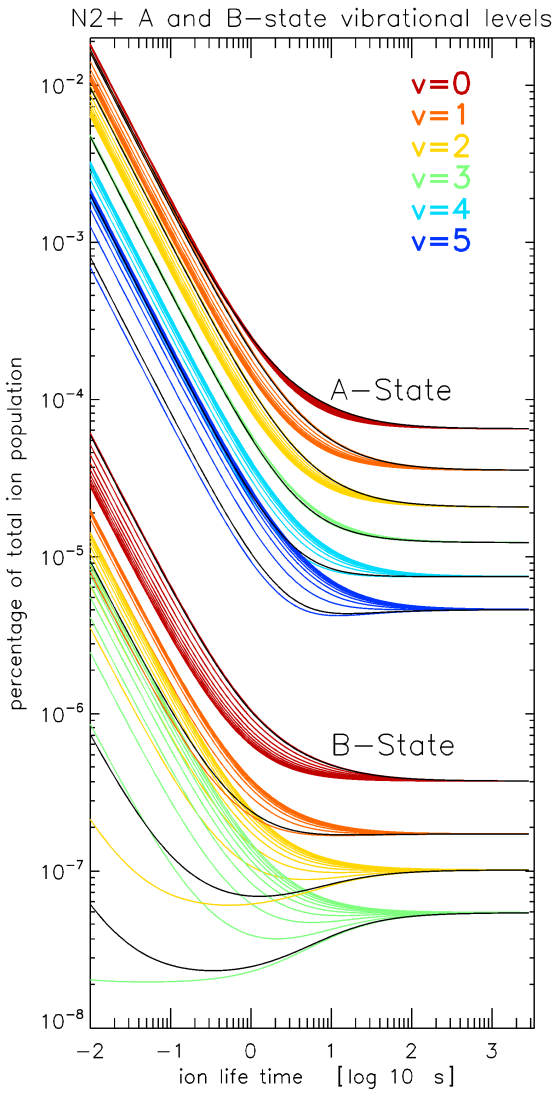

Figure 6.6: *Vibrational distribution of ion states in levels* $v' = 0 - 5$ *of the* N_2^+ *A state and vibrational levels* $v' = 0 - 3$ *of the* N_2^+ *B state with respect to the total population in all X, A and B states as a function of ion chemical lifetime.* $T_{vib} = 100 - 10000$ *K in steps of 1000 K with* $T_{vib} = 1000$ *highlighted in black.*

Published as: O. Jokiaho, B. S. Lanchester, N. Ivchenko – *"Resonance scattering by auroral N_2^+: steady state theory and observations from Svalbard,"* Annales Geophys., submitted 2009.

Chapter 7

Resonance scattering by auroral N_2^+: steady state theory and observations from Svalbard.

7.1 Introduction

Emissions from the nitrogen molecule are of great importance in auroral studies. Firstly, they are used as diagnostics for the total energy flux, since the brightness of these emissions is only weakly dependent on the characteristic energy. Secondly, spectral measurements of N_2^+ bands can be used to determine the rotational temperature. Thermal equilibrium of atmospheric constituents allows us to assume that the rotational temperature is a measure of the atmospheric neutral temperature of the emitting species. Hence it is possible to infer the height of the auroral excitation, from which is estimated the characteristic energy.

The auroral N_2^+ 1N band system in the UV (from $B^2\Sigma_u^+$ to $X^2\Sigma_g^+$) is caused by electron impact ionisation and excitation of the N_2 molecules. However, when N_2^+ ions are illuminated by sunlight above the shadow height at high latitudes, the 1N band system will scatter and fluoresce, enhancing brightness and leading to an increase in vibrational and rotational temperatures. Different bands are affected in different ways, so that the ratios of emissions will vary with shadow height. Therefore during sunlit or partially sunlit conditions the measured values of emission intensities (and rotational temperatures) will lead to uncertainties in the characteristic electron energy and energy flux. The average energy from rotational spectra can be underestimated due to the contribution from highly developed sunlit spectra. Similarly, the flux can be overestimated in a

simple photometric measurement when the brightness is increased due to the scattered contribution.

Abnormally bright N_2^+ was first observed by Störmer [1955] in the early 1910s. Triangulation indicated the rays were located above 1000 km. The observation that sunlit rays occur between a year before and three years after sunspot maximum can be related to the significant increase of the exospheric temperature from 1000 K to 2000 K, and expansion of the upper atmosphere at the maximum of solar UV activity. Sunlit measurements have usually been recorded away from the magnetic zenith [Broadfoot, 1967, Vallance Jones and Hunten, 1960]. The latter reported unusually high rotational and vibrational temperatures of 2200 K during the 1958 solar maximum. An historical account of resonance scattering from N_2^+ can be found in Hunten [2003].

The theoretical foundation for resonance scattering of N_2^+ ions was set up by Bates [1949]. Broadfoot [1967] later demonstrated how the vibrational distribution is strongly affected by resonance scattering and highlighted the method of using the relative intensities and populations of excited states to give an estimate of the two excitation sources. Ionisation from photoionisation is indistinguishable from electron impact because the ionisation efficiency is very similar; the former dominates in twilight and daytime non-auroral conditions, and the latter in sunlit and non-sunlit aurora. More enhanced vibrational development in twilight spectra in comparison to sunlit aurora is also reported. Broadfoot modelled steady state populations for all important vibrational levels of the N_2^+ $X^2\Sigma_g^+$, $A^2\Pi_u$ and $B^2\Sigma_u^+$ as a function of ion lifetime and reported a 40% contribution of resonance scattering to N_2^+ 1N bands.

Degen [1981] used new cross sections in the model of Broadfoot [1967] which raises ion lifetimes in sunlit aurora by an order of magnitude. He found that resonance scattering contributed 56% of the 1N intensities, pointing out the relative population increase with increasing vibrational level v'. Degen also introduced low energy electron induced fluorescence analogous to solar induced fluorescence to explain vibrational enhancement of the 1N band in the great type-A aurora of 1958 in non-sunlit conditions.

The model was revisited by Degen [1987] when he modified the N_2^+ 1N (0,0) rotational band structure by varying the ion life time and rotational temperature. The results were compared favourably with sunlit auroral data of Hunten et al. [1959].

The characteristic intensity minimum just below the shadow height of aurora that is partly sunlit has long been observed with scanning photometers. N_2^+ 1N (0,1) height profiles of volume emission rate were studied by Lanchester et al. [1987] over Svalbard. In the morning sector these profiles had the characteristic double hump feature due to the contribution from resonance scattering. In that work the resonance scattering contribution was subtracted in order to estimate the energy of precipitation from brightness ratios.

Romick et al. [1999] provided the first space borne spectrographic observation of auroral emissions above 600 km from the N_2^+ 1N and M band systems, reporting emissions up to 900 km over the northern polar cap close to magnetic noon. No other significant optical emissions were detected above 450 km, suggesting the source was resonance scattering of the N_2^+ ions in the presence of ion upflows. They measured up to a 40% contribution in the 1N band system intensity above the shadow height with $K_p = 3$ and a 4% contribution with $K_p = 1$.

Remick et al. [2001] conducted simultaneous observations of N_2^+ 1N (0,1) with N_2^+ M (0,0) at Poker Flat, Alaska over two seasons between 1995 and 1997. Emission rates of the two bands should be in strict proportion over a wide energy range, which was not found. The lack of proportionality was explained by the increase in the 1N band system intensity by resonance scattering. They concluded that there exists a short duration episodic acceleration mechanism in the presence of auroral arcs that lifts ions into the sunlit region of the ionosphere.

The present work sets out to quantify the effect of sunlit conditions on zenith measurements under a steady state. It follows work of Jokiaho et al. [2008], which used the N_2^+ 1N (0,2) band to determine the rotational temperature and thus estimate the energy of precipitation, in conjunction with the EISCAT Svalbard Radar. In the present work,

we make a statistical study of spectral measurements of three N_2^+ 1N bands (1,0), (1,2) and (2,3), and one N_2 2P band (0,3). We investigate the brightness ratios of the N_2^+ bands and their ratio to the N_2 band, since in resonance scattered auroral events the relationship between them can be used as an indicator of the scattered contribution. We also study the relationship of all emissions and their ratios to rotational temperatures. The theoretical basis of the study is provided in Section 3, giving a method of quantifying the scattering enhancement and the effect on rotational temperatures, as well as the possible effect of ion upflows.

7.2 Experimental Details and Analysis

We report a statistical study of night-time, twilight and daytime (cusp) aurora at the solar minimum from the magnetic zenith between 17 January and 14 March 2007 at Adventdalen. The experiment used the HiTIES equipped with a water cooled Andor iXon EMCCD camera and a five panel interference filter mosaic seen in Fig. 7.1, which was designed to measure the effect of resonance scattering of solar photons in aurora by N_2^+ molecules. Height integrated spectral profiles were obtained for the study with a temporal resolution of 10-30 s.

Spectral bands of interest are the N_2^+ 1N and N_2 2P band systems that both lie in the near UV region. The mosaic selects orders containing the bands of: N_2^+1N (0,1) at 427.8 nm, (1,2) at 423.6 nm, (2,3) at 419.9 nm and N_2 2P (0,3) at 405.8 nm. Some atomic lines are also seen, namely N^+ at 423.7 nm, O^+ doublet centred at 419 nm, contaminant mercury HgI at 404.7 nm, all of which are outside the bands of interest. The Hα and Hβ lines are excited in proton aurora [Galand et al., 2004] which is one of the science objectives of the SIF instrument [Lanchester et al., 2003]. In this study of resonance scattering we do not analyse the hydrogen emissions.

Wavelength calibration of the instrument was performed using data from a period with a bright aurora in the field of view. The observed position of identifiable spectral features were related to their tabulated wavelengths. The focusing was optimised for

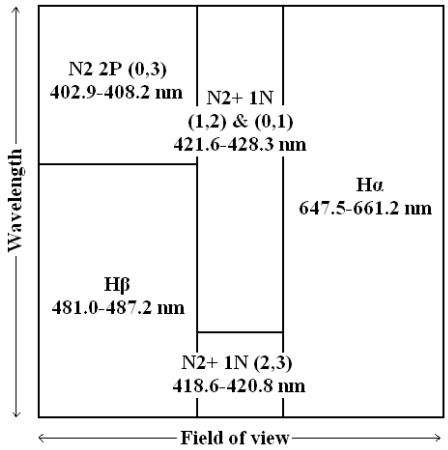

Figure 7.1: *The HiTIES spectrograph is equipped with a* 50×50 *mm square mosaic consisting of five interference filters. The 8° field of view is on the horizontal axis and wavelength on the vertical axis.*

best wavelength resolution in the R-branch rotational lines of the N_2^+ 1N (0,1). A flat lamp was used for intensity calibration of the data.

Figure 7.2 shows a typical auroral spectra used in this study. The prominent emissions in order of increasing wavelength are HgI, N_2 2P (0,3), N_2^+ 1N (2,3), (1,2) and (0,1). The presence of HgI indicates reflection of artificial lighting from the cloud cover above and is overlaid on auroral data for comparison. The wavelength intervals used for deriving the brightness of the bands are highlighted in colour.

The total band intensities were calculated by integrating the observed spectral brightnesses over wavelength intervals of $427.9 - 424.5$ nm for the N_2^+ 1N (0,1), $423.8 - 422.3$ nm for the N_2^+ 1N (1,2), $419.5 - 420.0$ nm for the N_2^+ 1N (2,3) and $405.6 - 406.0$ nm for the N_2 2P (0,3). The background levels are different for each of the bands and these were measured by taking an average of the spectral brightness outside the integrated region. The background brightness of N_2^+ 1N (0,1) and (1,2) was estimated from the longer wavelength side of the N_2^+ 1N (0,1) band head. The background for N_2^+ 1N (2,3) is determined from the region $418.5 - 419.5$ nm. The atomic oxygen lines are very weak

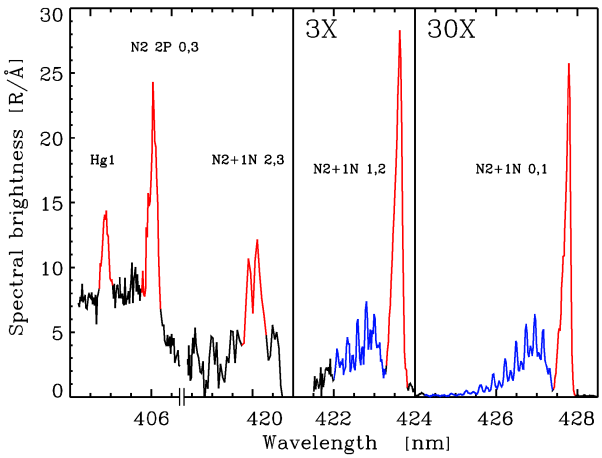

Figure 7.2: *Sample data from the HiTIES spectrograph using a 5-band mosaic filter (excluding the Hα and Hβ lines). The highlighted spectral features here correspond in increasing wavelength to HgI (red) overlaid from cloudy data, N_2 2P (0,3) (red), N_2^+ 1N (2,3) (red), N_2^+ 1N R of (1,2) (blue) P of (1,2) (red) and N_2^+ 1N R of (0,1) (blue) and P of (0,1) (red).*

and allow a reasonable noise level to be measured. The longer wavelength side of the band head cannot be used as the instrument response falls off rapidly due to optical vignetting at the edge of the mosaic. The background for N_2 2P (0,3) is measured between the HgI and the N_2 2P (0,3) features.

Low brightness and increased experimental uncertainty is associated with decreased instrument response in the UV. Spectral features other than N_2^+ 1N (0,1) and (1,2) are subject to greater uncertainties so that the band structure is difficult to resolve. The N_2 2P (0,3) and N_2^+ 1N (2,3) band typically account for only a few percent at most of the N_2^+ 1N (0,1) intensity and are situated further into the UV region. N_2 2P is a Π-Π triplet transition and forms one distinct band head which makes it easier to detect. The low flat lamp spectral brightness in the near UV also added some uncertainty in the measurements.

The rotational temperatures of the N_2^+ were derived using the χ^2 statistic [Jokiaho et al., 2008] with the N_2^+ 1N (0,1) band profiles. The standard deviation in height in-

tegrated rotational temperatures depends on the excitation conditions. It also depends on the temperature itself as the intensity distribution is more dynamic at lower temperatures than at higher temperatures. The overlapping of N_2^+ bands also needs to be considered at high rotational temperatures. The rotational band profiles were acquired by subtracting the correct level of background output from the statistical process.

7.3 Theoretical Approach

7.3.1 Volume emission rates

Following from Eq. 6.25 the volume emission rate from vibrational level v' in the A or B state to vibrational level v'' in the X state from direct electron impact excitation is given by

$$I^d_{v'\to v''} = \sum_{v'''} \eta^d_{v'''\to v'} b_{v'\to v''} \ \ [\mathrm{ph/m^3/s}] \tag{7.1}$$

The production rate $\eta^d_{v'''\to v'}$ is summed over the N_2 X state levels. However, this has an insignificant effect for $T_{vib} < 1000$ K as the great majority of ions lie on the zeroth vibrational level.

Using Eq. 6.26 the volume emission rate from vibrational level v' in the A or B state to vibrational level v'' in the X state due to resonance absorption of solar photons is given by

$$I^s_{v'\to v''} = (\sum_{v''*} \eta^s_{v''*\to v'}) b_{v'\to v''} \ \ [\mathrm{ph/m^3/s}] \tag{7.2}$$

where the summation in this case is over all vibrational levels $v''*$ of the N_2^+ X state. The production rate $\eta^s_{v''*\to v'}$ strongly depends on the distribution of vibrational levels in the N_2^+ X state and consequently greatly affects the vibrational distribution in the excited states. The total emission rate is given by

$$I^{total}_{v'\to v''} = n_{N_2^+} p_{v'} A_{v'\to v''} \ \ [\mathrm{ph/m^3/s}] \tag{7.3}$$

where $n_{N_2^+}$ is the total ion density.

The ion chemistry model is run for a constant energy flux of 1 mW/m^2 and for different monoenergetic electron energy distributions modelled by a Gaussian of 10% width in the range 100 eV to 10 keV to calculate the ion production rate and density of N_2^+ as a function of time and height.

Volume emission rate profiles were obtained for direct excitation of 30 s to reach steady state at heights up to 300 km, using Eq. 7.1, and for resonance scattered emissions with a sunlit ionosphere, using Eq. 7.2. The resulting profiles are shown in Fig. 7.3 for three monoenergetic primary electron spectra of 100 eV, 1 keV and 10 keV. The bands of interest are N_2^+ 1N (0,1), (1,2) and (2,3) plotted with solid line, dashes and dot-dash respectively. Resonance scattered emission is drawn in black and direct excitation emission in grey. It is evident from these results that the photon scattering contribution becomes increasingly significant at energies below 1 keV. The height labelled B represents the steady state boundary.

In order to compare the modelled emissions with those measured, we now consider how the modelled total brightness in each of the three bands of interest varies with shadow height. In Fig. 7.4 the total brightness is plotted for three primary electron input energies. It can be seen that the enhancement from resonance scattering increases with decreasing energy. For example, for electron energies of 100 eV (blue curves) at steady state, the brightness of the (2,3) band increases by two orders of magnitude as the shadow height decreases from 400 km to 250 km. The effect is similar for the (1,2) band, but to a lesser extent; for the (0,1) band the brightness increases by an order of magnitude. For higher energies (green and red curves) the increase in brightness with decreasing shadow height is less pronounced, being almost negligible for energies of 10 keV, due to the short ion lifetime at these heights.

The total brightness ratios (2,3)/(0,1) and (1,2)/(0,1) are plotted in Fig. 7.5 as a function of shadow height and using a range of input energies, and for T_{vib} of 1000 K. The ratio resulting from direct excitation is independent of energy, and is 0.01 for (2,3)/(0,1) and 0.18 for (1,2)/(0,1). With the inclusion of resonance scattering the ratios become

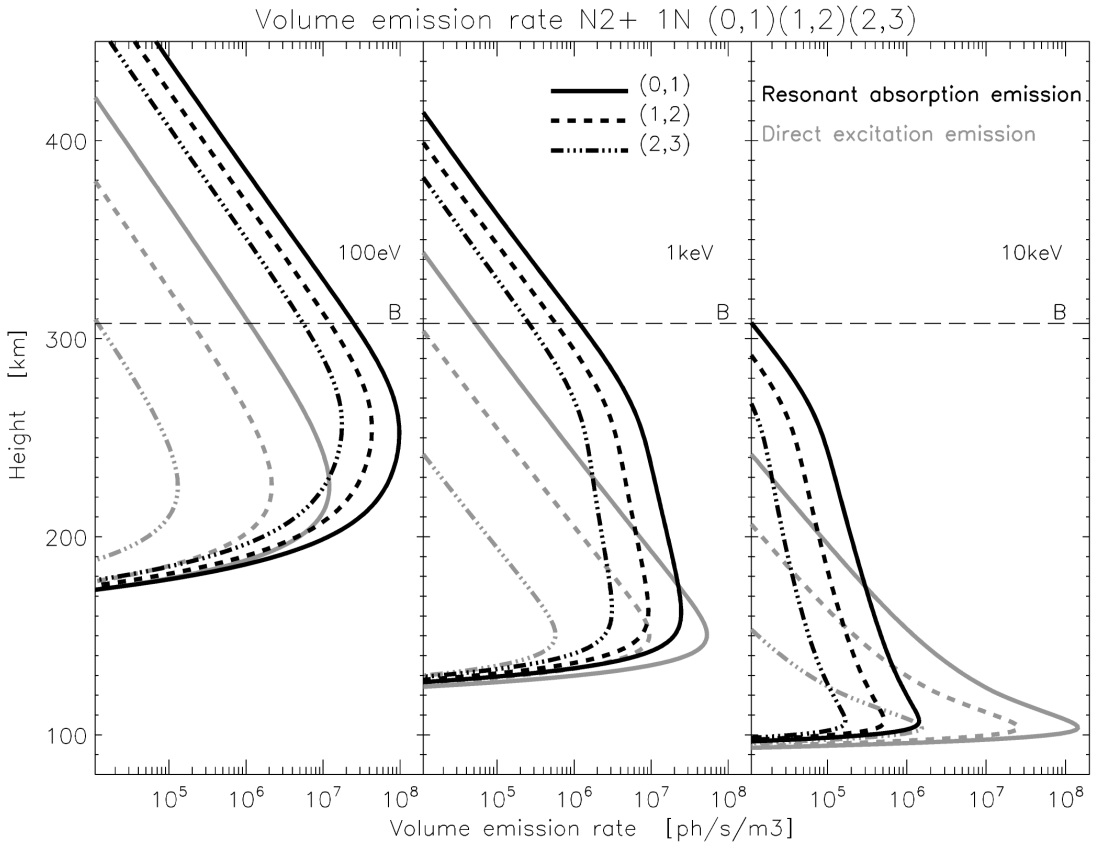

Figure 7.3: *Synthetic volume emission rates of N_2^+ (0,1) (solid),(1,2) (dashed) and (2,3) (dot-dash) corresponding to input energies of 100 eV, 1 keV and 10 keV for 30 s. Emission rates from direct excitation are in grey and resonance scattered emissions are in black. The steady state boundary for this condition is drawn at height B.*

a function of energy, increasing with decreasing electron energy. For energies below 100 eV the brightness ratio of (2,3)/(0,1) ratio is greater than 0.17, and the (1,2)/(0,1) is greater than 0.42.

The contribution of resonance scattering to observed height integrated N_2^+ 1N emissions depends on shadow height, electron energy and the band in question. Figure 7.6 shows the enhancement of total brightness compared to that resulting from only direct excitation for the three bands of interest. Two effects are noticeable. Firstly, the res-

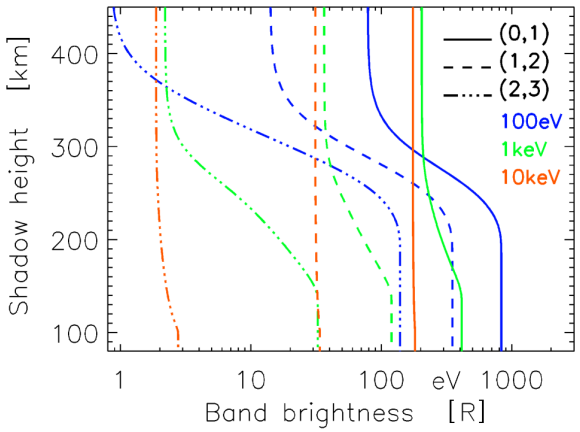

Figure 7.4: *Band brightness as a function of shadow height for primary electron energies of 100 eV (blue), 1 keV (green) and 10 keV (red) for the N_2^+ bands (0,1) (solid line),(1,2) (dashed) and (2,3) (dot-dash).*

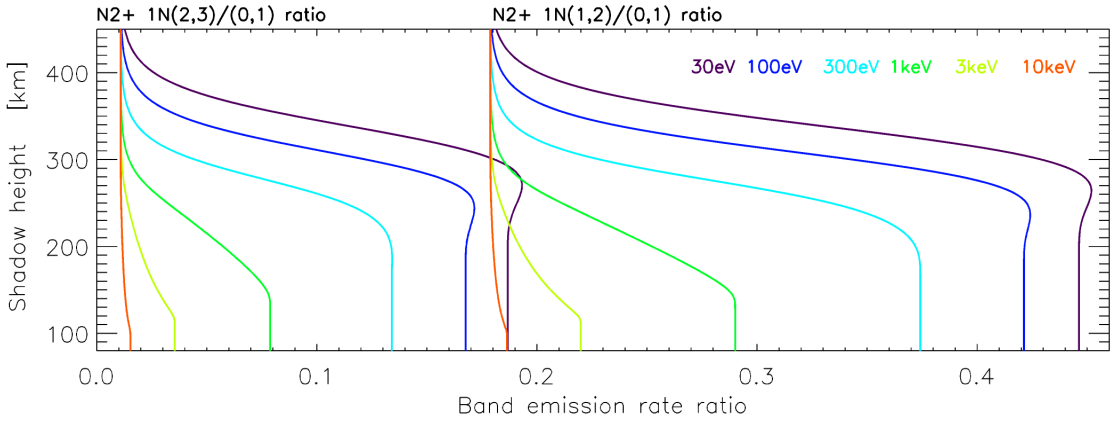

Figure 7.5: *Band brightness ratios as a function of shadow height for different primary electron energies for N_2^+ 1N (2,3)/(0,1) (left) and (1,2)/(0,1) (right).*

onance absorption enhancement increases with the vibrational v' level. Secondly, the maximum enhancement of resonant scatter is reached when the shadow height is below the height of peak ion density. For low energies the enhancement starts at higher altitudes and also reaches a maximum at higher altitudes.

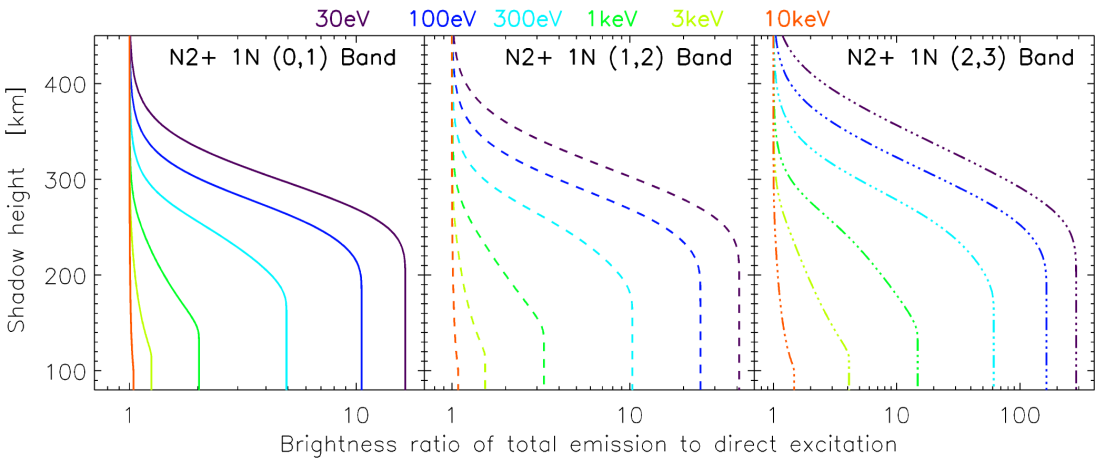

Figure 7.6: *The brightness of N_2^+ 1N (0,1), (1,2) and (2,3) bands with respect to the brightness of the same bands from direct excitation for a range of input electron energies.*

7.3.2 g-values

Scattering has been characterised by the g-value [Chamberlain, 1961], which is defined as the number of photons scattered per second per unit atom if there were no deactivation. In the present work the g-value should characterise resonance scattering per molecular N_2^+ ion. A problem lies in that different vibrational levels of N_2^+ X have different resonant absorption efficiencies. These efficiencies are presented in Table 7.1 for the 1N band system. Furthermore, the vibrational distribution in the N_2^+ X levels depends on the initial distribution from direct excitation and the re-distribution by resonance absorption, which is a function of ion lifetime. Hence, it is possible to quantify a g-value for a particular vibrational level for a specific height, but it is impossible to assign a single g-value for the total N_2^+ population.

7.3.3 Rotational temperatures

As detailed in Jokiaho et al. [2008], rotational temperatures of the N_2^+ 1N bands are related to the temperature of the parent neutral population. As this temperature is

N_2^+1N	$v'=0$	$v'=1$	$v'=2$	$v'=3$
$v''*=0$	8.240e-2	1.995e-2	2.538e-3	5.289e-5
$v''*=1$	6.079e-2	2.219e-2	3.246e-2	5.707e-3
$v''*=2$	2.564e-2	6.650e-2	4.716e-3	3.183e-2
$v''*=3$	7.389e-3	4.793e-2	5.300e-2	1.827e-4
$v''*=4$	2.032e-3	1.874e-2	5.855e-2	3.790e-2
$v''*=5$	–	6.711e-3	3.188e-2	5.589e-2

Table 7.1: *N_2^+ X resonance absorption efficiencies to N_2^+ B in units of (ph/s) per ion in the X state.*

strongly height dependent, it can be used to assess the energy of the electrons creating auroral emissions. In sunlit aurora the rotational temperatures estimated from the height-integrated spectra will be enhanced for two reasons. Firstly, resonance scattering produces the strongest enhancement in the aurora at the highest altitudes, where the neutral temperature is greatest. Secondly, after multiple scattering, the rotational temperature will tend to the spectral temperature of the solar spectrum as it is in a collisionless environment. Complete modelling of the distribution of rotational intensities is outside the scope of this paper, but the lowest limit to an estimated rotational temperature can be obtained by assuming that the N_2^+ population retains the rotational distribution of the parent N_2 population (i.e. without taking account of redistribution in resonance scattering). In Fig. 7.7 this variation of rotational temperature with shadow height and input energy has been estimated using the theoretical model results. A synthetic spectrum is obtained from the model emission rate profiles for different input energies. These spectra are integrated in height and fitted over the same wavelength range as the observations to find the rotational temperature. The effect on the rotational temperature of different shadow heights is shown in colour.

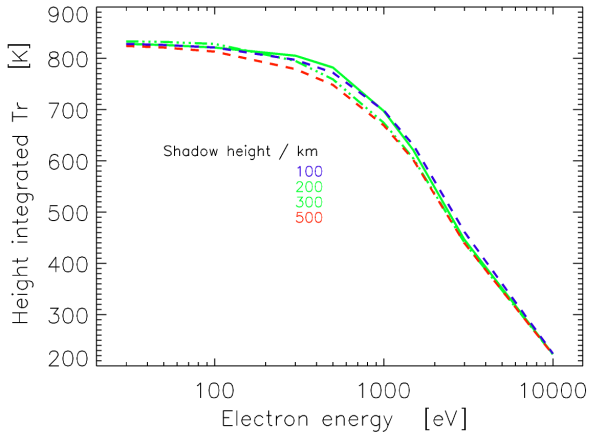

Figure 7.7: *Height integrated rotational temperature profiles as a function of primary electron energy and shadow height.*

7.4 Experimental results

An overview of the data used in this study is shown in two different representations in Fig. 7.8. In Fig. 7.8a the data are plotted against local time in day after 1 January 2007. In Fig. 7.8b the same data points are ordered with hours UT. In each part the data are presented in four panels: three ratios N_2^+ 1N (1,2)/(0,1), N_2^+ 1N (2,3)/(0,1), N_2 2P (0,3)/N_2^+ 1N (0,1) and rotational temperature. All the data in this section are ordered by shadow height using colour coding. It was assumed that there is no screening height for atmospheric absorption.

From the first set of figures in Fig. 7.8a it can be seen that the values for the 1N ratio (1,2)/(0,1) in the top panel are in the range $0.1-0.4$ and those for the 1N ratio (2,3)/(0,1) are in the range $0.01-0.3$. These values can be compared with the theoretical values of Fig. 7.5, and are in good agreement. The lower range in both cases is somewhat higher than the theoretical values, but this may be accounted for by the value of vibrational temperature being too high at 1000 K for auroral heights. The ratio of N_2 to N_2^+ emissions in the third panel is inversely proportional to the enhancement of the ion emission in resonance scattering. As we do not model the 2P bands, only relative variations are of

interest. The fourth panel shows clearly that the rotational temperatures are enhanced for low shadow heights. The 1N ratios also increase with decreasing shadow height.

In Fig. 7.8b the effect of local time is apparent immediately, with two distinct populations seen in all four panels. Most of the data with shadow height below 250 km occur between 04-10 UT when Svalbard is under the morning oval and in the cusp. The 1N ratios in the two top panels demonstrate an increasing ratio with decreasing shadow height, which follows the increase of UT. In the third panel it is noticeable that the ratios of N_2 to N_2^+ emissions are much lower in the morning hours than the evening, indicating the effect of increased emission from scattering. The rotational temperatures are clearly higher during the morning hours, as seen in the bottom panel, and again there is some indication of ordering with shadow height. The population from the evening aurora between 18-23 UT is when the statistical oval is overhead on Svalbard. The 1N ratios are lower, and the rotational temperatures are lower, corresponding to both high shadow heights and more energetic precipitation.

In order to study these separate populations in more detail, the data have been ordered with band brightness in Fig. 7.9, using the same format for the ratios and rotational temperature, and using colour to display the shadow height. The data on the left are from 03-11 UT and those on the right are from 19-01 UT. During the evening and night hours the ratio of 1N (1,2)/(0,1) in the top panel of Fig. 7.9b decreases as the brightness increases, which is the possible effect of increasing energy with increasing brightness. The second panel of Fig. 7.9b is more noisy, so no trend is seen. In both these panels there are some higher values of ratios associated with lower shadow heights. The third panel of Fig. 7.9b is as expected for the ratio of the neutral N_2 to N_2^+. The constant proportionality is seen, with little effect from sunlight. The spread of data points reduces with increased brightness, with the data converging on the constant value of about 0.04. In the bottom panel of Fig. 7.9b there is a trend to lower rotational temperatures with increasing brightness, again indicating a relationship between energy and brightness.

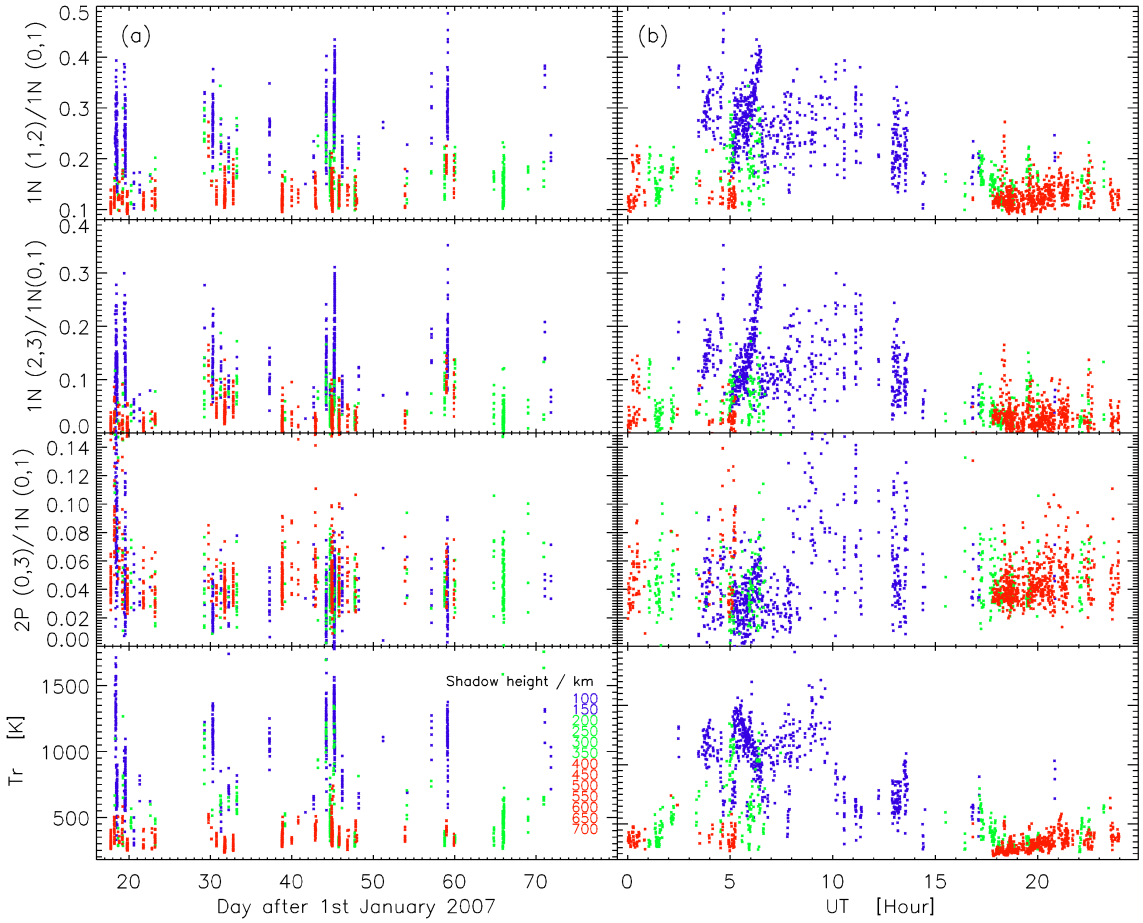

Figure 7.8: *(a) Ratios of N_2^+ 1N (1,2)/(0,1), (2,3)/(0,1), N_2 2P (0,3)/1N (0,1) and rotational temperature as a function of number of days since 1 Jan 2007. Solar shadow height (excluding screening height) is shown in colour. (b) Ratios of N_2^+ 1N (1,2)/(0,1), (2,3)/(0,1), N_2 2P (0,3)/1N (0,1) and rotational temperature as a function of universal time. Solar shadow height (excluding screening height) is shown in colour.*

The morning and cusp hours shown in Fig. 7.9a are very different from the evening hours. The enhanced ratios are clearly organised by shadow height in the top two panels. There is a distinct group of data points associated with a shadow height of > 400 km with low ratios and high brightness, which follow the nightside distribution. For these data the aurora is dominating the resulting ratio values. In the third row of panels the

scatter in the ratio of N_2 to N_2^+ is greater for the morning hours than for the evening hours. In both cases the high ratios are a result of the larger experimental uncertainty for lower brightnesses. However, it is significant that there is a range of ratios below the constant value of approximately 0.04 seen on the night side. Ratios as low as 0.01 are seen in the morning hours. These values indicate an enhancement of N_2^+ due to resonant scatter over the constant neutral N_2 emissions, which can be estimated from the theoretical values in Fig. 7.6 for N_2^+ 1N (0,1) as a four-fold increase. Our steady state assumption allows us to estimate the characteristic electron energy required to produce the enhancement assuming the shadow height is known; e.g. for shadow heights of 200 km and 300 km such ratios were found to correspond to electron energies of 300 eV and 30 eV respectively. The bottom panel of Fig. 7.9a shows two groups of data points for rotational temperature versus brightness during the morning and cusp hours: one low energy, high temperature (low shadow heights) that are associated with the scattering processes and another higher energy, lower temperature (high shadow heights). The evening-night time spectra in the bottom panel of Fig. 7.9b shows only the unaffected high energy and low temperature characteristics of the aurora from direct excitation.

Finally the 1N ratios (1,2)/(0,1) have been plotted versus rotational temperature in Fig. 7.10 for the morning hours 03-11 UT. The high temperatures up to 1500 K are found for low shadow heights and high ratios. The minimum temperatures estimated in Fig. 7.7 from our simple model are below 1000 K for all energies and shadow heights, so there is a strong effect from scattering which requires more careful analysis. Such high temperatures suggest considerable redistribution between the rotational levels that may be influenced by solar radiative temperature.

7.5 Discussion and Conclusions

The aim of the present work is to assess and quantify the effects of resonance scattering on N_2^+ 1N emissions at high latitudes. The theoretical treatment of Sect. 3 solves the

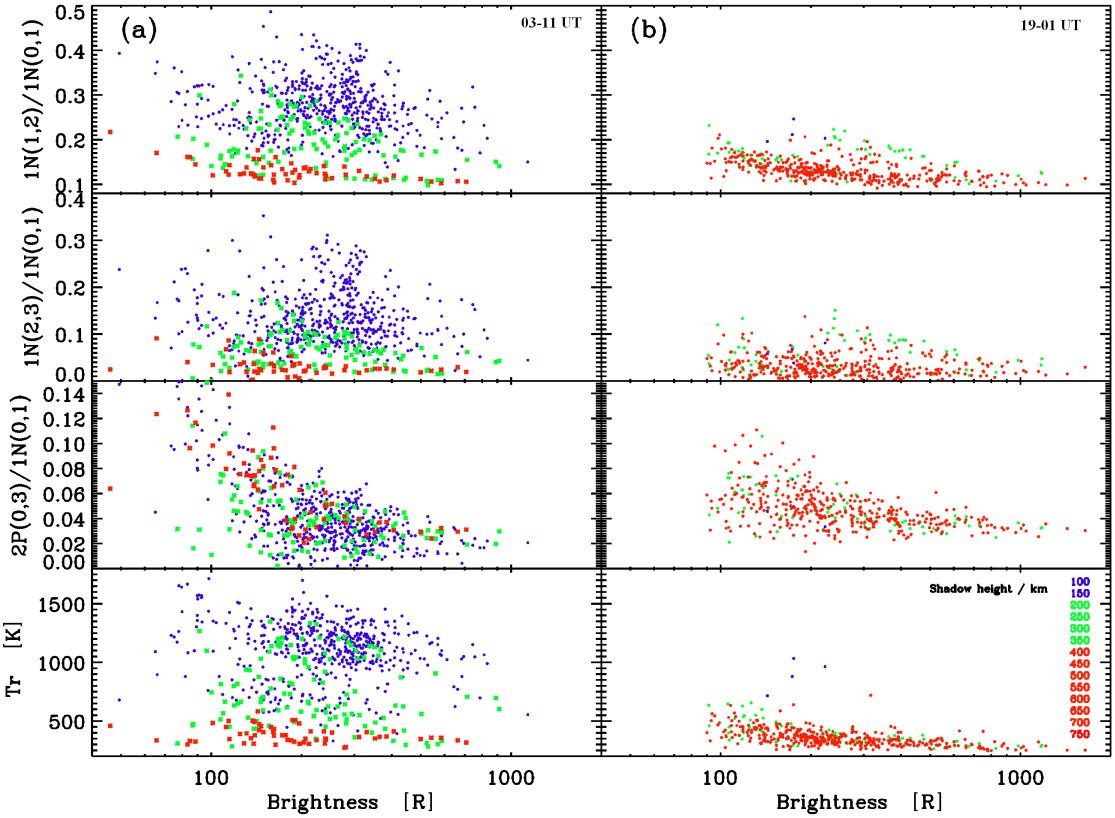

Figure 7.9: *Ratios of N_2^+ 1N (1,2)/(0,1), (2,3)/(0,1), N_2 2P (0,3)/1N (0,1) and rotational temperature as a function of N_2^+ 1N (0,1) band brightness for (a) morning-day time (03-11 UT) and (b) evening-night time spectra (19-01 UT). Solar shadow height (excluding screening height) is shown in colour.*

balance equations for steady state to give the populations of all the vibrational levels of the N_2^+ X, A and B states, and hence, using an ion chemistry model, the emissions from direct excitation and from scattering, with changing shadow height. The main result of this work shows that for shadow heights above about 400 km the 1N bands and their ratios are almost unaffected, but for shadow heights below 150 km (i.e. fully illuminated) there are significant enhancements which increase with decreasing energy. At very low energies of 100 eV the increase in brightness is found to be a factor of 10

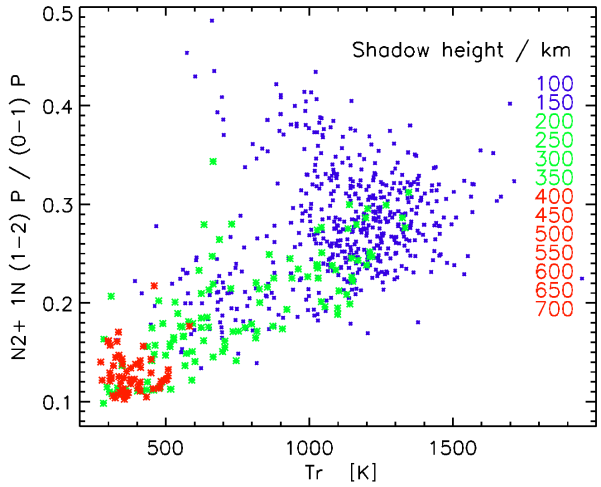

Figure 7.10: *The ratio of N_2^+ 1N (1,2)/(0,1) as a function of rotational temperature and shadow height (excluding screening height) for 03-11 UT.*

(Fig. 7.4).

The variation in the ratios of the 1N bands have been modelled for (1,2)/(0,1) and (2,3)/(0,1) for several input energies, and as a function of shadow height, in order to compare with the observations from more than two winter months. The observed ratios have a lower limit than the theoretical values, which can be explained by the choice of T_{vib} in the modelling. We have chosen a vibrational temperature of 1000 K as a conservative estimate. It can be determined from Fig. 6.6 that the ratios will decrease with a smaller value of T_{vib} as seen in the relative populations shown in Fig. 6.5. The non-sunlit N_2^+ 1N (1,2)/(0,1) ratio was measured by Vallance Jones [1974] as 0.1290, and the (2,3)/(0,1) ratio as 0.0017. These values are both smaller than our theoretical ratios, but in the range that we observe.

The main result of the present work is that the ratios of the 1N bands are a function of energy under sunlit conditions. The observations in this statistical study do not give an independent estimate of electron precipitation. The results from previous observations of the magnitude of the effect of resonance scattering make claims of specific percentages. It is clear from the present work that such numbers as 56% quoted by other

observers are not valid without knowledge of the energy spectrum of the precipitation that has excited and ionised the nitrogen molecules. Over the two months of 24 hours of twilight and solar illumination that we have measured, the emissions are clearly from a large range of energies, i.e. from precipitation events that vary significantly.

In order to determine the effect of resonance scattering more accurately it is necessary to know the energy of precipitation, which indicates that a case by case approach is more suitable. With the advantage of incoherent scatter radar to provide electron density profiles, the incoming energies can be inferred. Jokiaho et al. [2008] have used the EISCAT radar to compare energies derived from electron densities and modelling with those derived from optical measurements of N_2^+ using rotational temperatures. It was this study that gave impetus to the need to determine the effects of sunlight on these important emissions. There are clear events within the present observations that will be used for future case studies. One event can be readily distinguished in the overview plots of Fig. 7.8 between 05:00 UT and 06:30 UT. This was a period of continuous electron precipitation on 14 Feb 2007. During this time the ratios of N_2^+ (1,2)/(0,1) and (2,3)/(0,1) were steadily increasing whilst the rotational temperature was steadily decreasing as a function of time, indicating increasing electron energy.

We have established in the observations that the rotational temperature is strongly affected by the resonance scattering, not only through the peak in the emission profile shifting to higher altitude with higher corresponding neutral temperatures. Values of T_{rot} in excess of 1000 K suggest considerable redistribution between the rotational states. In order to calculate the full effect, a complete model is required which includes all rotational states, radiative and collisional processes (including inelastic collisions with N_2 and electrons). This is outside the scope of this paper, but is important for future work. It should be noted however, that if inelastic collisions not leading to the loss of N_2^+ ions are important, their effect will be to equalise the rotational temperatures of N_2^+ and the neutrals or electrons. These temperatures are typically below 1000 K for the conditions presented, so any observation of T_{rot} in excess of this must come

from heights where collision frequencies are negligible compared to characteristic frequencies of resonance scattering (g-factors). The fact that such values of T_{rot} are indeed observed may point to the importance of ion upflow processes.

Chapter 8

Summary

This section encapsulates the motives and rationale behind this thesis. During this PhD work, an independent spectrograph mosaic filter design was performed. This was followed by modelling of vibrational population distribution of diatomic molecules via *ab initio* time independent model and an *ab initio* model of rotational spectra of diatomic molecules with convolved instrument function. It was followed by quantifying the spectral coefficients for throughput of various optical imaging filters as a function of rotational temperature. These models have been complemented by data from incoherent scatter radar, in the form of electron density profiles and the HiTIES spectrograph in the form of rotational spectra from zenith optical measurements. This was followed by the assessment of various excitation and loss processes of excited and ionised N_2 populations as a function of height and the effect of resonant scattering of sunlight via N_2^+ in sunlit aurora both qualitatively and quantitatively.

The motivation behind this doctoral study lies in the fact that spectral modelling of aurora can directly yield the excitation processes involved in creating the emissions. Until now, the role of resonance scattering on auroral emissions is not easily found in literature. During sunlit or partially sunlit conditions the measured values of emission intensities (and rotational temperatures) will lead to uncertainties in the characteristic electron energy and energy flux. The average energy from rotational spectra can be underestimated due to the contribution from highly developed sunlit spectra. Similarly, the flux can be overestimated in a simple photometric measurement when the brightness is increased due to the scattered contribution. The present work was influenced by the availability of the Southampton ion chemistry code that could be used together with

the use of solar shadow height, primary electron energy and modelling of vibrational populations can directly quantify the various emissions processes from ions created by precipitating electrons onto atmospheric constituents.

The main finding in this work is the relationship between resonant scattering of solar photons via N_2^+ and direct emission from electron impact on N_2. A relationship was found that clearly indicates the observations are a function of primary electron energy and solar shadow height when the auroral arcs are partially sunlit during events of electron precipitation.

The work has high relevance for future activity and suggests two directions for further commitment. One is an event study of comparing 'cusp' observations with high shadow heights, and those with low shadow heights rather than a statistical long term study done here, especially if there are corresponding radar data. This would allow more comprehensive rotational analysis to be made in an attempt to explain the high temperatures seen here.

The other is a time dependent study of the effects of scattering. When the lifetime of the N_2^+ ion becomes comparable with the scattering timescale, and with timescales of temporal variations in the aurora, the steady state solution poorly describes the reality. Another interesting implication is that the sun-illuminated N_2^+ population at high altitudes serves as a 'marker' of the F-region plasma, in a way similar to the metastable O^+ population, opening the possibility for direct optical observations of plasma flows [Dahlgren et al., 2009].

During the post graduate work the writer learned to understand atmospheric reaction processes and recognise the importance of vibrational and rotational degrees of freedom in electronic transitions. This includes cascading and photon scattering that increases the brightness but consequently do not increase the total ion content in the ionosphere. This will no doubt form a foundation for theoretical models for synthetic emission features of future projects including low light optical instruments and filters.

Bibliography

Ashrafi, M., Lanchester, B. S., Lummerzheim, D., Ivchenko, N. and Jokiaho, O., Modelling of N_2 1P emission rates in aurora using different cross sections for excitation, *Ann. Geo.*, *27*, 2545-2553, 2009.

Ashrafi, M., ASK Auroral Structure and Kinetics in action, *Astronomy Geophysics*, *48*, *4*, 2007.

Bates, D. R., The emission of the negative system of nitrogen from the upper atmosphere and the significance of the twilight flash in the theory of the ionosphere, *Proc. R. Soc.*, *A196*, 562591, 1949.

Brandy, J. H., Rotational temperatures of the auroral 3914 Å nitrogen band vs. height at Churchill, Manitoba, *Can. J. Phys. 31*, 1793–1797, 1964.

Broadfoot, A. L., Resonance Scattering by N_2^+, Planet. Space Sci., Vol 15, 1801-1815, 1967.

Chakrabarti, S., Pallamraju, D., Baumgardner, J. and Vaillancourt, J., HiTIES: A High Throughput Imaging Echelle Spectrograph for ground-based visible airglow and auroral studies, *J. Geophys. Res. 106*, 30,337–30,348, 2001.

Chamberlain, J. W. , Physics of the aurora and airglow, *Academic Press*, 424, 1961.

Dahlgren, H., Ivchenko N., Lanchester, B., Ashrafi, M., Whiter, D., Marklund, G., Sullivan, J., First directoptical observations of plasma flows in the metastable O+ ion in discrete aurora, *J. Atmos. Sol. Terr. Phys.*, *71*, 228-238, Feb, 2009.

Dahlgren, H., Ivchenko N., Sullivan, J., Lanchester, B., Marklund, G., Whiter, D., Morphology and dynamics of aurora at fine scale: first results from the ASK instrument, *Ann Geo.*, *26*, 1041-1048, May 2008

Degen, V., Modeling of N_2^+ First Negative spectra excited by electron impact, *J. Quant. Spectroscopic Radiat. Transfer*, *18*, 113–119, 1977.

Degen, V. , Vibrational Enhancement and the Excitation of N_2^+ and the First Negative System in the High-Altitude Red Aurora and the Dayside Cusp, *J. Geophys. Res.*, *86*, *A13*, 11372-11378, December, 1981.

Degen, V., Modeling of the N_2^+ First Negative Bands in the Sunlit Aurora, *Planet. Space Sci.*, *35*, *8*, 1061-1066, 1987.

Fordham, J. L., Bellis, J. G., Bone, D. A., Norton, T. J., MIC photon counting detector, *Proc. SPIE*, *1449*, *Electron Image Tubes and Image Intensifiers II, edited by Csorba, I. P.*, 87-98, 1991.

Fox, J. L., Dalgarno, A., The vibrational Distribution of N_2^+ in the terrestrial ionosphere, *J. Geo. Res.*, *90*, *A8*, 7557-7567, 1985

Galand, M., Baumgardner, J., Pallamraju, D., Chakrabarti, S., Lvhaug, U. P., Lummerzheim, D., Lanchester, B. S., Rees,M. H., Spectral imaging of proton aurora and twilight at Troms, Norway, *J. Geophys. Res.*, *109*, *A7*, 2004.

Gattinger, R. L., Vallance Jones, A., Hecht, J. H., Strickland, D. J., Kelly, J., Comparison of ground-based optical observations of N_2 second positive to $N_2(+)$ first negative emission ratios with electron precipitation energies inferred from the Sondre Stromfjord radar, *J. Geophys. Res.*, *14*, *96*, 11,341-11,351, 1991.

Gilmore F. R., Laher, R. R., Espy, P. J., Franck-Condon Factors, R-centroids, Electronic Transition Moments and Einstein Coefficients for Many Nitrogen and Oxygen Band Systems, *J Phys Chem Ref Data*, *21*, *5*, 1992.

Ginsburg, N., Dieka, G. H., *Physic. Rev. 59*, 632, 1941.

Gustavsson, B., Three Dimensional Imaging of Aurora and Airglow, Doctoral thesis at the Swedish Institute of space Physics, Kiruna, 2000

Harang, L. The Aurorae, Chapman and Hall Ltd., 1951, p 83.

Hedin, A. E., Extension of the MSIS thermosphere model into the middle and lower atmosphere, *J. Geophys Res. 96*, 1159–1172, 1991.

Henriksen K., Deehr C. S., Romick G. J., Sivjee G. G., Fedorova N. L., Totunova G. F., Low energy enhancement of the OI 6300A line and enhancement due to resonance excitation of the N2+ first negative bands, *Ann Geophys*, *2*, *2*, 191-196, 1984

Henriksen, K., Veseth, L., Deehr, C. S, Smith, R. W., Neutral temperatures and emission height changes in an E-region aurora, *Planet. Space Sci. 35*, 1317–1321, 1987.

Herzberg, G., *Spectra of diatomic molecules*, 2nd edition, D. van Nostrand, 1950.

Hilliard, R. L., Shepherd, G. G., Upper atmosphere temperatures from Doppler line widths, 4. A detailed study using the OI 5577 Å auroral and nightglow emissions, *Planet. Space Sci. 14*, 383–406, 1966.

Holma, H. A., Kaila, K. U., Jussila, J. R. T., Temperatures, emission heights and energies in discrete auroral forms, *Phys. Chem. Earth (B)*, *25*, 463–466, 2000.

Holma, H. A., Kaila, K. U., Jussila, J. R. T., Electron energy estimations in an auroral arc, *Proc. 28th Ann. Europ. Meeting of Atmospheric Studies by Optical Methods*, S.G.O. Publications *92*, 105–108, 2003.

Hunten D. M., Koenig, H. J., Vallance Jones, A., Rotational Structure of the 3914 A N_2 Band in Sunlit Aurorae, *Nature*, 183, February 14,453-454, 1959.

Hunten, D. M., Rawson, E. G., Walker, J. K., Rapid measurement of N_2^+ rotational temperatures in aurora, *Can. J. Phys. 41*, 258–270, 1963.

Hunten, D. M., Sunlit Aurora and the N_2^+ ion: a Personal Perspective, *Planet. Space Sci.*, *51*, 887-890, 2003.

Ivchenko, N., Galand, M., Lanchester, B. S., Rees, M. H., Lummerzheim, D., Furniss, I. and Fordham, J., Observation of $O^+(^4P - ^4D^0)$ lines in proton aurora over Svalbard, *Geophys. Res. Lett.*, *31*, 2004.

Jevons, W., Report on Band-Spectra of Diatomic Molecules, The Physical Society, The University Press Cambridge, 1932

Jokiaho O., Lanchester, B. S., Ivchenko, N., Daniell, G. J., Miller, L. C. H., Lummerzheim, D., Rotational temperature of N_2^+ (0−2) ions from spectrographic measurements used to infer the energy of precipitation in different auroral forms and compared with radar measurements, *Ann. Geo.*, *26*, *7*, 853-866, 2008.

Jokiaho O., Lanchester, B. S. and Ivchenko, N., Resonance scattering by auroral N_2^+: steady state theory and observations from Svalbard., *Ann. Geo.*, *27*, *9*, 3465-3478, 2009.

Kaila, K. U., Determination of the energy of auroral electrons by the measurements of the emission ratio and altitude of aurorae, *Planet. Space Sci.*,*37*, 341–349, 1989.

Koehler, R. A., Shepherd, M. M. Shepherd, G. G., Paulson, K. V., Rotational temperature variation in pulsating auroras, *Can. J. Phys. 59*, 1143–1149, 1981.

Lanchester, B. S., Rees, M. H.,Field-aligned current reversals and fine structure in a dayside auroral arc, *Planet. Space. Sci.*, *35*, *6* ,759-768, 1987.

Lanchester, B. S., K. U. Kaila, and I. W. McCrea, Relationship between large horizontal electric fields and auroral arc elements, *J. Geophys. Res. 101*, 5075–5084, 1996.

Lanchester, B. S., Rees, M. H., Lummerzheim, D., Otto, A., Frey, H. U., and Kaila, K. U.: Large fluxes of auroral electrons in filaments of 100 m width, *J. Geophys. Res. 102*, 9741–9748, 1997.

Lanchester, B. S., M. H. Rees, D. Lummerzheim, A. Otto, K. J. F. Sedgemore-Schulthess, H. Zhu, I. W. McCrea, Ohmic heating as evidence for strong field-aligned currents in filamentary aurora, *J. Geophys. Res. 106*, 1785–1794, 2001.

Lanchester, B. S., Rees, M. H. Robertson, S.C., Galand, M., Lummerzheim, D., Baumgardner, J., Mendillo, M., Furniss, I. and Aylward, A. D., Proton and electron precipitation over Svalbard - first results from a new Imaging Spectrograph (HiTIES), *Proc. 28th Ann. Europ. Meeting of Atmospheric Studies by Optical Methods*, S.G.O. Publications *92*, 33–36, 2003.

Lanchester, B. S., Ashrafi, M., Ivchenko, N., Simultaneous imaging of aurora on small scale in OI (777.4 nm) and N2 1P to estimate energy and flux of precipitation, *Ann. Geo.*, *27* , 2881-2891, 2009

Lofthus, A. and Krupenie, P. H., The spectrum of molecular nitrogen, *J. Phys. Chem. Ref. data*, *6*, No. 1, 113, 1977.

Lummerzheim, D., and Lilensten, J., Electron transport and energy degradation in the ionosphere: evaluation of the numerical solution, comparison with laboratory experiments and auroral observations, *Ann. Geophysicae.*, *12*, 1039-1051, 1994.

McWhirter, I., Furniss, I., Aylward, A. D., Lanchester, B.S., Rees, M. H., Robertson, S. C., Baumgardner, J. and Mendillo, M., A new spectrograph platform for auroral studies in Svalbard, *Proc. 28th Ann. Europ. Meeting of Atmospheric Studies by Optical Methods*, S.G.O. Publications *92*, 73-76, 2003.

Miller, J. R. and Shepherd, G. G., Auroral measurements using rocket-borne photometers, *Ann. Geophys. 24*, 305-312, 1968.

Morton, D. C., Atomic Data for Resonance Absorption Lines, *Astrophys J suppl S*, *77*, 119-202, 1991.

Naude, S. M., The Rotational Analysis of the First Positive Nitrogen (N2) Bands, *Phys. Rev. 38, 372 - 373*, June 1931.

Naude, S. M., Quantum Analysis of the rotational structure of the first positive bands of nitrogen (N_2), *Proceedings of the Royal Society of London. Series A, Vol. 136, No. 829, pp. 114-144*, May 1932.

Nevin, T. E., Rotational analysis of the first negative band spectrum of oxygen, *Philosophical Transactions of the Royal Society of London. Series A, Mathematical and Physical Sciences, Volume 237, Issue 783, pp. 471-507*, Nov 1938.

Nevin, T. E., Rotational analysis of the first negative band spectrum of oxygen II,*Proceedings of the Royal Society of London. Series A, Mathematical and Physical Sciences, Vol. 174, No. 958*, 371-378, 1938

Omholt, A., The Optical Aurora, Springer-Verlag, Heidelberg, 1971

Palmer, J. R., Plasma density variations in the aurora, PhD thesis, University of Southampton, 1995.

Rees, M. H. and D. Luckey, Auroral electron energy derived from ratio of spectroscopic emissions 1. Model computations, *J. Geophys. Res. 79*, 5181–5186, 1974.

Rees, M. H., Physics and chemistry of the upper atmosphere, *Cambridge University Press*, 1989.

Remick, K. J., Smith, R. W., Lummerzeim, D., The significance of resonant scatter in the measurement of N_2^+ first negative $0-1$ emissions during auroral activity, *J. Atmos. Sol. Terr. Phys., 63*, 295-308, 2001.

Romick, G. J., Degen, V., Stringer, W. J., Henricksen, K., The altitude profile of N_2^+ first negative rotational temperature in auroral arc, *J. Geophys. Res. 83*, 91–96, 1978.

Romick, G. J., Yee, J-H., Morgan, M. F., Morrison, D., Paxton, L. J., Meng, C-I., Polar Cap Optical Observations of Topside (>900km) Molecular Nitrogen Ions, *Geophys. Res. Lett., Vol. 26, 7*, 1003-1006, April 1, 1999.

Shepherd, G. G. and Eather, R. A., On the determination of auroral electron energies and fluxes from optical spectral measurements, *J. Geophys. Res. 81*, 1407–1410, 1976.

Shepherd, G. G. and Hunten, D. M., On the measurements of rotational temperature from unresolved auroral nitrogen bands, *J. Atmospheric Terr. Phys. 6*, 328–335, 1955.

Störmer, C., The Polar Aurora, Clarendon Press, 1955.

Squires, G. L., Practical physics, Fourth Edition, *Cambridge University Press*, 176, 2001.

Vallance Jones, A., Gattinger, R. L., Shih, P., Meriwether, J. W., Wickwar, V. B., Kelly, J., Optical and radar characterization of a short-lived auroral event at high latitude, *J. Geophys. Res. 92*, 4575–4589, 1987.

Vallance Jones, A., Hunten, D. M., Rotational and Vibrational Intensity Distribution of the First Negative N_2^+ Bands in Sunlit Auroral Rays, *Can. J. Phys., 38*, 458-475, 1960.

Vallance Jones A., Aurora, D Reidel Publishing Company

Vegard, L., Results of investigations of the auroral spectrum during the years 1921–1926, *Geophys. Publ., 9(11)*, 1–71, 1932.

Whitten R. C., Poppoff, I. G., Fundamentals of Aeronomy, John Wiley Sons Inc, 1971.

Zhu, H., A. Otto, M. H. Rees, B. S. Lanchester, and D. Lummerzheim, Ionosphere-magnetosphere simulation of small scale structure and dynamics, *J. Geophys. Res. 106*, 1795–1806, 2001.

Zwick, H. H. and Shepherd, G. G., Upper atmospheric temperatures from Doppler line widths -v. Auroral electron energy spectra deduced from the 5577 and 6300 Å atomic oxygen emissions, *Planet. Space Sci. 21*, 605–621, 1973.